TITAN
CARBON SEQUESTRATION

Underground Injection Control – Class VI Permit Application for

Cronos No. 1 and Rhea No. 1

Jefferson County, Texas

SECTION 1 – SITE CHARACTERIZATION

February 2024

LONQUIST
SEQUESTRATION LLC

SECTION 1 – SITE CHARACTERIZATION

TABLE OF CONTENTS

Figures

Tables

1.1. Overview

This site characterization for Titan Carbon Sequestration, LLC's (Titan) Titan Carbon Sequestration Project (Titan Project) was prepared to meet the requirements of Title 16, Texas Administrative Code (16 TAC) **§5.203(c)(2)** [Title 40, U.S. Code of Federal Regulations (40 CFR) **§146.82(a)(3)**]. This section describes the regional and site geology for the proposed location. The site characterization incorporates analysis from multiple data types from public, proprietary, and licensed data sets, including well logs, 3D seismic, academic and professional publications, and existing core-sample analyses.

1.2. Regional Geology

The proposed Titan Project is located in southeastern Texas within the Gulf of Mexico basin. The coastal portion of the basin covers approximately 148 million acres and includes parts of Texas, Louisiana, Mississippi, Alabama, Arkansas, Missouri, Kentucky, Tennessee, Florida, and Georgia (Roberts-Ashby, et al., 2012). Figure 1-1 depicts the location of the Titan Project relative to the present coastal extent of the Gulf of Mexico. A generalized stratigraphic column of the Gulf of Mexico basin is provided in Figure 1-2. The geologic section is comprised of up to 20 kilometers (km) of strata deposited in succession from the Jurassic to the Holocene (Roberts-Ashby, et al., 2012).

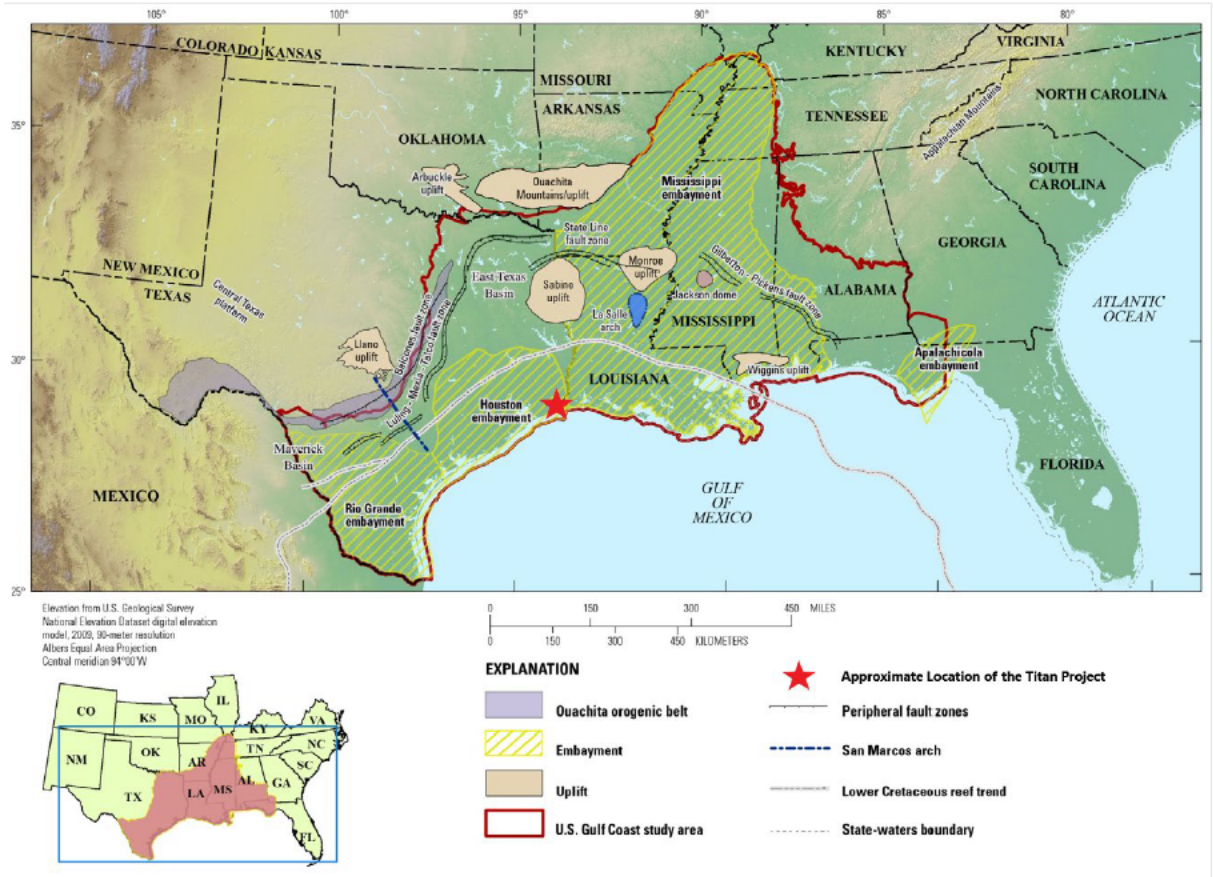

Figure 1-1 – Regional Gulf of Mexico Locator Map (modified from Roberts-Ashby et al., 2012)

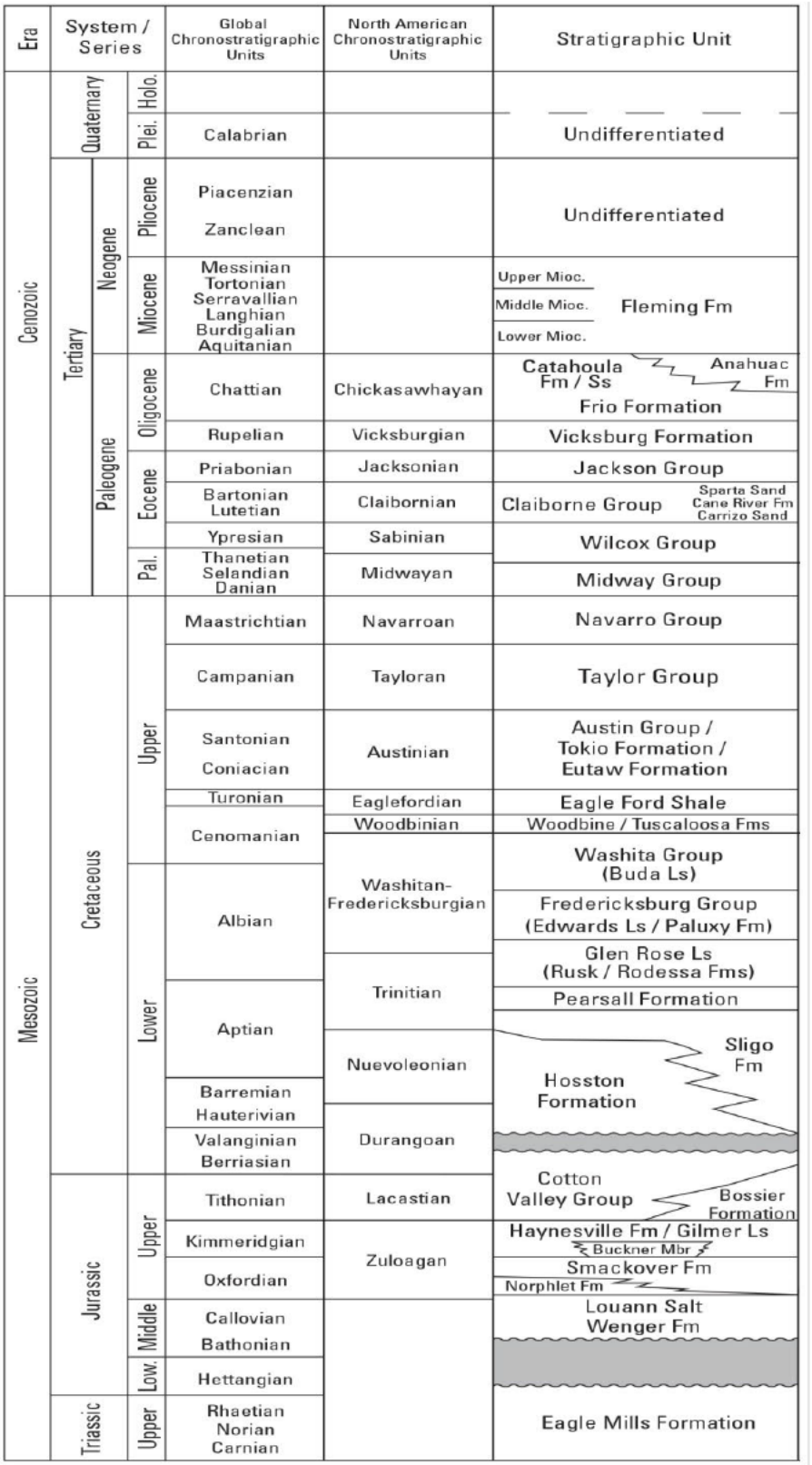

Figure 1-2 – Stratigraphic Column of the Gulf of Mexico (modified from Roberts-Ashby et al., 2012)

The Gulf of Mexico basin was formed by crustal extension and rifting events responsible for the separation of the North American plate and the Yucatan block during the Mesozoic breakup of Pangea. Rifting that commenced during the Middle Jurassic lasted approximately 25 million years and resulted in the variable thickness of transcontinental crusts underneath the basin (Galloway W. E., 2008).

Initial sedimentation occurred between the Late Triassic to Early Jurassic, with deposits filling accommodation space within graben structures created by seafloor spreading; these deposits consisted of terrestrial red beds and volcanics of the Eagle Mills formation (Galloway W. E., 2008). During the Middle to Late Jurassic, the basin consisted of a shallow, hypersaline environment with a narrow connection to the Atlantic Ocean (Treviño & Rhatigan, 2017). This resulted in large-scale deposition of a continuous evaporite sequence up to 4 km thick, known as the Louann Salt. The Louann Salt provided a foundation across the basin for subsequent deposition and played a critical role in later structural development of the basin (Galloway W. E., 2008).

Salt deposition halted by the end of the Jurassic, and subsequent fill into the basin consisted of successive sedimentation of clastics, carbonates, and evaporites. These strata were deposited in a highly cyclic environment, subject to frequent sea-level change and fluctuations in sediment supply that influenced deposition (Galloway W. E., 2008; Roberts-Ashby, et al., 2012). Deposition was also affected by five North American tectonic phases: (1) Laramide uplift, (2) mid-Cenozoic thermal phase, (3) basin and range tectonism, (4) southern Appalachian and Cumberland Plateau uplift and erosion, and (5) Rocky Mountain plateau tectonic uplift. Notably, the southern Appalachian and Cumberland Plateau uplift shifted the depocenter from the northwest portion of the basin margin to present-day Louisiana during the Miocene deposition (Galloway W. E., 2008).

The combination of subsidence and rapid sediment loading of up to 20 km of section over a foundation of salt up to 4 km thick resulted in significant salt mobilization and associated gravity tectonic structures—including growth faults, allochthonous salt bodies, salt welds, salt-based detachment faults, salt diapirs, and basin-floor compressional fold belts (Galloway W. E., 2008).

An interpreted regional seismic line through the Gulf of Mexico is provided in Figure 1-3 to illustrate the present-day structure of the basin. The figure includes a locator map and line of section for reference to the Titan Project, noted with a red star.

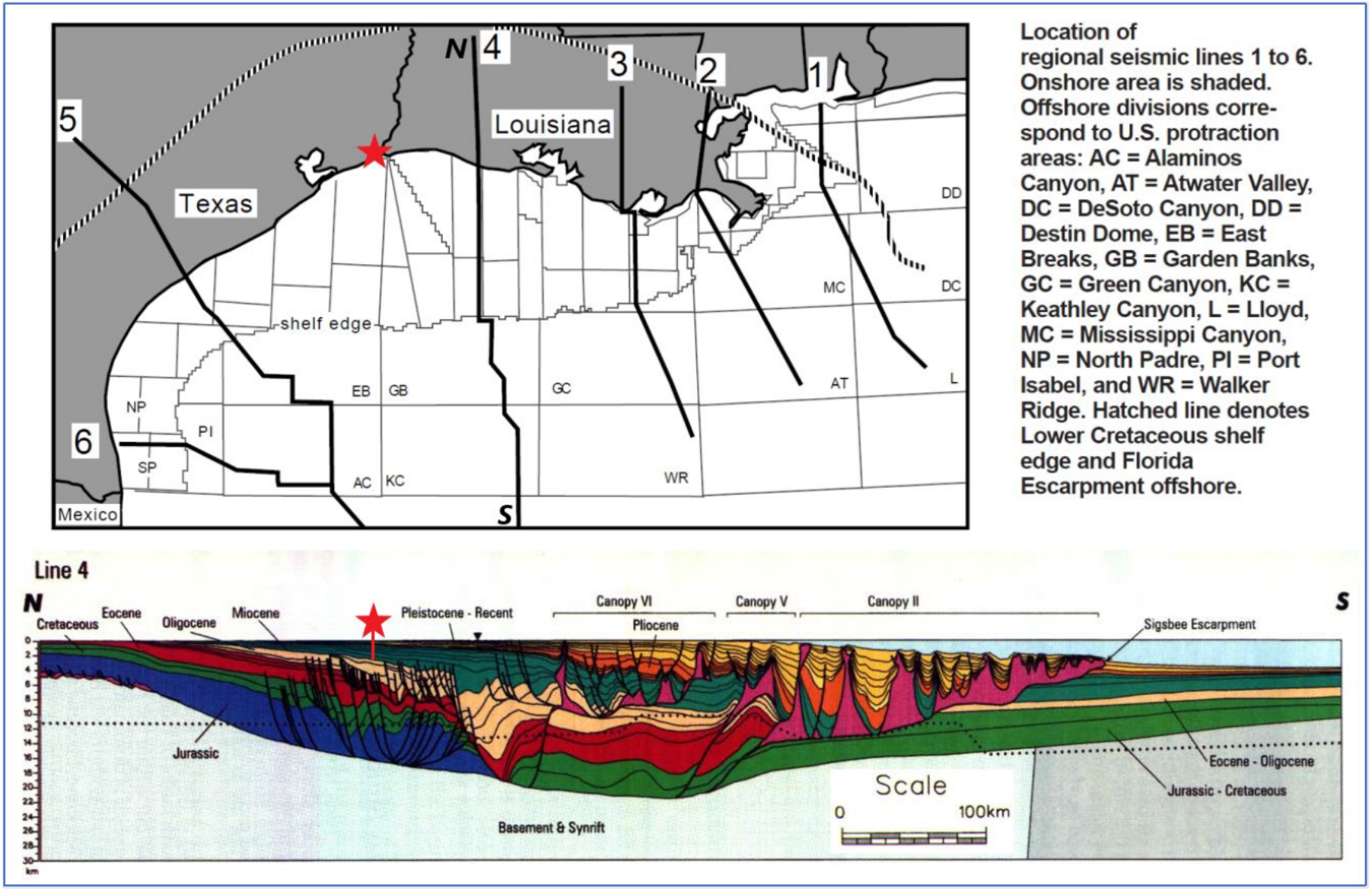

Figure 1-3 – Regional seismic line and locator map. The red star represents the approximate location of the Titan Project (modified from Peel et al., 1995).

1.2.1 Major Stratigraphic Units

The formations targeted in this study consist of Miocene deposits, specifically Lower Miocene to Middle Miocene in age. The Miocene geologic section along the Gulf Coast generally consists of four regressive, fluvio-deltaic depositional episodes, occasionally disrupted by marine transgression and regional deposition of shale. Regressive cycles are characterized by deposition of deltaic sands, silts, and clays; these intervals represent reservoir potential within the Miocene section. Periods of transgression and coastal onlaps are characterized by deposition of tight marine shales associated with biochronozone markers that "serve as fine-grained regional sealing units that subdivide the Miocene section into four SAUs [storage assessment units]": the Lower I, Lower II, Middle, and Upper series (Roberts-Ashby, et al., 2012).

Figure 1-4 contains a stratigraphic column of Tertiary depositional episodes in the Gulf of Mexico basin and clarifies the age of key biochronozone markers relative to sea-level fluctuation and the proposed stratigraphic intervals of the Titan Project. The stratigraphic intervals of interest are color coded by their role in the injection process, with confining zones shaded gray and the gross injection zone shaded yellow. The proposed injection zone for the Titan Project is located within the Lower Miocene regressive sequence and is confined by the overlying *Amphistegina B* (Amph B) and underlying *Siphonina davisi* (Siph Dav) transgressive cycles (Treviño & Rhatigan, 2017).

Sandstones within the four Miocene series are lithologically similar within the Gulf Coast region and are generally described as fluvial-dominated deltaic deposits that dip and thicken basin-ward. Deposition of Miocene sediments around the Titan Project occurred within the Calcasieu delta (Galloway, 2000; Roberts-Ashby et al., 2012).

A comprehensive stratigraphic review of Miocene strata and associated deposition within the Gulf of Mexico basin is available for reference in published material by Galloway (2008) and Snedden and Galloway (2019).

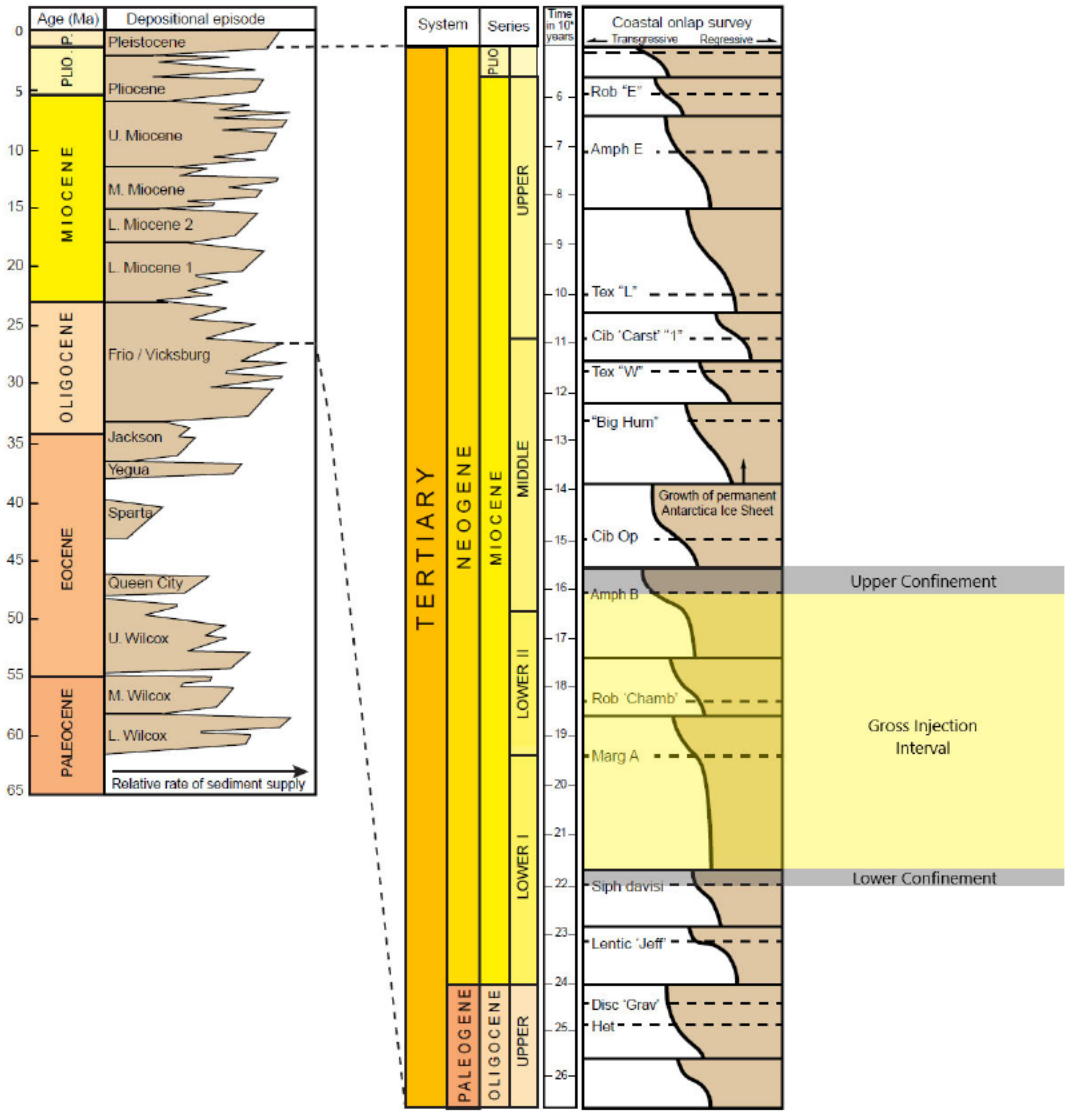

Figure 1-4 – Stratigraphic column of Tertiary depositional episodes in the Gulf of Mexico basin with Miocene sea-level fluctuations relative to associated biochronozones and proposed injection and confining zones (modified from Trevino and Rhatigan, 2017).

Lower Confining Zone: Lower Miocene Siph Dav

The proposed lower confining zone consists of the tight, transgressive Siph Dav shale located within the Lower Miocene. The Siph Dav shale consists of fine-grained silt and clay particles deposited during the maximum flooding surface associated with the first appearance of the Siph Dav biomarker. Maximum flooding surfaces are, by nature, deposited in a relatively high-water column, capable of dispersing fine-grained material and entrained clay well onto the continental shelf (Meckel and Trevino, 2014; Roberts-Ashby et al., 2012). Publicly available core data and published thin section analysis of Siph Dav core demonstrate "abundant clay and low porosity, therefore, high sealing capacity" (Meckel & Trevino, 2014). The base of the Siph Dav confining zone overlies the Lower Miocene "X Sand."

Injection Zone: Lower Miocene Sandstones

The proposed injection zone for the Titan Project consists of porous, regressive deposits located within the Lower Miocene. Lower Miocene sandstones and siltstones of the Gulf Coast are comprised of fluvial-deltaic deposits that were sourced primarily from the ancestral Red River and Mississippi River systems. Lower Miocene deposits prograde the continental margin approximately 65 km to 80 km during the 8 mega annum (Ma) depositional episode and are bound within the underlying Siph Dav shale and overlying Amph B shale (Galloway W. E., 2008).

In 2012, the U.S. Geological Survey (USGS) assessed the carbon dioxide storage resources of the Gulf Coast and determined that the Lower Miocene SAU covers an area of 8.43 million acres ± 10%. Detailed USGS regional mapping suggests that the gross sandstone thickness of the Lower Miocene SAU averages 3,100 feet (ft) ± 800 ft with an average net sand thickness of 1,150 ft ± 500 ft (Roberts-Ashby, et al., 2012).

The USGS also conducted a porosity and permeability analysis of Neogene reservoirs from production data reported by Nehring Associates, Inc., in 2010. The analysis reviewed 432 porosity measurements and 259 permeability measurements from petroleum reservoir averages to approximate the average porosity and permeability of the complete Miocene SAU. The report concluded that Miocene reservoirs along the U.S. coastal plain have an average porosity of 28% ± 4% and an average permeability of 500 millidarcy (mD). The report acknowledged that permeability varies significantly within the data set, like other geologic formations, with the permeability of some reservoirs reported as low as 20 mD and others as high as 8,000 mD. The porosity and permeability averages were modeled with a mean burial depth of 8,000 ft; however, the report clarified that porosity remained high regardless of burial depth (Roberts-Ashby, et al., 2012).

Upper Confining Zone: Middle Miocene Amph B Shale

The proposed Amph B upper confining zone consists of the tight, clay-rich, transgressive, shale located within the Middle Miocene geologic section. The Amph B shale is composed of calcareous mudrock deposited conformably over Lower Miocene sediments during a period of first-order marine transgression. Periods of first-order marine transgression tend to be associated with eustatic highs and deposition of extensive maximum flooding surfaces capable of depositing fine-grained material across large swaths of the continental shelf. Deposition occurred widespread and coincided with the first appearance of the Amph B faunal top that indicates the boundary between the Middle Miocene and Lower Miocene depositional episodes (Meckel & Trevino, 2014). The USGS National Assessment of Carbon Dioxide Storage Resources of the U.S. Gulf Coast concluded that marine shales such as the Amph B tend to be fine-grained and serve confining zones between periods of regressive deposition associated with porous sand and even silt deposition. This assessment is supported by the fact that 95% of oil production and 87% of gas production in Texas state waters occur below the Amph B, demonstrating that the shale is capable of containment. The Amph B shale and maximum flooding surface represent the thickest confining zone within the total Miocene section (Roberts-Ashby, et al., 2012).

Regional Shale Beds

Deposition of the Lower Miocene regressive sequence was interrupted by two periods of marine transgression. These regional shale beds are associated with the *Robulus L* and *Marginulina Asc (Marg Asc)* biochronozones, as was depicted in Figure 1-4 (page 10) (Treviño & Rhatigan, 2017). The Lower Miocene section contains similar lithology and petrophysical properties within the section and across the Titan Project; therefore, for the purposes of this permit application, the injection zone is limited to one single interval (Roberts-Ashby, et al., 2012).

1.3. Site Geology

Based on the modeled extents of the injection plume and pressure front, the Titan Project area of review (AOR) is located in Jefferson County, Texas, [redacted] as shown in Figure 1-5.

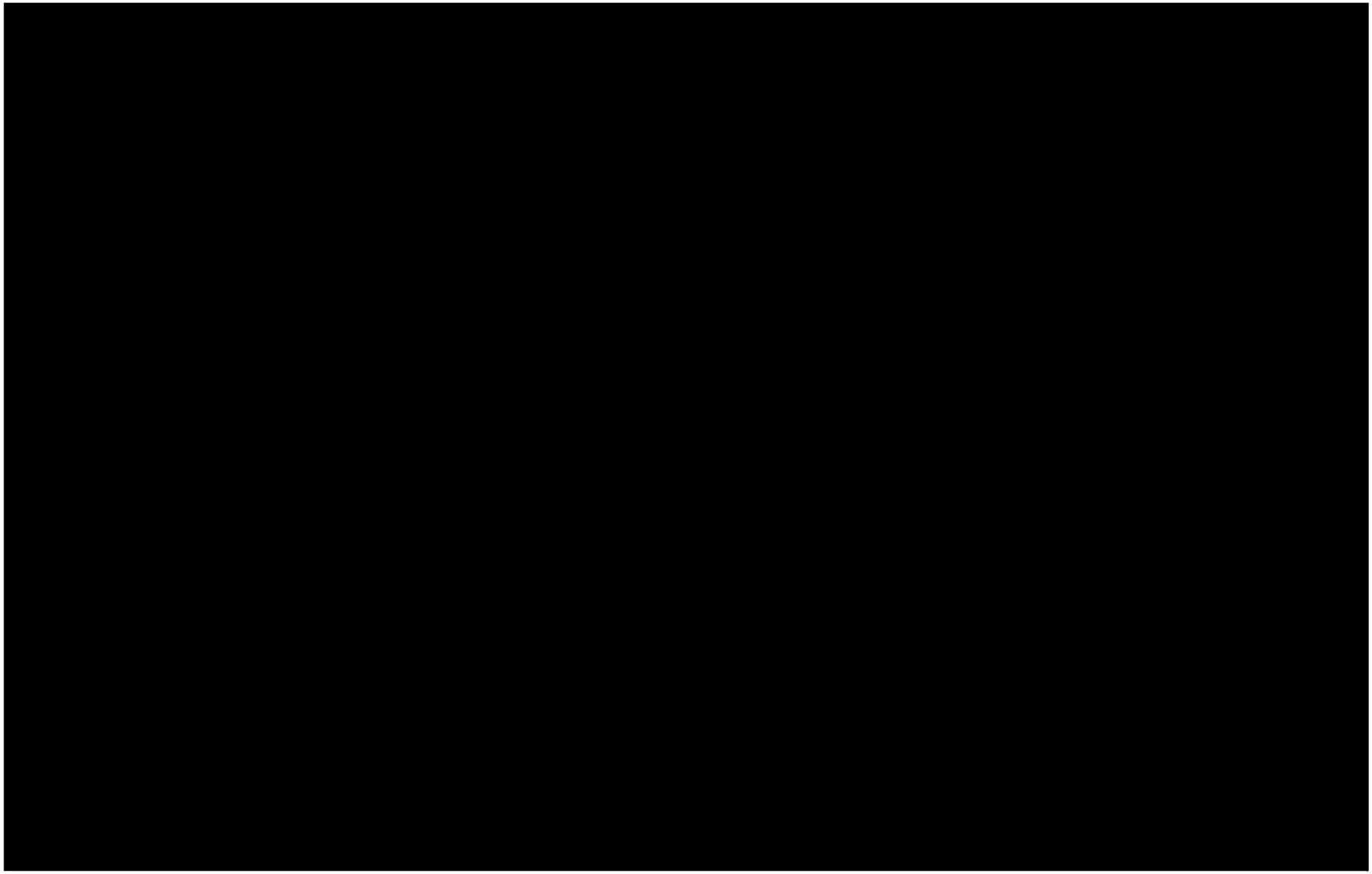

Figure 1-5 – Overview Map of Titan Project

Titan intends to obtain additional information to enhance the initial site-characteristics assessments, based on the prior research conducted across the project area, by implementing a stratigraphic test well, Prometheus No. 1, [redacted] The drilling of this proposed stratigraphic test well will yield site-specific subsurface information, enriching the data set acquired from previous investigative endeavors.

Table 1-1 offers a comprehensive list of wireline logs slated for acquisition during the drilling of Prometheus No. 1. These logs include projected top and base depths tailored to provide precise data relevant to the site characterization objectives. The top and base depths of investigation may be adjusted during drilling to accommodate the analysis of the intended target formations.

Table 1-2 outlines the expected intervals for coring operations during the drilling of the Prometheus No. 1 test well. These coring operations aim to gather mineralogical, fluid composition, petrophysical, mechanical, and geochemical data, which will contribute to the site-specific characterization efforts.

Table 1-1 – Openhole Logging Plan

Trip	Hole Section	Logging Suite	Openhole Diameter (in.)	Use	Cronos No. 1 Depths (ft)	Rhea No. 1 Depths (ft)
1	Surface Section	Spectral Gamma Ray, Resistivity, Bulk Density, Neutron Porosity, Spontaneous Potential	[redacted]	Rock properties; fluid identification and proportion (determining the Underground Source of Drinking Water (USDW) base); lithology/permeability identification	[redacted]	[redacted]
2		Multi-arm Caliper		Cement volume calculations		
3	Intermediate Section	Spectral Gamma Ray, Resistivity, Bulk Density, Neutron Porosity, Sonic/Acoustic, Spontaneous Potential		Synthetic seismogram tie; rock properties and geomechanics; fluid identification and proportion; lithology/permeability identification		
4		Multi-arm Caliper		Cement volume calculations		
5	Long String Section	Spectral Gamma Ray, Resistivity, Bulk Density, Neutron Porosity, Sonic/Acoustic, Spontaneous Potential		Synthetic seismogram tie; rock properties and geomechanics; fluid identification and proportion; lithology/permeability identification		
6		Sonic Scanner (Geomechanics Basket) – Four Arm Caliper-Borehole Imager		Rock properties and geomechanics/stress conditions/cement volume calculations		
7		Formation Fluid Tester		Formation fluid properties/rock properties		
8		MDT Stress Testing with MDT Dual Packer		Geomechanics		
[redacted]						

*MDT – modular formation dynamics tester
TD – total depth

Table 1-2 – Planned Core Intervals, Prometheus No. 1

Stratigraphic Unit	Zone
[redacted]	

*Rotary sidewall cores will be obtained in these sections.

Information regarding reservoir characteristics and geological properties for both the injection and confining zones is sourced from various data repositories, encompassing proprietary, licensed, subscribed, and publicly available data sets. These repositories include the Texas Railroad Commission (TRRC) online database, Louisiana Department of Natural Resources (LDNR) Strategic Online Natural Resources Information System (SONRIS), Texas Bureau of Economic Geology (BEG), IHS LogNet, Enverus, TGS R360, and published research—from which a comprehensive understanding of the general geologic setting and lithological attributes is derived. Additionally, where possible, this understanding is substantiated by offset wellbore and core data. The expected conditions across the proposed sequestration project site are projected through petrophysical analyses of 56 wells featuring wireline logs, as shown in Figure 1-6. This data set includes logs from 14 wells with digitized curves (Log American Standard Code for Information Interchange (ASCII) Standard (LAS)) logs, as well as production data from wellbores in proximity to the proposed well site.

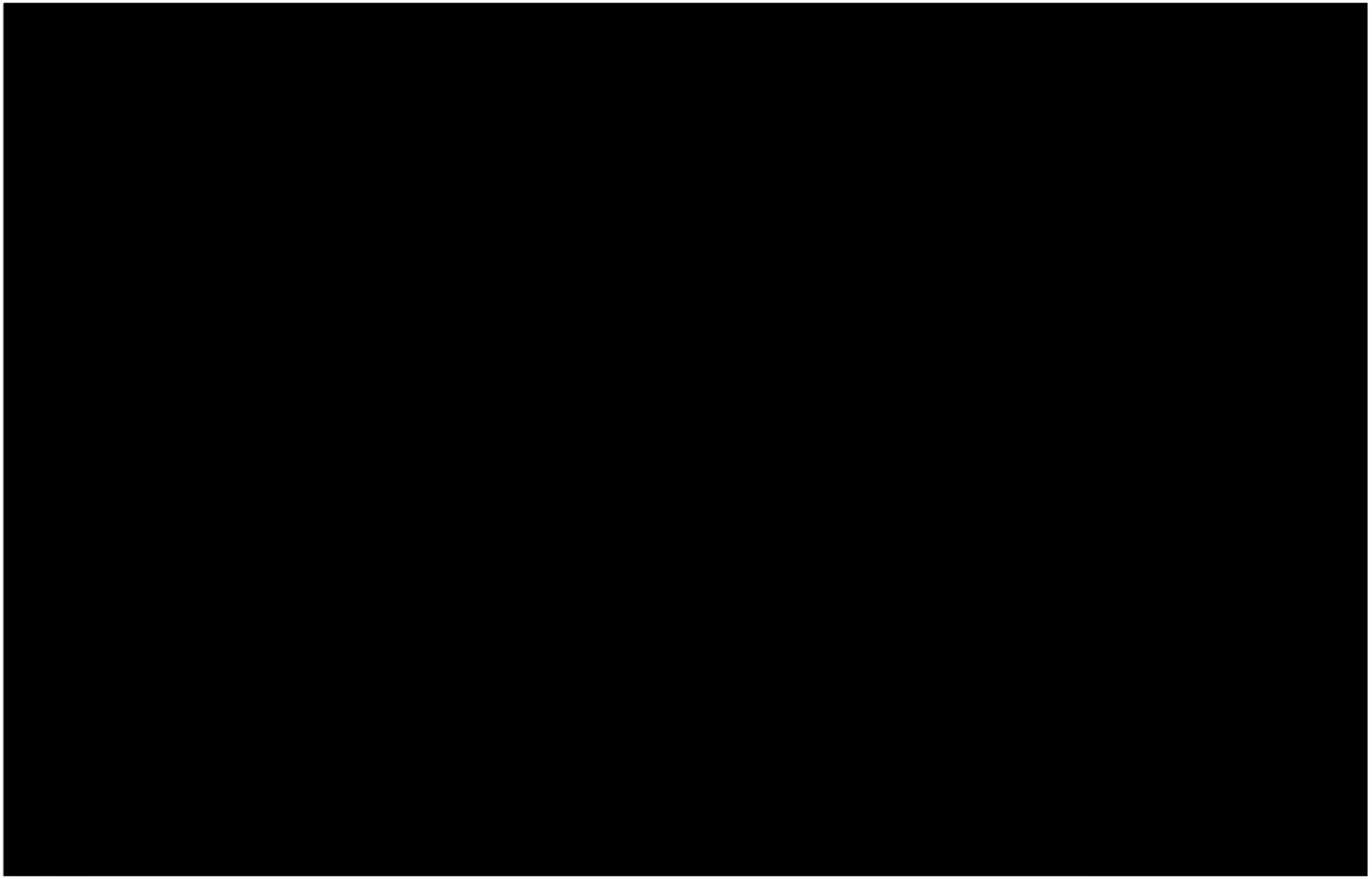

Figure 1-6 – Well Log Data

The [redacted] is the nearest offset wellbore relative to the proposed Titan Project location. [redacted] Table 1-3 provides information on the depths and corresponding thicknesses of the upper confining unit, injection zone, and lower confining unit—all as encountered within the well. Additionally, Figure 1-7 presents a stratigraphic column detailing lithologies, formations, and depth profiles observed in the Iles well.

Table 1-3 – Injection and Confining Zones as Encountered in [redacted]

System	Group/Formation Name	Injection/Confining	Formation Top-Bottom (ft)	Thickness (ft)
Miocene	Amph B	Upper Confining	[redacted]	
Miocene	Lower Miocene	Injection		
Miocene	Siph Dav	Lower Confining		

*Depths in true vertical depth (TVD)

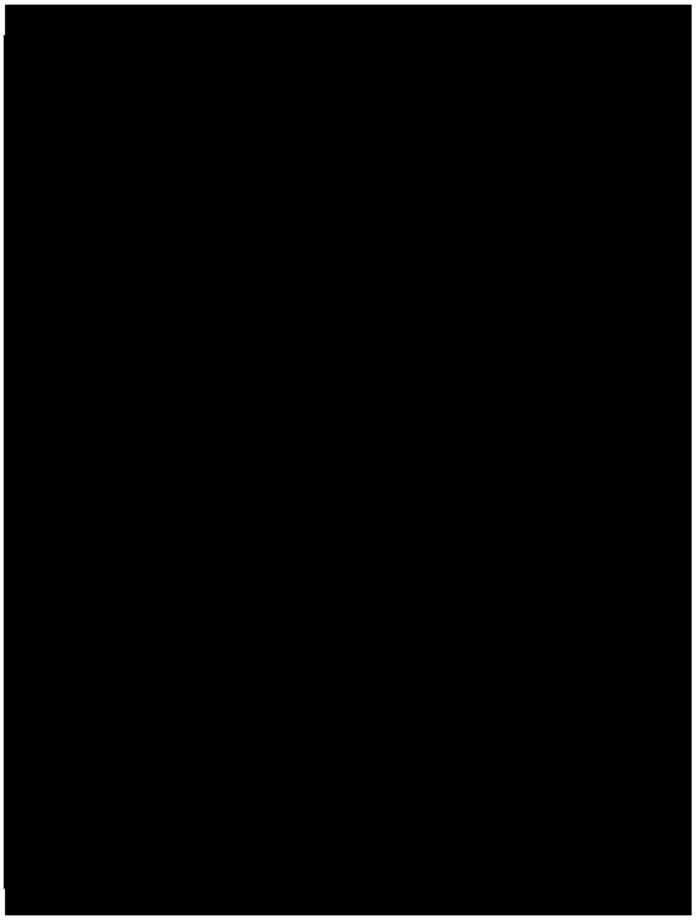

Figure 1-7 – Stratigraphic column from [redacted] Shallower depths than the log interval were referenced from the BEG surface casing estimator. (https://coastal.beg.utexas.edu/surfacecasing/#!/ for [redacted]).

1.3.1 Injection Zone

The injection zone was created from sediments deposited during the Lower Miocene period. These sediments include two shales linked to maximum flooding surfaces, namely *Robulus L* and *Marg Asc*, as identified in the study conducted by (Olariu, DeAngelo, Dunlap, & Treviño, 2019). Figure 1-8 illustrates the relationship between the injection zone and the stratigraphic chart.

The early Miocene was characterized as a period of "relative paleogeographic stability" (Galloway W. E., 2008). After the Anahuac transgression, the "Houston sediment dispersal axis was abandoned" in favor of the Red River axis, which supplied sediment to the Calcasieu delta (Galloway W. E., 2008). Figure 1-9 (page 21) is a depiction of the proposed project location in relation to the paleogeography of the early Lower Miocene, showing the proposed location falling within the Calcasieu delta. Sediment sourcing within the Lower Miocene was greatly influenced by the uplift of the Edwards Plateau and the influx of "reworked Cretaceous and older Cenozoic debris" (Galloway W. E., 2008). The Calcasieu delta "prograded on to a highly unstable, collapsing continental margin, creating an extensive, sand delta-fed apron" (Galloway W. E., 2008).

The Lower Miocene is broken into two subsections, LM1 and LM2, separated by the transgressive marine shale *Marg Asc*. Figure 1-8 is a stratigraphic column depicting this depositional relationship, where LM1 is the initial deposition of the early Miocene with the LM2 closing out the Lower Miocene deposition cycle. Although southern deltas within the Lower Miocene saw reduced sediment influx during LM2, the Calcasieu delta continued through LM2, allowing for ample sand sediment to be present throughout the Lower Miocene (Snedden & Galloway, 2019). Figure 1-10 (page 22) is a paleogeographic map of the LM2 with the proposed project location depicted by the red star.

The ongoing influx of sediment mass is evident in the net injectable-sand presence in the AOR. The BEG conducted a study to assess the suitability of Lower Miocene sediments for injection along the Texas coast. Within this study, sands meeting specific reservoir-quality criteria, as determined by the spontaneous potential (SP) curve, were identified as potential injection sands. Figure 1-11 (page 23) displays an isopach map of net injectable sands derived from the study, highlighting that the AOR has some of the highest onshore net injectable-sand values along the Texas coast. Gross thickness of the injection zone within the proposed injection area ranges from [redacted], as shown in *Appendix B-10* along with Figure 1-12 (page 24).

Throughout the Lower Miocene deposition, the Calcasieu depocenter displayed minimal variation, with a slight westward shift during LM2. This consistency in depocenter location, combined with a steady source of sediment throughout the Lower Miocene, has resulted in a uniform mineralogical composition within the entire injection zone. Lower Miocene sediments primarily consist of a mix of sandstones, siltstones, and shale layers. This geological composition is visually represented in Figure 1-13 (page 25), which presents an openhole log of the offset well [redacted]). The paleo tops depicted were correlated from offset paleo picks. The lithology is depicted in track one through the Vshale curve, where shale and

sand intervals are shaded based on the Vshale values calculated from the SP curve. *Section 1.5* contains additional details on how the Vshale values were computed.

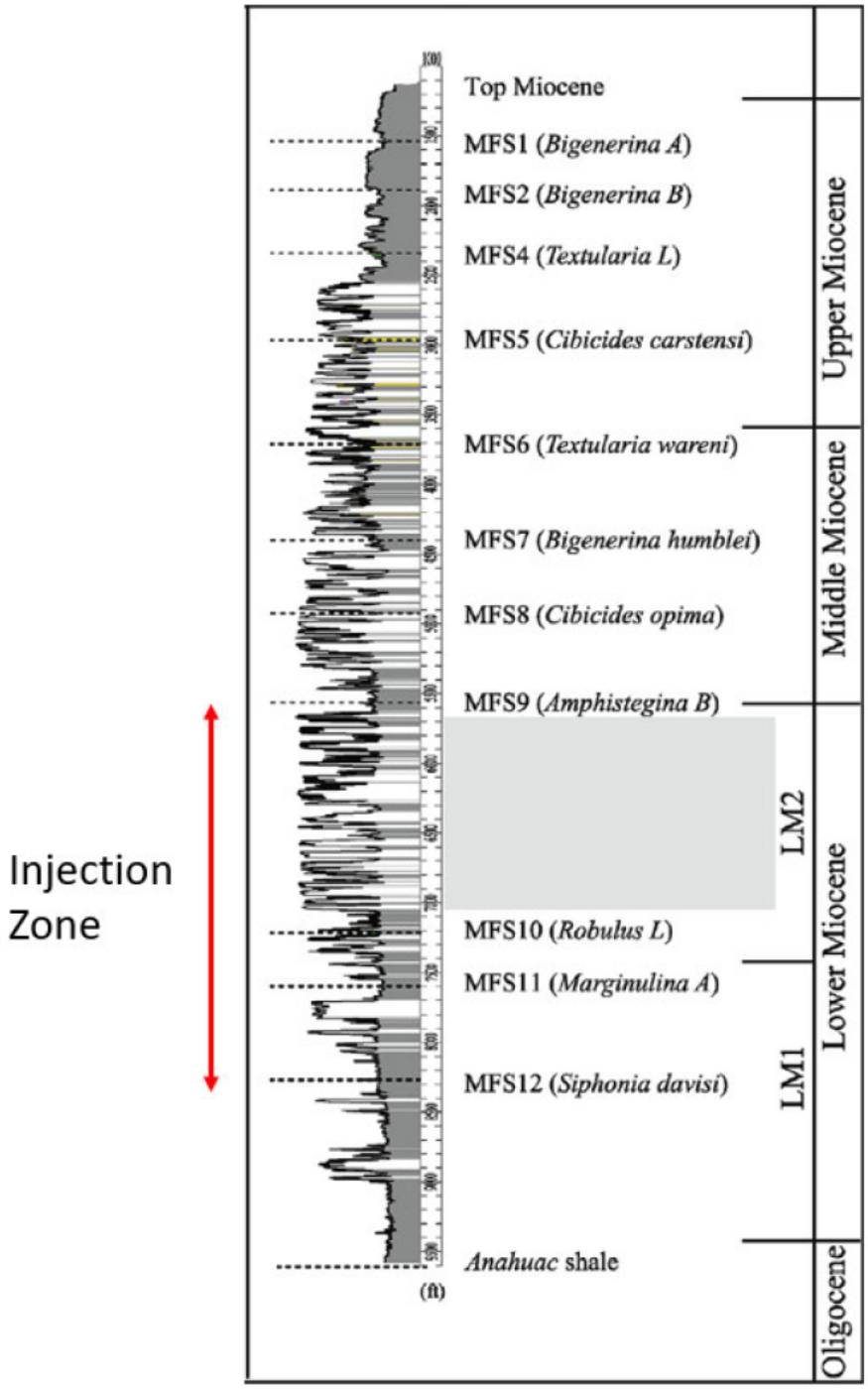

Figure 1-8 – Injection Zone in the Gulf of Mexico, Miocene Stratigraphic Section (Olariu, DeAngelo, Dunlap, & Treviño, 2019)

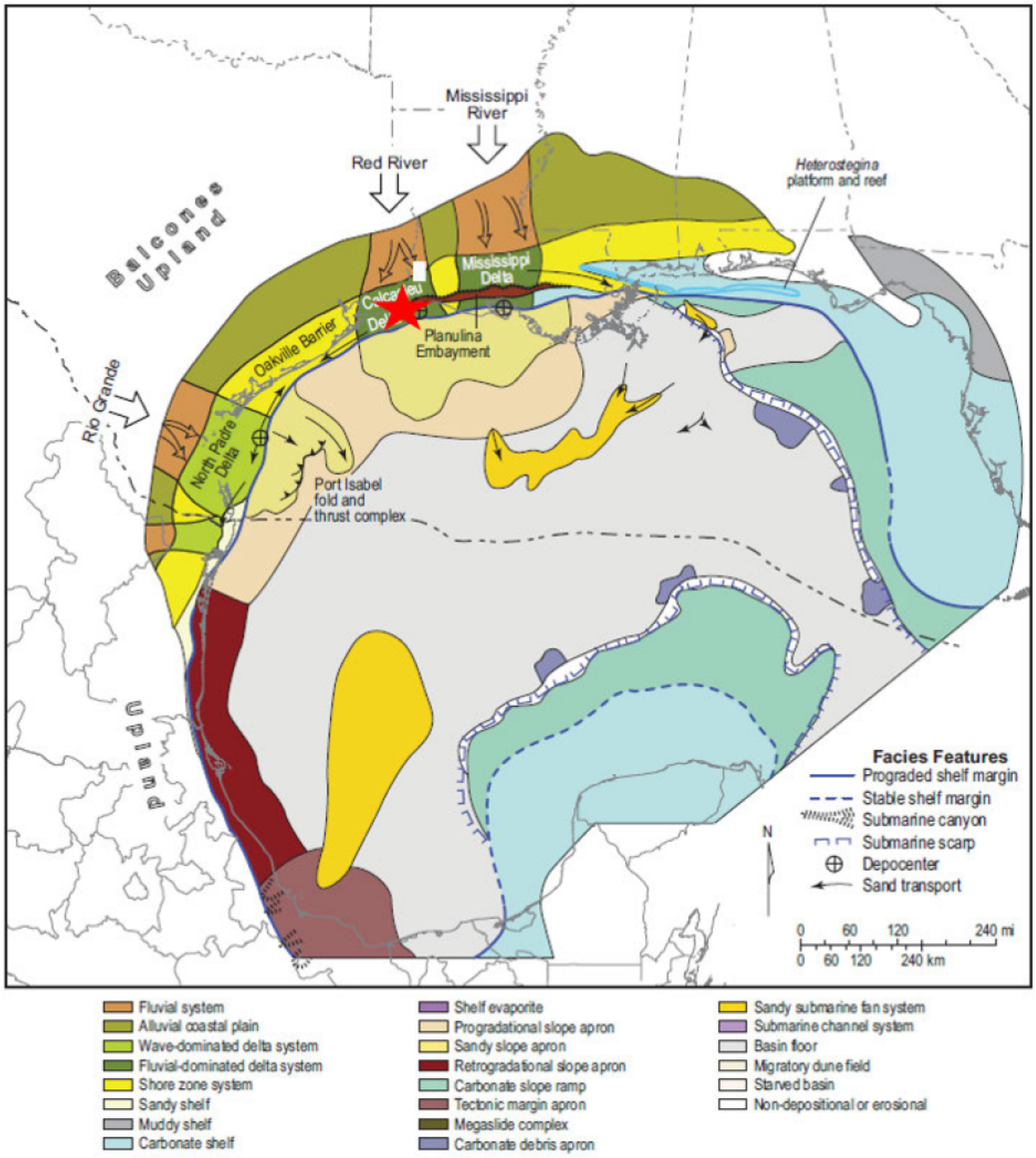

Figure 1-9 – Gulf of Mexico paleogeography during the Lower Miocene (LM1) (Snedden & Galloway, 2019). The red star denotes the project location.

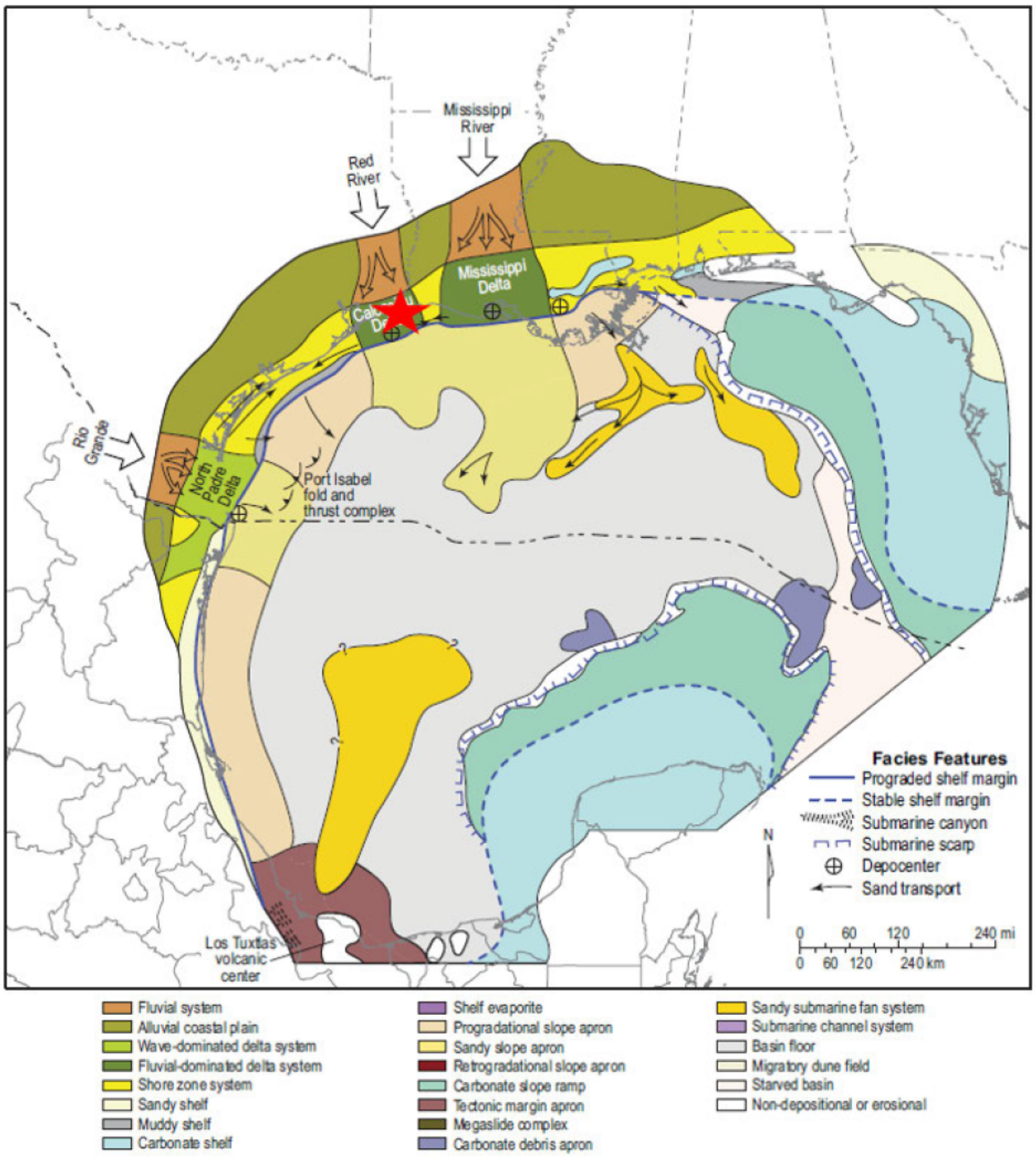

Figure 1-10 – Gulf of Mexico paleogeography during the Lower Miocene (LM2) (Snedden & Galloway, 2019). The red star denotes the project location.

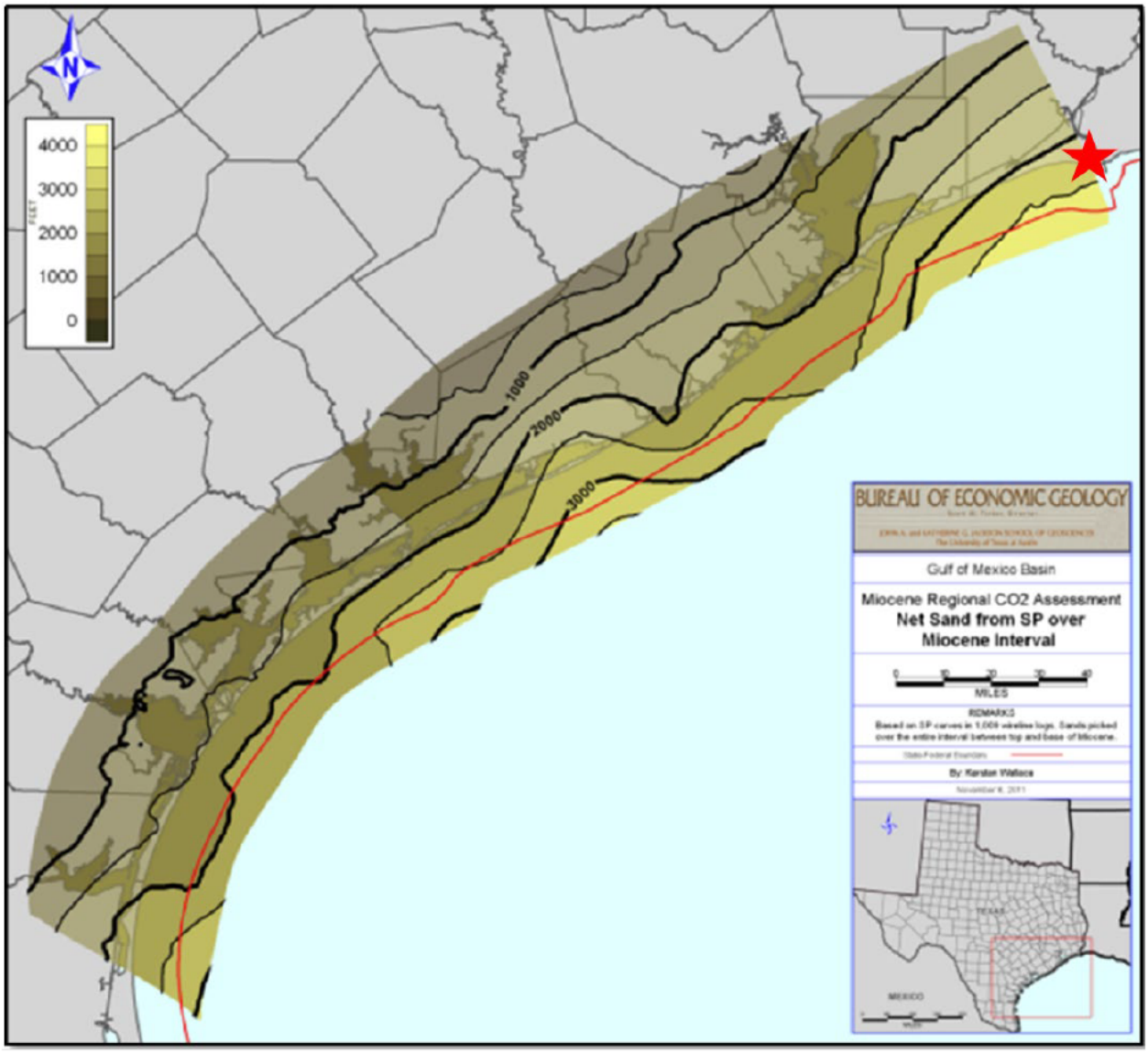

Figure 1-11 – Net sand isopach map from the BEG study. The red star represents the Titan Project location (Meckel & Trevino, 2014).

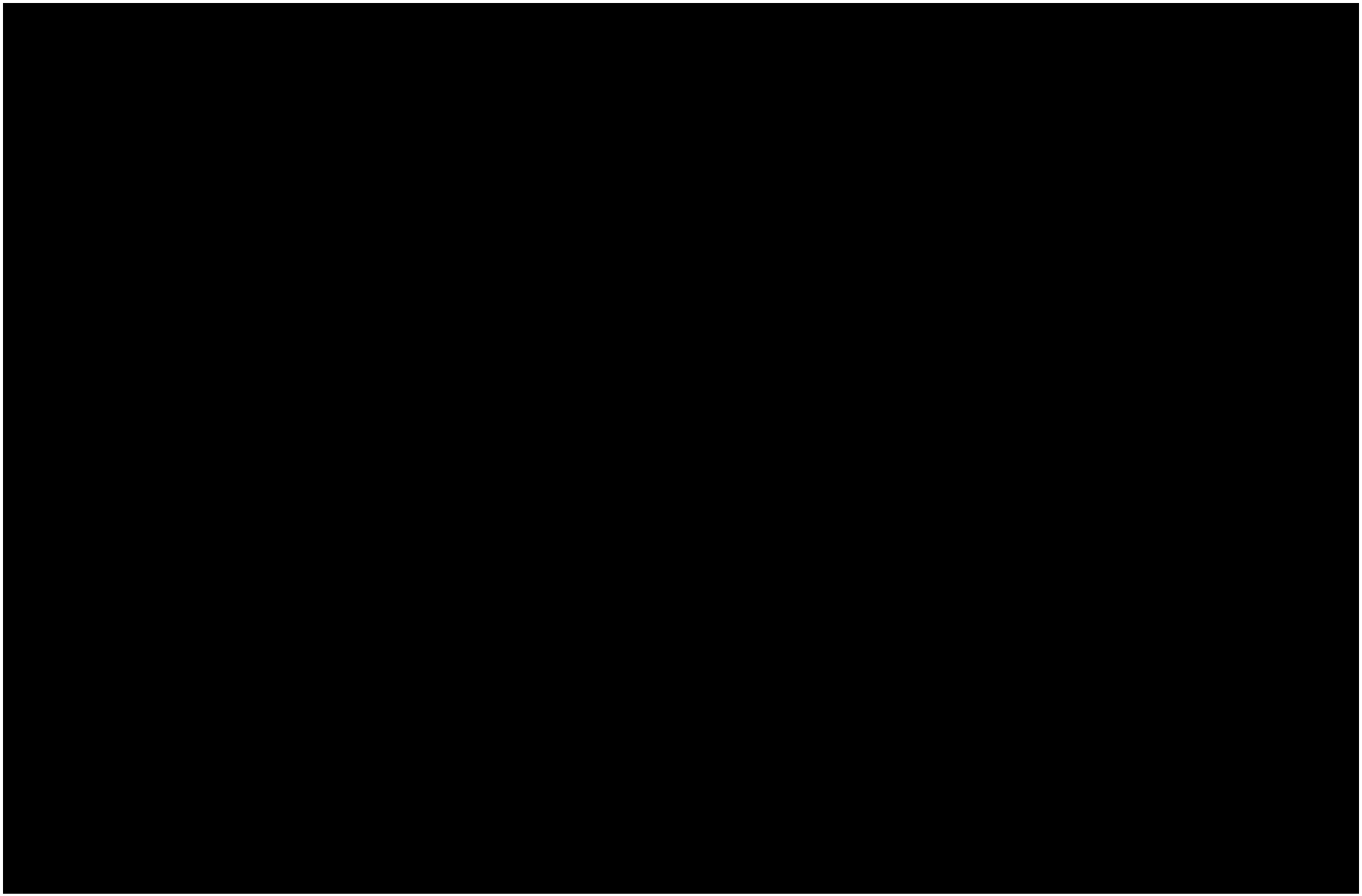

Figure 1-12 – Gross Injection Zone Isopach Map

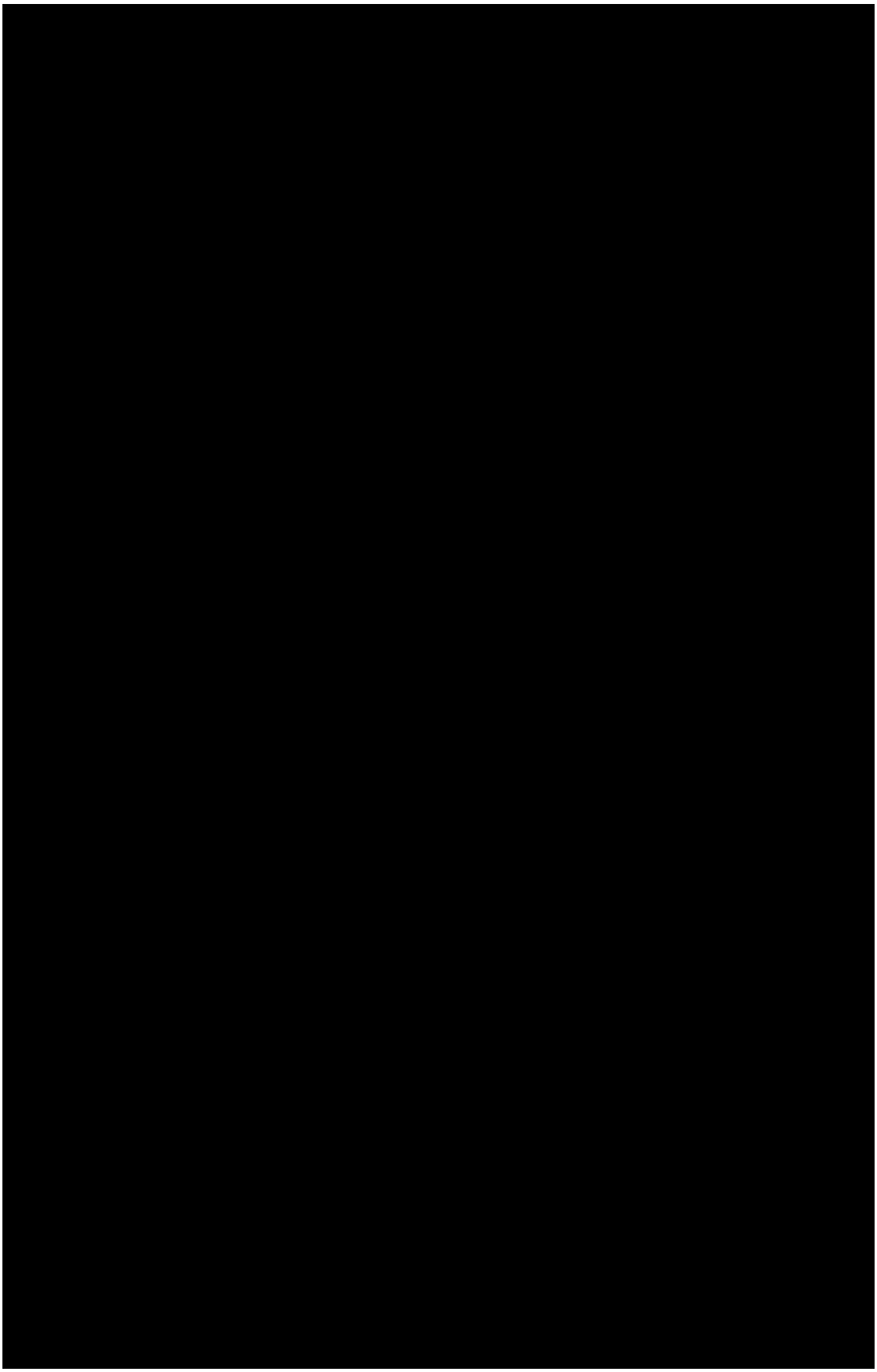

Figure 1-13 – Openhole log of [redacted] depicting the proposed injection zone.

Though limited core data of the stratigraphic section of interest are available for analysis, Lower Miocene core sampled from High Island well 24L No. 9 (42-708-30316) in the previously referenced BEG study were analyzed. [redacted] Conventional core, 106 ft in length, was taken over a 360-ft section that included calcareous mudstone, marine shale, medium coarse-grained sandstone, and interbedded shale and fine-grained sandstone. These samples resemble the primary lithofacies that will be encountered throughout the injection and confining zones. Therefore, it can be assumed that similar mineralogy will be encountered throughout the injection zone.

Samples were taken from these conventional cores for multiple analysis including thin section, X-ray diffraction (XRD), and scanning electron microscopy (SEM). Results from the XRD analysis in the injection sands within the Lower Miocene are shown in Figure 1-15 (page 28). Large concentrations of quartz and low concentrations of clay were examined and are expected throughout the Lower Miocene, within the sand intervals. A thin section displaying the grain distribution and excellent porosity (represented in blue) within a sandstone sample representative of sandstones targeted for injection is displayed in Figure 1-16 (page 28).

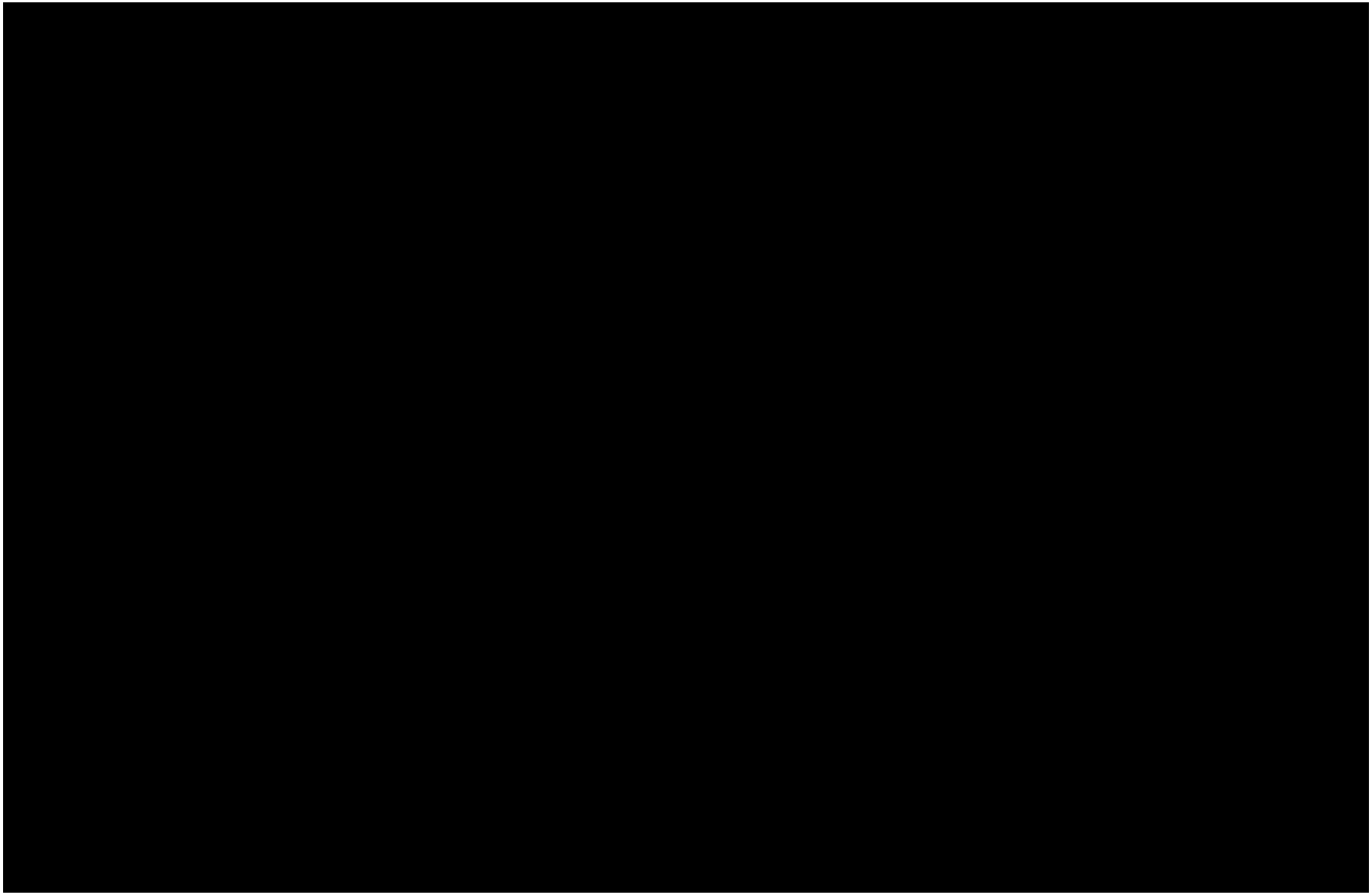

Figure 1-14 – Map depicting High Island core data in relation to the proposed Titan injection wells.

Well	Depth (ft)	Quartz	Kaolinite	Calcite	Illite	Plagioclase	K-Feld
High Island 24L #9	8555	48.49	3.73	1.62	4.65	19.61	21.92
High Island 24L #9	8560.5	49.14	3.58	1.83	5.03	18.85	21.57
High Island 24L #9	8570.6	51.88	2.20	1.99	4.85	18.74	20.34
High Island 24L #9	8572	50.86	2.74	2.29	4.98	18.82	20.31

Figure 1-15 – XRD analysis from High Island core data within the sand intervals (Meckel & Trevino, 2014).

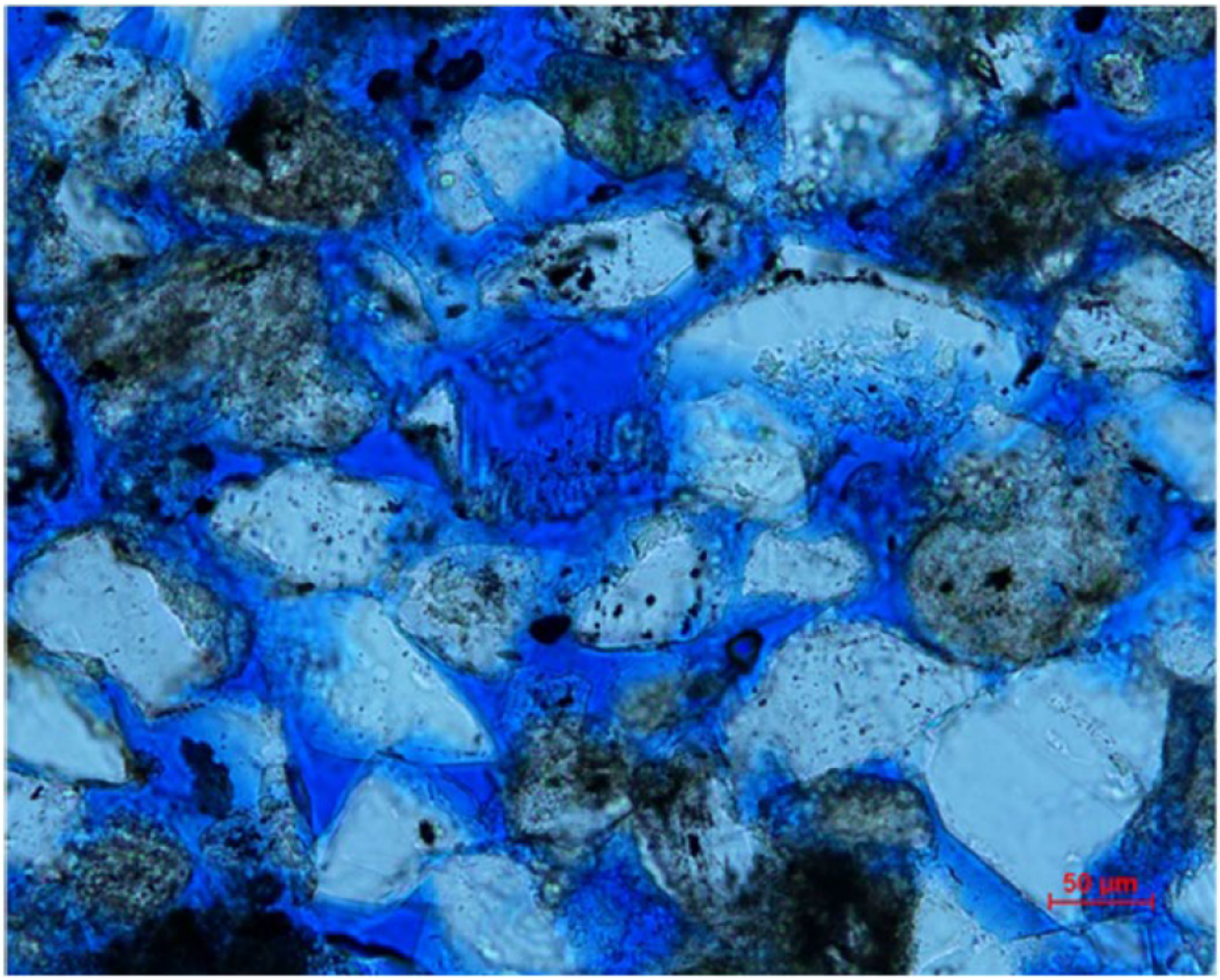

Figure 1-16 – Thin section of High Island core depicting high porosity (in blue) within the injection sands (Meckel & Trevino, 2014).

1.3.2 Upper Confining Zone

The Amph B shale is recognized as a regional marine shale that marks the lower boundary of the Middle Miocene and the upper boundary of the Lower Miocene (Galloway, 2000). Research conducted by the BEG has highlighted the Amph B's significance as a crucial confining layer for CO_2 injection, attributed to its extensive lateral presence and effective sealing properties (Treviño and Rhatigan, 2017). Further proof of the sealing properties of the Amph B is supported by the

fact that, as noted earlier, 95% of oil production and 87% of gas production in Texas state waters take place beneath Amph B, highlighting its effectiveness as a regional sealant (Meckel & Trevino, 2014). This shale is the result of a flooding event approximately 16 million years prior to the initial formation of the West Antarctic Ice Sheet. The Amph B transgression disrupted episodes of deltaic progradation dominated by sandstone and shore-zone advances, towards the end of the early Miocene and the beginning of the Middle Miocene (Meckel and Trevino, 2014).

Figure 1-17 displays an openhole log image of the upper confining zone in the [redacted] Within this image, [redacted]. Core-based analyses make it apparent that the Lower Miocene mudrocks are rich in clay and possess a good sealing capacity for CO_2 storage in the underlying sandstone units. The sealing effectiveness of the samples under study exhibits a positive association with the clay content and the presence of calcite cementation. Notably, mudstone samples with a higher clay content tend to exhibit greater capillary entry pressure and smaller pore-throat dimensions compared to the underlying sandstones. The SEM imaging reveals that these claystone samples predominantly feature isolated intraparticle pores that do not effectively interconnect to form pore networks (Meckel & Trevino, 2014).

Although cores in this study are not within the Amph B itself, similar mineralogic and lithologic characteristics are expected to be encountered within the Amph B (Meckel & Trevino, 2014). Figure 1-18 (page 31) represents the results from XRD analysis on the mudstones samples from the High Island core. [redacted]

The gross thickness of the Amph B ranges from approximately [redacted] within the project AOR. (Gross isopach maps of the Amph B are provided in *Appendix B-8*). Thin sand interbeds occur within the Amph B but will have no effect on the confining nature of the formation—due to the high clay content above and below the interbedded sand prohibiting an interconnected pore system that would induce transmissibility.

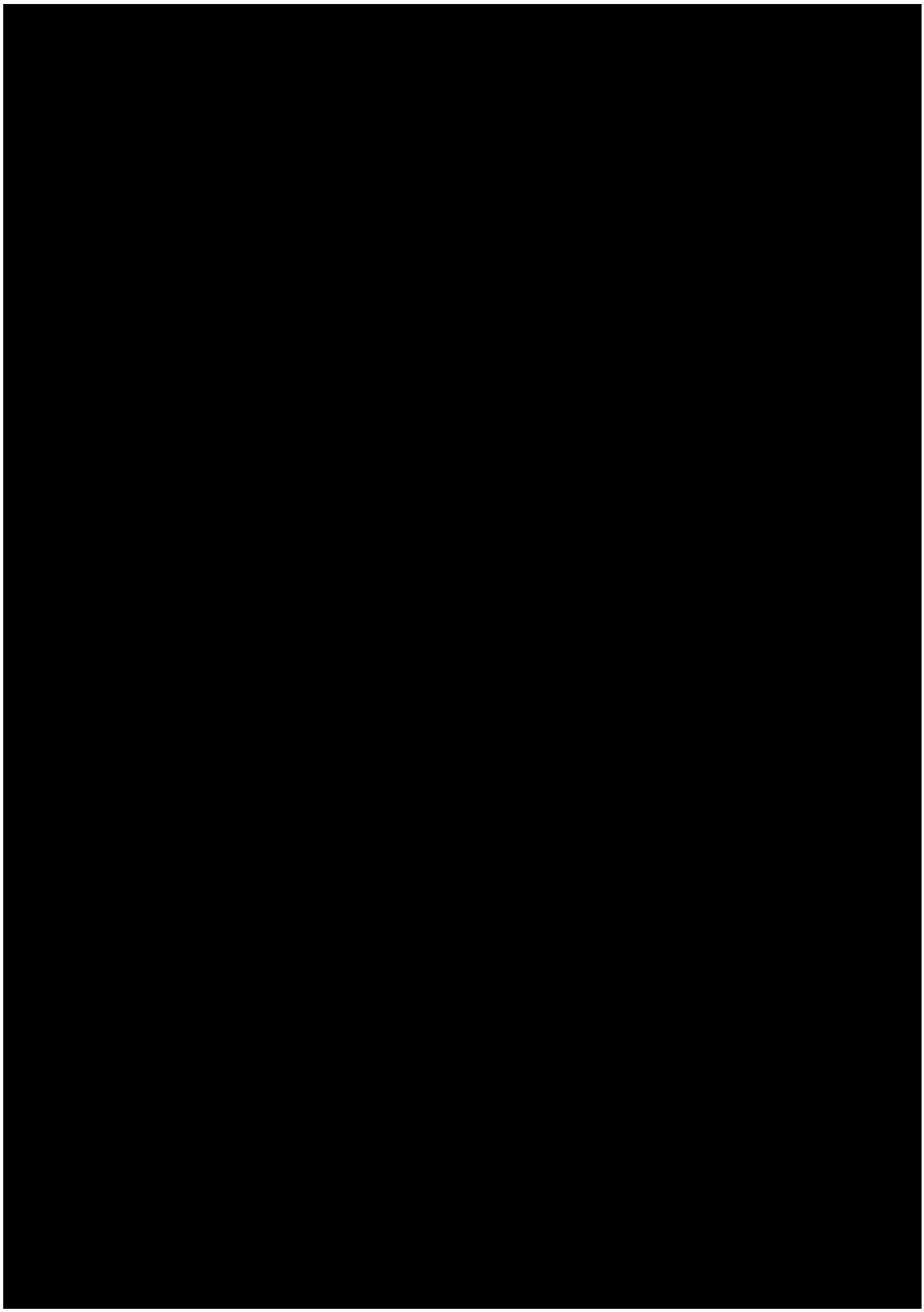

Figure 1-17 – Openhole log of [redacted] depicting the proposed upper confining zone.

Depth (ft)	Quartz	Kaolinite	Calcite	Illite	Albite	K-feldspar	Chlorite	Total
Well High Island 24L #9, API: 427083031600								
8403.1	23.7	12.7	15.8	22.5	6.7	18.6		100.0
8408.5	18.9	13.9	19.4	26.0	6.2	15.5		100.0
8412.9	27.0	10.3	11.2	21.6	9.5	20.4		100.0
8421	20.5	15.3	13.8	32.4	7.7	10.4		100.0
8421*	22.0	15.6	14.1	30.3	6.9	11.1		100.0
8423.1	20.4	15.6	13.3	33.9	7.0	9.8		100.0
8427.4	41.4	7.2	5.1	15.2	16.2	15.0		100.0
8429.5	40.1	9.9	2.4	20.7	13.4	13.5		100.0
8429.5*	42.5	7.7	3.1	19.1	14.5	13.1		100.0
8481.6	34.8	9.9	7.2	21.1	13.0	14.0		100.0
8481.6*	34.6	9.4	7.4	22.6	13.1	13.0		100.0
8485	29.8	10.7	11.5	24.2	11.0	12.8		100.0
8489	26.7	12.9	10.2	28.0	10.2	12.0		100.0
8492	36.0	2.9	20.5	4.7	17.5	18.4		100.0

Figure 1-18 – XRD analysis of mudstone samples within the High Island core (Meckel & Trevino, 2014).

1.3.3 Lower Confining Zone

The lower confining zone is directly associated with the maximum flooding surface of the Siph Dav. The High Island core data previously referenced was taken in the Siph Dav. Therefore, mudstones sampled in the High Island core data will adequately portray the mineral and lithologic conditions of the lower confining zone. Figure 1-18, as noted above, is an XRD analysis of the mudstone samples within the Siph Dav. Unlike the upper confining zone, the presence of illite is expected at these deeper burial depths. A thin section is shown in Figure 1-19 depicting the 8,408 ft sample from the High Island core, "showing abundant clay and low porosity, therefore, high sealing capacity" (Meckel & Trevino, 2014).

The base of the lower confining zone is bounded by the X Sand, a regional Lower Miocene sand. Figure 1-20 (page 33) displays the lower confining zone from the [redacted] The VSHL curve in the left track is a clay concentration curve based on the SP curve, shaded to represent sand and shale content, and the ILD curve in the right track is the measured deep-resistivity log. As evidenced through the response of both curves, the Siph Dav is a continuous shale/mudstone that will have optimal sealant characteristics.

The gross lower confining zone is [redacted] thick in the [redacted] and varies from [redacted] within the AOR. Structure and isopach maps of the Siph Dav are included in *Appendix B-9*.

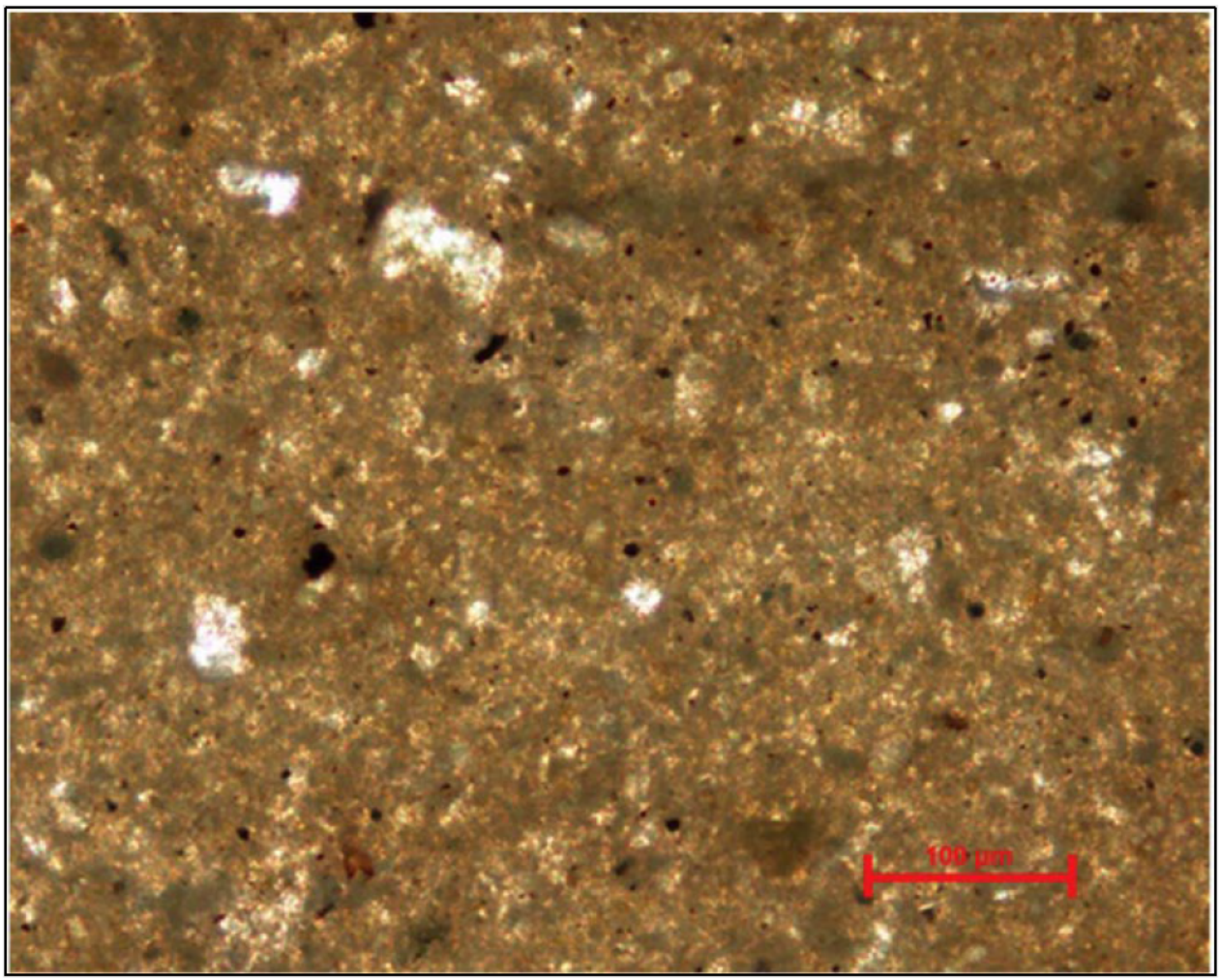

Figure 1-19 – Thin section of mudstone showing high clay content and low porosity from High Island core (Meckel & Trevino, 2014).

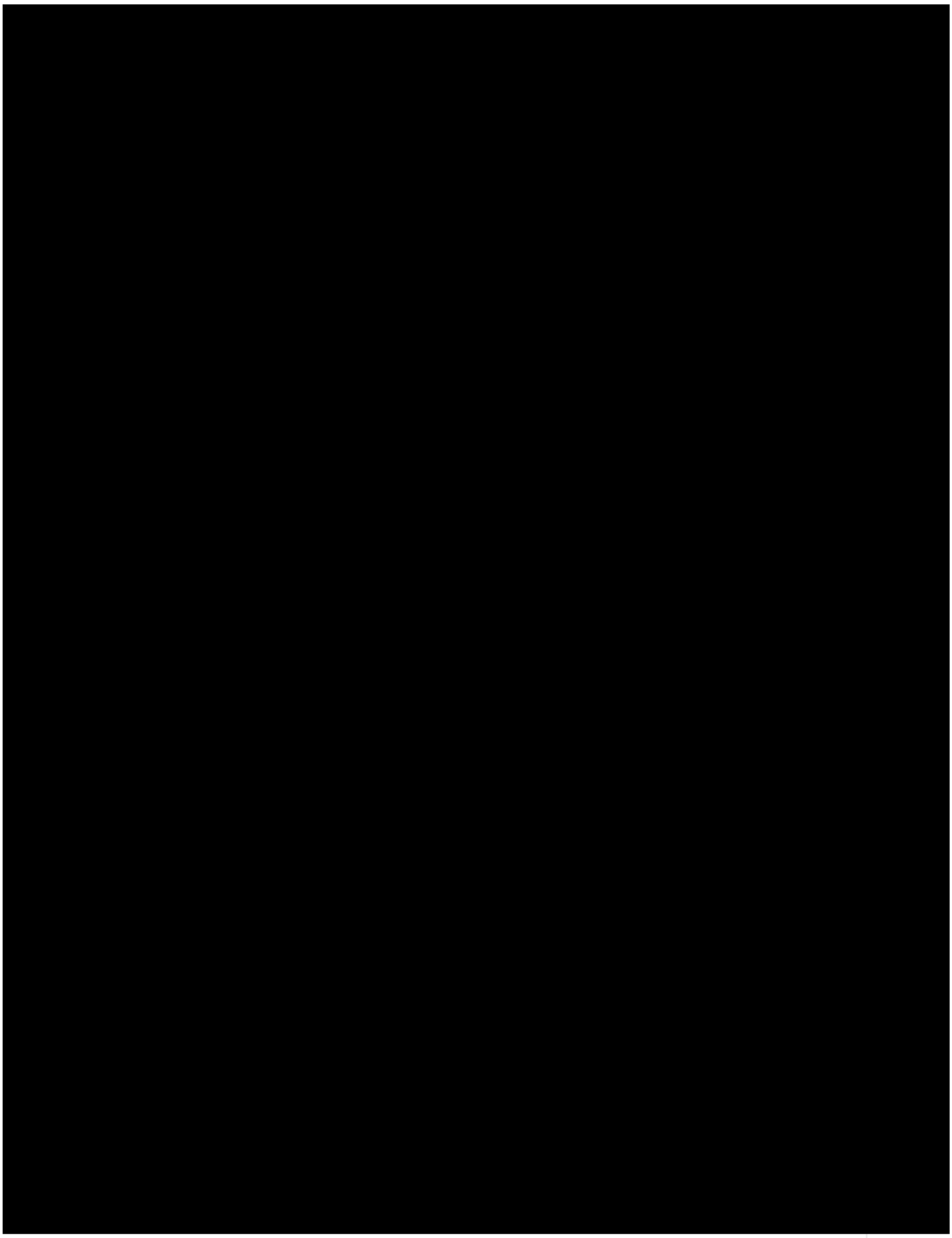

Figure 1-20 – Openhole log of [redacted] depicting the proposed lower confining zone.

1.3.4 Geologic Structure

1.3.4.1 Data sources

Structural dips of sedimentary strata within the injection zone were mapped using offset well control and 28 square miles (sq mi) of 3D seismic data. Subsurface control was provided from [redacted] Well information and log data were compiled for these wells from multiple data sources including TGS, Enverus, IHS, and the TRRC. Professional geologists and engineers cross-referenced data sets to ensure completeness and accuracy. Directional surveys were available and used for all deviated wellbores. The compiled well database was imported into Petra® for mapping. Raster logs were available for [redacted] of the wells and digital LAS curves were incorporated from [redacted] of those wells. Tops were correlated across the region based on log response and then integrated with the 3D seismic data for the structural interpretation. These tops were sourced from offset field papers to assist in regional stratigraphic correlations. Structure maps, cross sections, and isochore maps with further detail are included in *Appendices B-1* through *B-12.*

About 28 sq mi of 3D surface seismic data were obtained under license by Titan and used for the current interpretation. This data set is a segment of the [redacted] sourced from the [redacted]

The licensed data from the [redacted]

Figure 1-21 – Location of 3D Seismic Surveys

1.3.4.2 Reflection Seismic Profiles

The 3D reflection profiles, which visualize subsurface features by highlighting differences in velocity and density, were integrated with geological formation top data obtained from subsurface well control. This integration allowed for the creation of maps outlining the designated injection and confining zones, providing insights into formation depths and the presence of any anomalies like faults. These maps are presented in Figures 1-22 through 1-24 (pages 37 through 39, respectively).

The 3D seismic data set was used to chart a sequence of Miocene-era strata, measuring approximately 3,000 ft in thickness. The quality of the seismic data is high, featuring offsets adequate for delineating the target interval within the depth range of [redacted] TVD subsea (TVDSS). Across the envisioned CO_2 storage area (in the black polygon featured in Figure 1-22), the recorded and interpreted 3D seismic data does not indicate significant alterations in the injection or confining zones via major thinning or thickening events. [redacted]

[redacted]

[redacted]

Figure 1-22 – Structure Map of the Top of Amph B

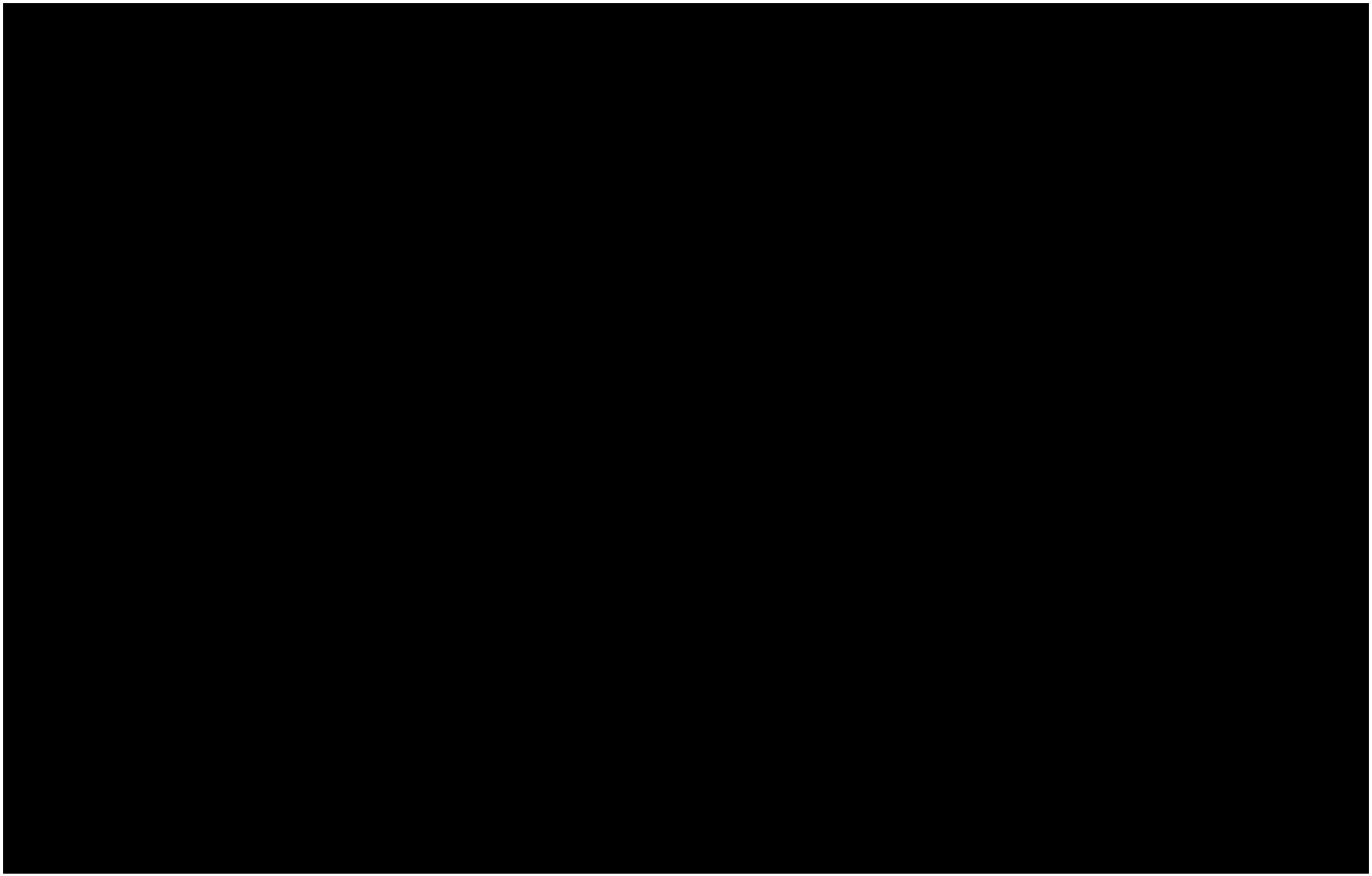

Figure 1-23 – Structure Map of the Top of the Lower Miocene

Figure 1-24 – Structure Map of the Top of Siph Dav

1.3.4.3 Velocity Control and Synthetic Seismogram

A velocity survey was used from [redacted] n Figure 1-25. The checkshot velocity information and synthetic well ties from [redacted] ere used to confirm the time-to-depth relationship of the PSTM data, illustrated in Figures 1-26 and 1-27.

Figure 1-25 – Location of well with a checkshot velocity survey (indicated by the blue circle), with wells used for synthetic ties to seismic (green circles). The red stars indicate the locations of the proposed injection wells.

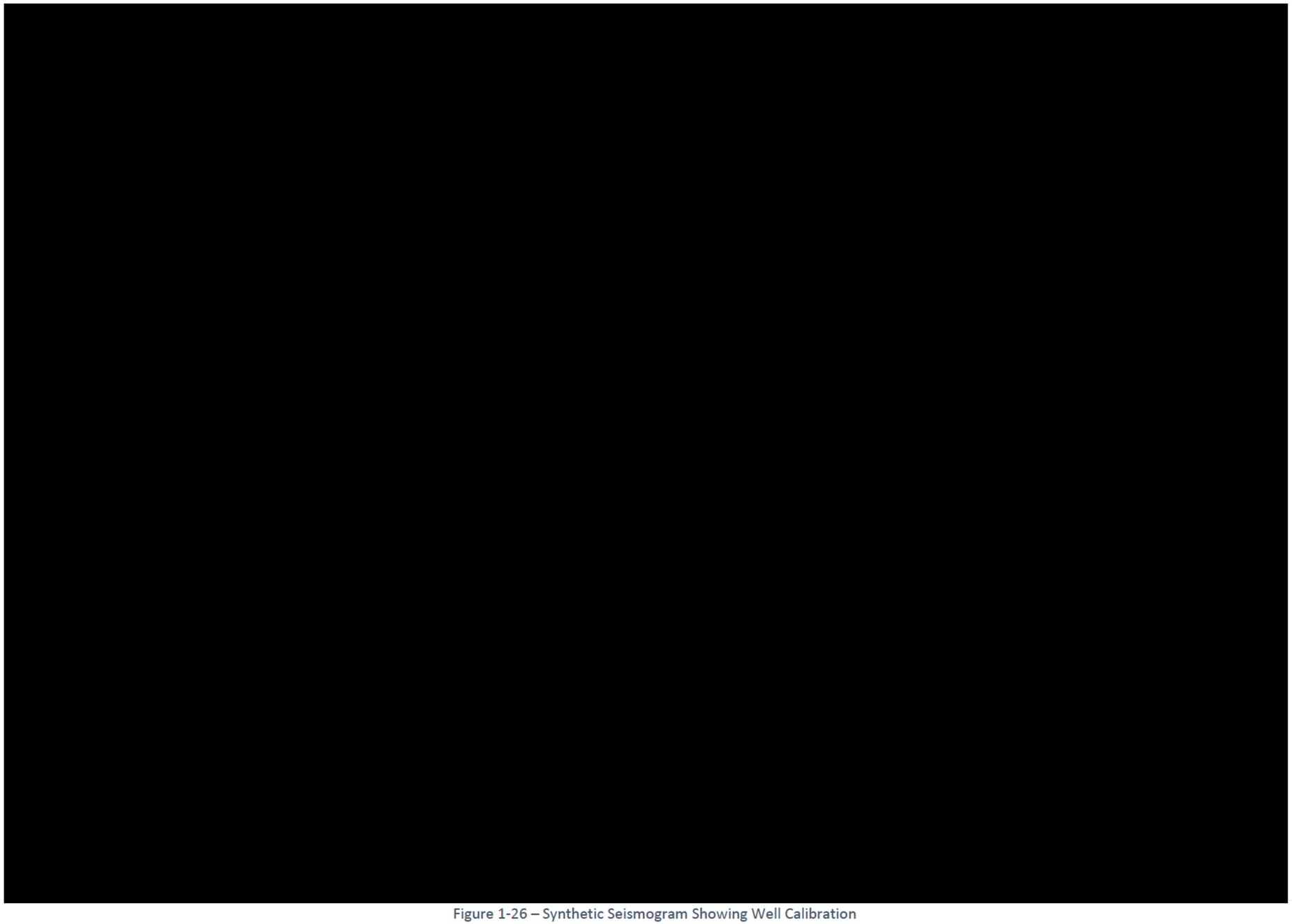

Figure 1-26 – Synthetic Seismogram Showing Well Calibration

Figure 1-27 - Seismic Line with Synthetic Well Tie

1.4. Geomechanics

1.4.1 Local Stress Conditions

Local formation stresses will be calculated by integrating mechanical rock properties from an X-dipole openhole log, calibrated with geomechanical core tests. According to published maps of crustal-stress orientation along the northern coast of the Gulf of Mexico basin, the maximum horizontal stress (SHmax) orientation is primarily parallel to the coast in an east-northeast direction near the AOR (Yassir and Zerwer, 1997; Heidbach et al., 2016).

1.4.1.1 Determination of Vertical Stress (S_v) from Density Measurements

The vertical stress can be characterized by the pressure exerted on a formation at a given depth due to the total weight of the rocks and fluids above that depth (Aird, 2019). The vertical stress and overburden gradient at the top of the upper confining, injection, and lower confining zones were estimated from log data at the offset [redacted] These were calculated by integrating bulk density from surface to the formation depth in half-foot intervals. The average bulk density of the upper confining and injection zones was estimated from the same log. [redacted] Tables 1-4 and 1-5 show the overburden gradient and vertical stress (both in pounds per square inch (psi)) and average bulk densities (in grams per cubic centimeter (g/cm^3)) of the upper confining, injection, and lower confining zones for the two injection well locations.

Table 1-4 – Calculated Vertical Stresses for Cronos No. 1

Formation	Depth (ft)	Avg Bulk Density (g/cm^3)	Avg Bulk Density (lb/ft^3)	Vertical Stress (psi)	Overburden Gradient (psi/ft)
Amph B	[redacted]				
Lower Miocene					
Siph Dav					

Table 1-5 – Calculated Vertical Stresses for Rhea No. 1

Formation	Depth (ft)	Avg Bulk Density (g/cm^3)	Avg Bulk Density (lb/ft^3)	Vertical Stress (psi)	Overburden Gradient (psi/ft)
Amph B	[redacted]				
Lower Miocene					
Siph Dav					

1.4.2 Elastic Moduli and Fracture Gradient

Elastic moduli, including inputs for Eaton's equation, will be determined from laboratory analysis of core samples and log data where applicable. Core samples and log data for this project location are not available at this time and will be recovered during the drilling of the stratigraphic test well(s); the results of mechanical tests will be included in future permit updates. The core samples will undergo triaxial compressive strength testing to provide the geomechanical properties listed in Tables 1-6 and 1-7.

Table 1-6 – Triaxial Compressive Strength Test Results for Cronos No. 1

Sample Number	Depth (ft)	Zone	Formation	Confining Pressure (psi)	Compressive Strength (psi)	Young's Modulus (10^6 psi)	Poisson's Ratio
N/A[(a)]	N/A[(a)]	Upper Confining	Amph B	N/A[(a)]	N/A[(a)]	N/A[(a)]	N/A[(a)]
N/A[(a)]	N/A[(a)]	Injection	Lower Miocene	N/A[(a)]	N/A[(a)]	N/A[(a)]	N/A[(a)]
N/A[(a)]	N/A[(a)]	Lower Confining	Siph Dav	N/A[(a)]	N/A[(a)]	N/A[(a)]	N/A[(a)]

(a) Results are pending the retrieval and lab testing of cores, which will occur when the stratigraphic test well(s) are drilled.

Table 1-7 – Triaxial Compressive Strength Test Results for Rhea No. 1

Sample Number	Depth (ft)	Zone	Formation	Confining Pressure (psi)	Compressive Strength (psi)	Young's Modulus (10^6 psi)	Poisson's Ratio
N/A[(a)]	N/A[(a)]	Upper Confining	Amph B	N/A[(a)]	N/A[(a)]	N/A[(a)]	N/A[(a)]
N/A[(a)]	N/A[(a)]	Injection	Lower Miocene	N/A[(a)]	N/A[(a)]	N/A[(a)]	N/A[(a)]
N/A[(a)]	N/A[(a)]	Lower Confining	Siph Dav	N/A[(a)]	N/A[(a)]	N/A[(a)]	N/A[(a)]

(a) Results are pending the retrieval and lab testing of cores, which will occur when the stratigraphic test well(s) are drilled.

1.4.2.1 Fracture Gradient Calculations

The fracture pressure gradient was estimated using Eaton's equation, a method created for Gulf Coast sands to determine the fracture pressure of the rock. Eaton's equation is commonly accepted as the standard practice for the estimation of fracture gradients (Eaton, 1969). The calculation requires Poisson's ratio (v), overburden gradient (OBG), and pore gradient (PG) to determine the required pressure to fracture the injection zone. These variables can be changed to match the site-specific injection zone. The inputs and resulting fracture pressure gradients for the two proposed injection wells are shown in Tables 1-8 and 1-9 (page 49) for the upper and lower confining zones and injection zone, respectively.

The inputs for Eaton's equation were defined through a review of log data, available literature, and industry standards. The overburden gradients calculated from log data for each zone as was listed in Tables 1-4 and 1-5 (page 43) were utilized. Pore pressure for each zone was estimated from log data at [redacted] A total dissolved solids (TDS) curve was prepared using resistivity data. The TDS values were used to calculate fluid density and pore pressure in half-foot intervals. The resulting pore pressure vs. depth curve is provided in Figure 1-28. This pore pressure result should be considered an adequate representation of pore pressures encountered within the injection and confining zones within the region.

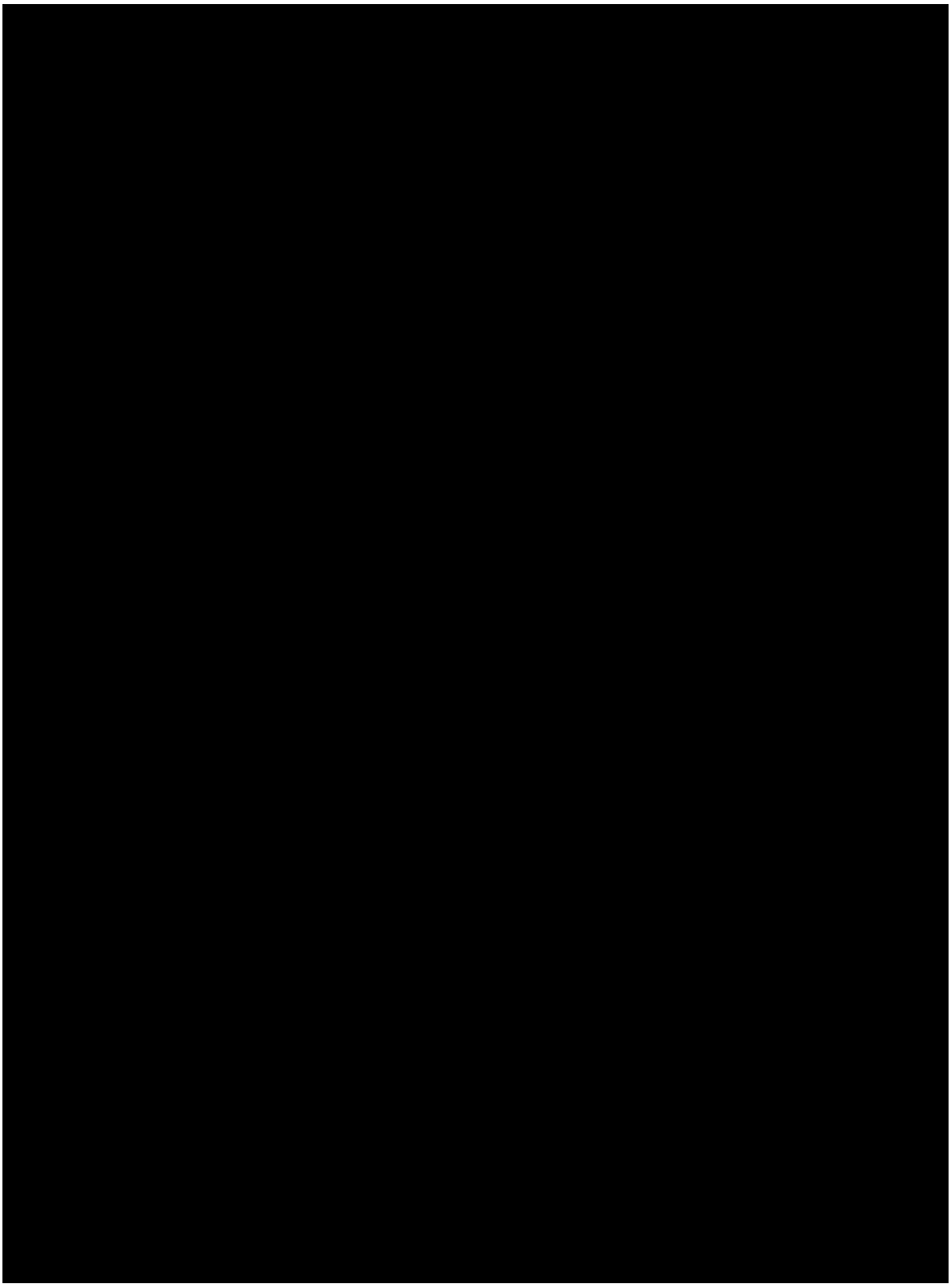

Figure 1-28 – Plot of pore pressure gradient vs. depth calculated from log data at the offset well [redacted]

The Poisson's ratio for the injection zone [redacted]. This well location is shown relative to the Titan Project location in Figure 1-29. The core was retrieved from the Lower Miocene and provided the best available estimate for the Poisson's ratio of the injection zone at the project location. The Poisson's ratio for the upper and lower confining zones was estimated based on a review of published literature. The confining zones consist of clay-rich shales overlying and underlying the injection zone. These shales have a typical range of a Poisson's ratio of 0.28–0.43 (Molina, Vilarrasa, and Zeidouni, 2016). A [redacted]

Figure 1-29 – Map depicting [redacted] core data in relation to the proposed Titan injection wells.

Using these values in Equation 1, a fracture gradient of [redacted] psi/ft was calculated for the injection zone at both injection locations. This gradient was selected to calculate the maximum allowable bottomhole pressure, because it is slightly lower than the fracture gradients of the upper and lower confining zones. A 10% safety factor, as required in 16 TAC 29-N-6 **§5.206(d)(2)(C)** [40 CFR **§146.88(a)**], was then applied to this number—resulting in a maximum allowable bottomhole pressure of [redacted] psi/ft. This safety factor was applied to ensure that the injection pressure would never exceed the fracture pressure of the injection zone.

(Eq. 1)

$$FG = \frac{\nu}{1-\nu}(OBG - PG) + PG$$

[redacted]

Table 1-8 – Fracture Gradients Calculated for Cronos No. 1

Depth (ft)	Zone	Member	Overburden Stress (psi/ft)	Pore Pressure (psi/ft)	Poisson's Ratio	Fracture Gradient (psi/ft)
[redacted]						

Table 1-9 – Fracture Gradients Calculated for Rhea No. 1

Depth (ft)	Zone	Member	Overburden Stress (psi/ft)	Pore Pressure (psi/ft)	Poisson's Ratio	Fracture Gradient (psi/ft)
[redacted]						

1.4.3 Geopressure

As indicated by the pore pressure gradient in Tables 1-8 and 1-9, pressures expected to be encountered within the injection zone will not reflect a geopressured reservoir. Figure 1-30 illustrates a contour map showing the depth of the first occurrence of a pressure gradient of 0.6 psi/ft. According to the map published by the USGS, a pore pressure gradient of 0.6 psi/ft should be anticipated at approximately [redacted] ft. This gradient corroborates with offset well log analysis identifying geopressure characteristics from openhole logs within the [redacted] as shown in Figure 1-31 (page 52).

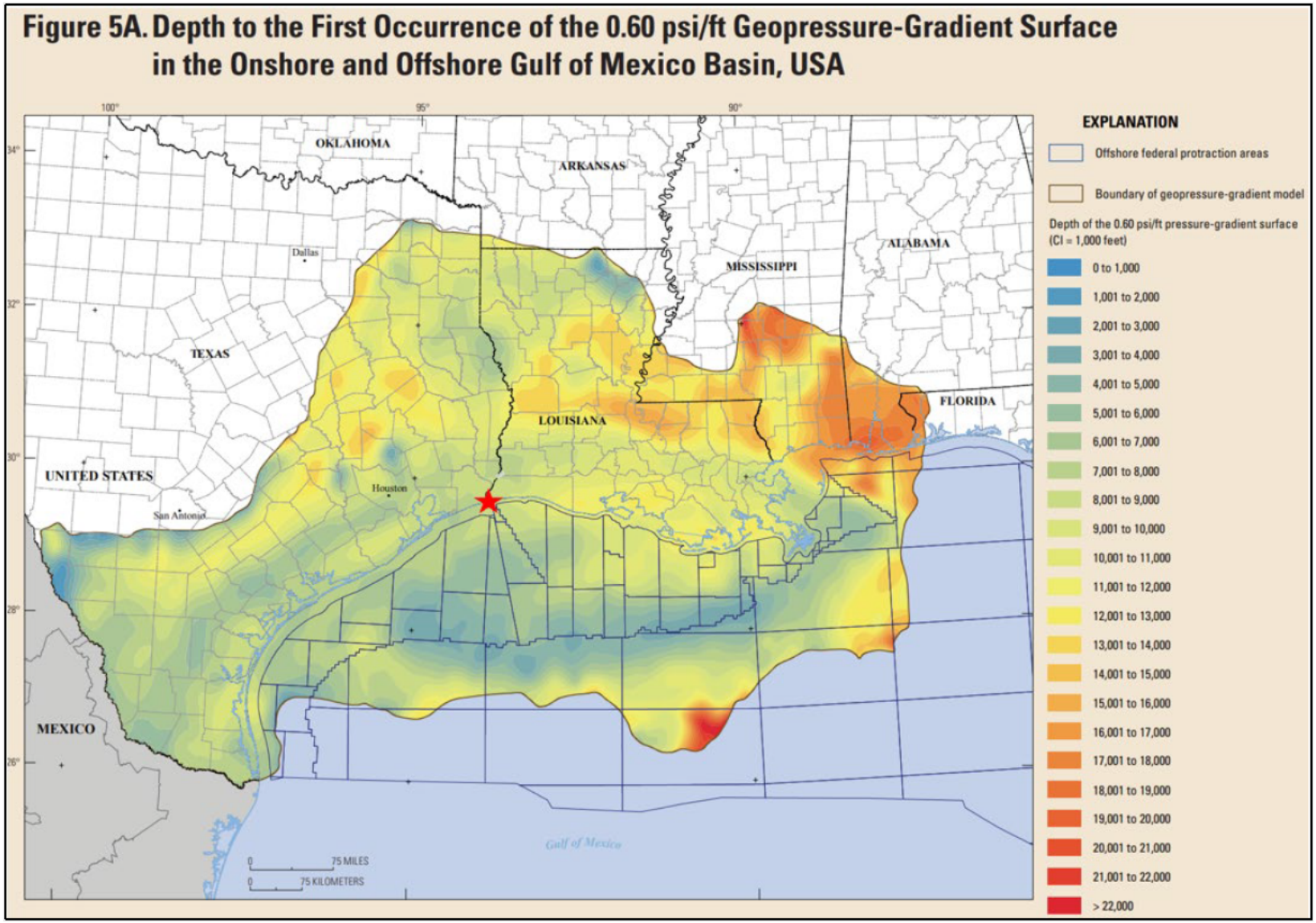

Figure 1-30 – USGS contour map of the first occurence of 0.6 psi/ft pressure gradient (Burke, Kinney, Dubiel, & Pitman, 2013).

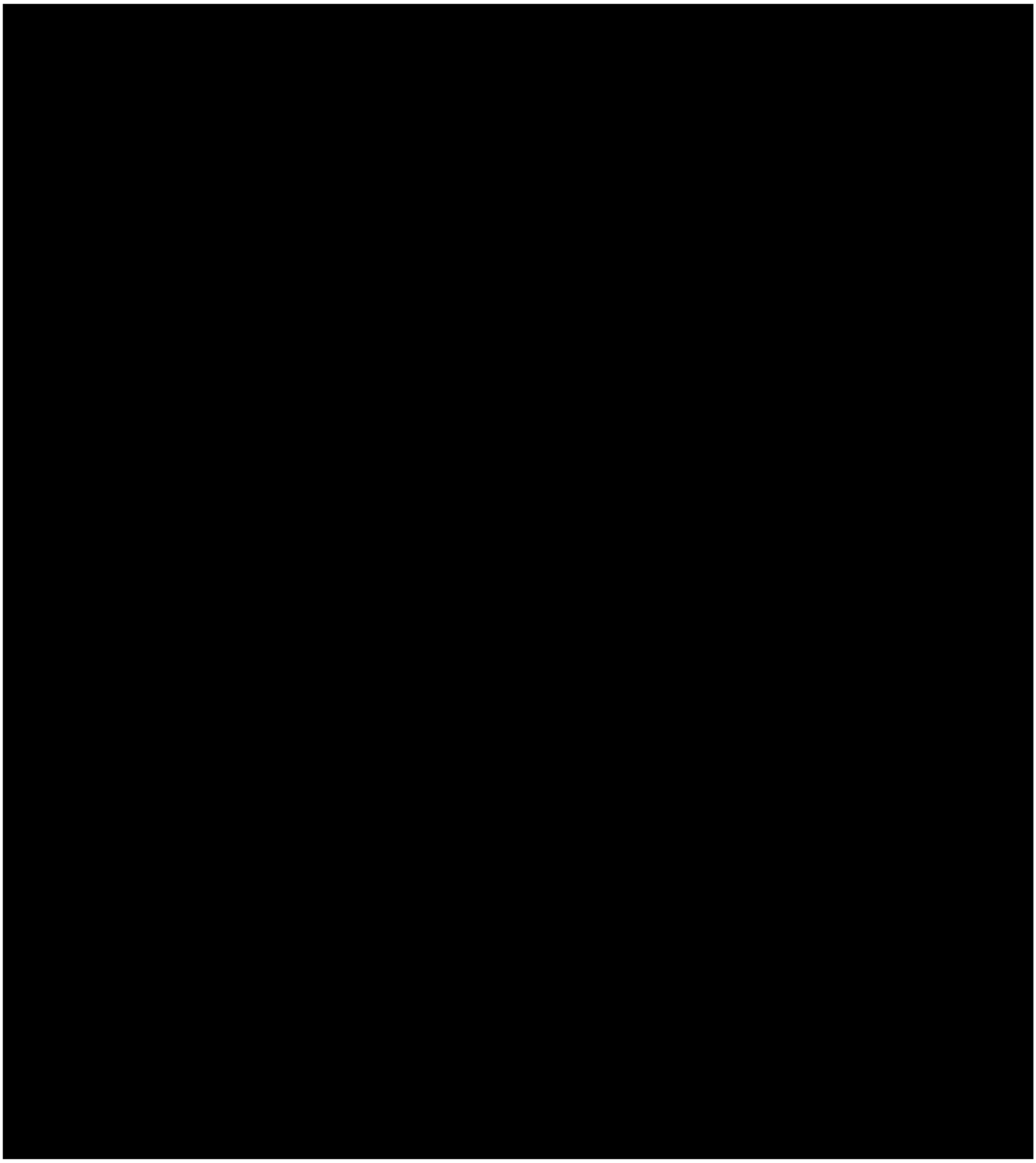

Figure 1-31 – Openhole log of [redacted]

1.5. Porosity and Permeability

The distributions of porosity and permeability within the Lower Miocene at the Titan Project locations are significantly influenced by both deposition and post-burial events. Deposition of sands and silts sourced from the Calcasieu delta system created an environment characterized by interbedded sands and shales. In line with the findings discussed in *Section 1.3.1*, XRD analysis has shown elevated concentrations of quartz with minimal calcite cementation, prohibiting permeability and porosity destruction through calcite cementation, and creating ideal conditions for porosity and permeability development within the injection sands. As a result, it is expected that the injection sands within this interval will remain unconsolidated and exhibit higher vertical-to-horizontal permeability ratios.

These ratios are closely linked to effective porosity, largely influenced by the presence of clays and shales within the injection zone, which serve as barriers. Based on literature, Gulf Coast unconsolidated sandstone formations can exhibit Kv/Kh ratios up to 0.9 (Hovorka et al., 2003). Within the dynamic model, the selection of [redacted] for the Kv/Kh ratio represents a standard upscaled value when extrapolating to the larger model grid block scale for high vertical permeability intervals (Weber and van Geuns, 1990). (This approach is discussed in more detail in *Section 2.5.2.1*, on porosity/permeability.) Common porosity trends within Gulf Coast sands show slightly decreasing porosities with depth but, overall, still have good porosity for injection. This trend is due to compaction defined as decreased intergranular pore space resulting from greater mechanical compaction. This trend is graphically depicted in Figure 1-31 illustrating the decline in porosity with depth. Data retained from the coring and logging operations within the stratigraphic test well and injection wells will be implemented into the current interpretations to enhance accuracy.

Porosity and permeability estimates for both the reservoir and confining zones were determined by conducting a petrophysical analysis using offset openhole logs and core data. During the drilling of the stratigraphic test well and injection wells, supplemental physical data on porosity, permeability, capillary entry pressure, and other reservoir characteristics will be acquired and analyzed. This information will enhance understanding and modeling of the containment and injectability aspects of the reservoir at the proposed injection site. The nearest well to the proposed storage site that provided density/neutron porosity log data for the intended injection zone corresponds to the [redacted] The following procedure was applied to this specific well to establish a correlation between lithology-indication logs and effective porosity. Effective porosity serves as a measure of the interconnected or intergranular void space within a rock, which offers a more accurate representation of the available pore space for fluid mobility as compared to total porosity. Total porosity encompasses intragranular pore space, which may not be directly linked to the overall pore network.

Quality assurance (QA) was conducted to verify the use of accurate data for subsequent calculations. An evaluation was carried out to compare digital or LAS log data with a corresponding raster log. Digital curves were adjusted as needed to maintain consistency with the original raster log data, as illustrated in Figure 1-32. Furthermore, a trend line was

established to interpret the variation of SP with depth, and during this analysis, baseline shifts in SP were detected, as depicted in Figure 1-33.

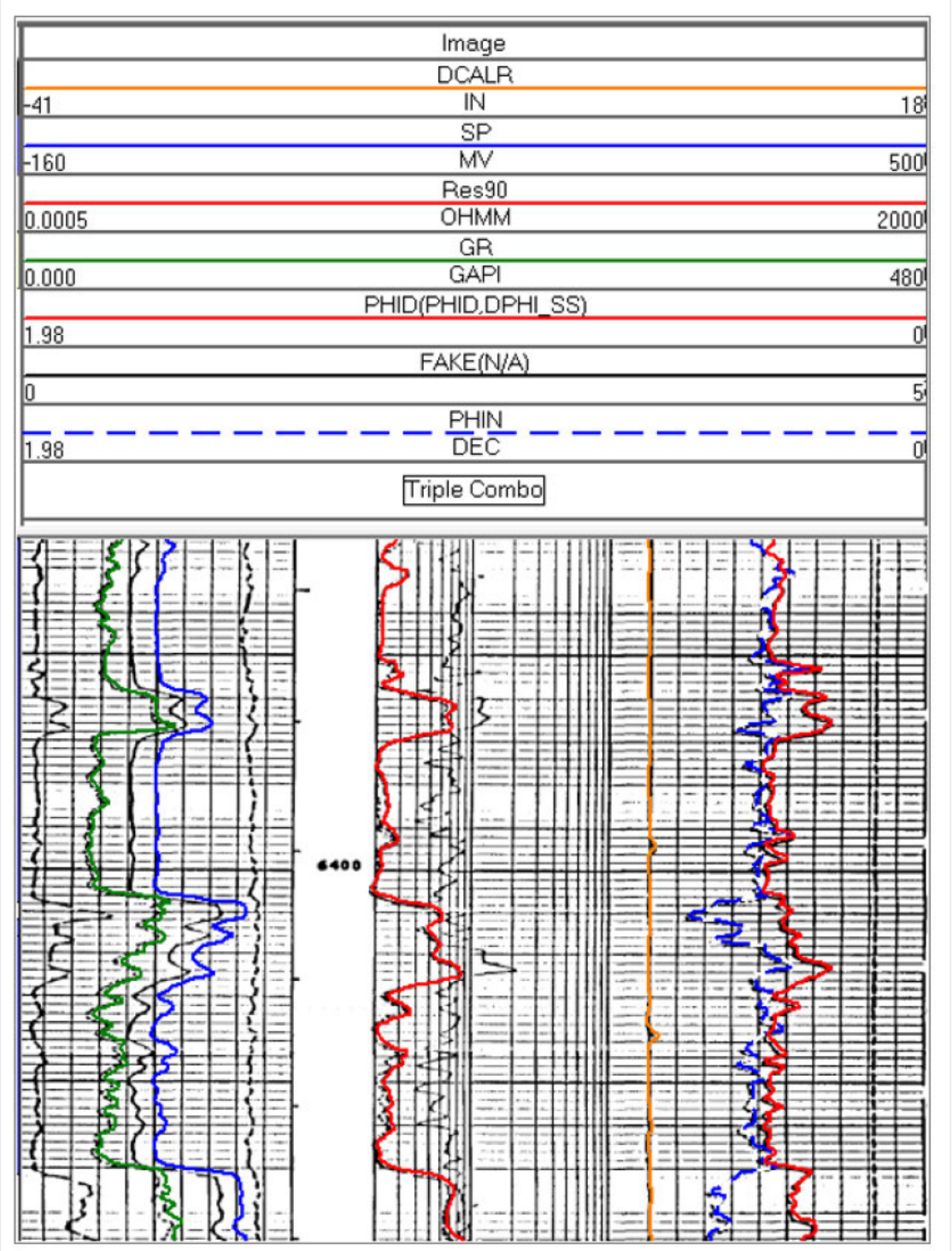

Figure 1-32 – Log depicting example QA process to ensure digital data resembles raster data.

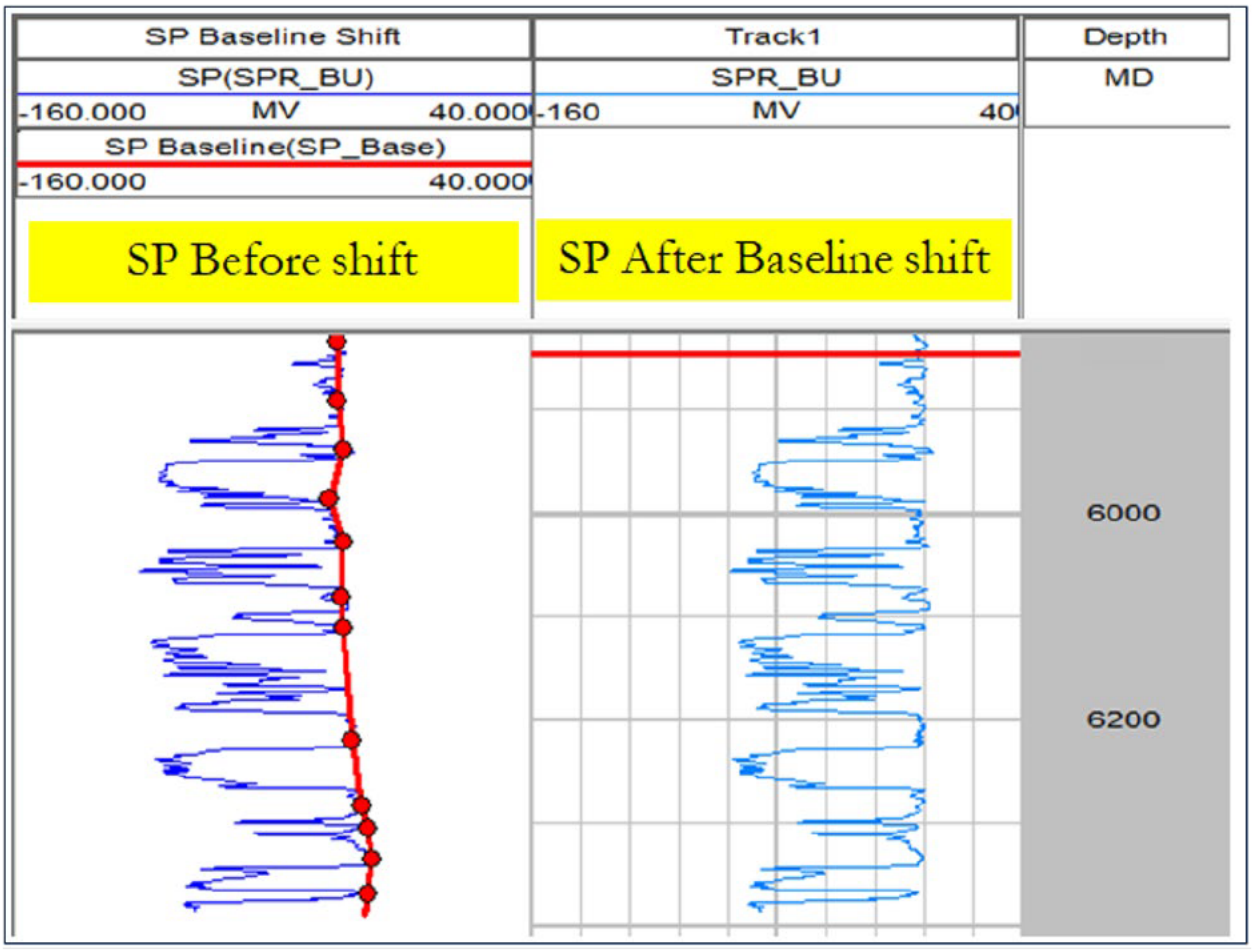

Figure 1-33 – Example of SP Baseline Shift Over Depth

After the spontaneous potential curves were corrected, Vshale was computed from the SP logs, using Equation 2.

(Eq. 2) $$Vshale = \frac{(SP - SPsand)}{(SPshale - SPsand)}$$

Where:
SP = spontaneous potential
$SPsand$ = spontaneous potential reading of a sand
$SPshale$ = spontaneous potential reading of a shale

Estimated effective porosity (PHIEST, Φ_{eff}) was calculated using the Vshale log and PHIMEAN, using Equation 3.

(Eq. 3) $$\emptyset_{eff} = \emptyset_{mean} * (1 - Vshale)$$

Where:
$\emptyset_{eff}$ = effective porosity
$\emptyset_{mean}$ = mean porosity

The PHIEST curve was compared to the PHIE derived from actual density porosity logs for validation. Figure 1-34 illustrates the strong correlation between the computed and measured curves. The PHIEST curve was then used in adjacent wells with SP log data to generate the most accurate estimates of effective porosities within the Miocene intervals.

Since Φ_{eff} reflects the degree of interconnected pore space, a correlation can be established between porosity and permeability. Sidewall core reports were obtained and analyzed from an offset operator for [redacted], located approximately [redacted] of the Titan Project. Table 1-10 lists the core points along with their corresponding reservoir values. A correlation was established between porosity and the corresponding permeabilities based on the core data presented in Figure 1-35 (page 59). These cores were collected from diverse lithologic intervals, offering a comprehensive representation of the likely permeability ranges encountered within the injection and confining zones. This variability is shown in Figure 1-36 through an openhole log with the core points depicted. The gamma ray (GR) and SP curves in Track 1 aid in identifying the lithology of the cored interval. Higher GR and SP readings (lines trending to the right side of the track) indicate shale, while the opposite trend suggests sand. As indicated in the image, the cores were taken within the *Marg Asc* maximum flooding surface and sand deposit that followed thereafter. This variability enabled the development of a single equation to represent a reliable relationship between porosity and permeability. Equation 4 was used to determine permeability as follows:

(Eq. 4) $$K(mD) = $$ [redacted]

These equations were applied to [redacted] offset wells near the proposed injection site and used to develop porosity and permeability distributions within the model. Figure 1-37 shows the location of the offset wells utilized for the porosity and permeability evaluation.

Figure 1-34 – Comparison between calculated effective porosity (PHIE) and estimated effective porosity (PHIEST), from the [redacted]

Table 1-10 – Core Data Values, [redacted]

Depth (ft)	Permeability (md)	Porosity	Oil Saturation	Water Saturation
[redacted]				

Figure 1-35 – Porosity vs. Permeability Scatterplot of Sidewall Core from [redacted]

Figure 1-36 – Openhole log display of [redacted] depicting the variabiliy of the core points within the section.

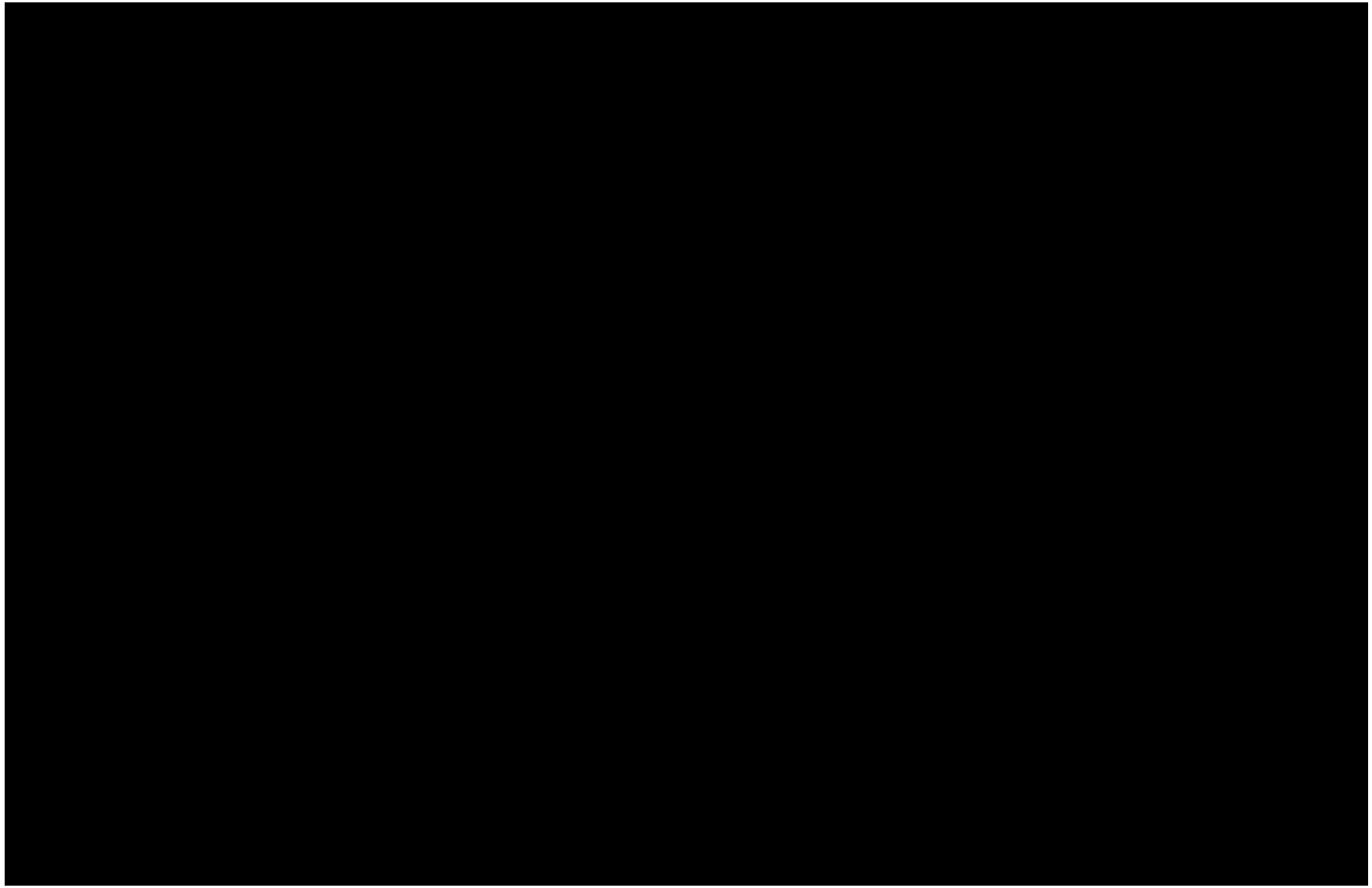

Figure 1-37 – Porosity Modeling Wells

1.5.1 Upper Confining Zone

The Amph B maximum flooding surface contains high clay content due to the depositional features described in *Section 1.3.2*. Figure 1-38 is an openhole log image of the [redacted], with PHIE representing effective porosity and K_Core representing permeability. As displayed in the openhole log, the Amph B contains thin sand members with little porosity and permeability development within the center of the formation. These sands will not impact the sealing capabilities of the clays above and below them. The clay-rich shales in the Amph B contain isolated pores that cannot create effective pore networks, rendering them "sufficient" for CO_2 sequestration (Meckel & Trevino, 2014). Distributions of the porosity and permeabilities within the geocellular model that reflect these shale facies are depicted in Figures 1-39 and 1-40 (pages 64 and 65, respectively).

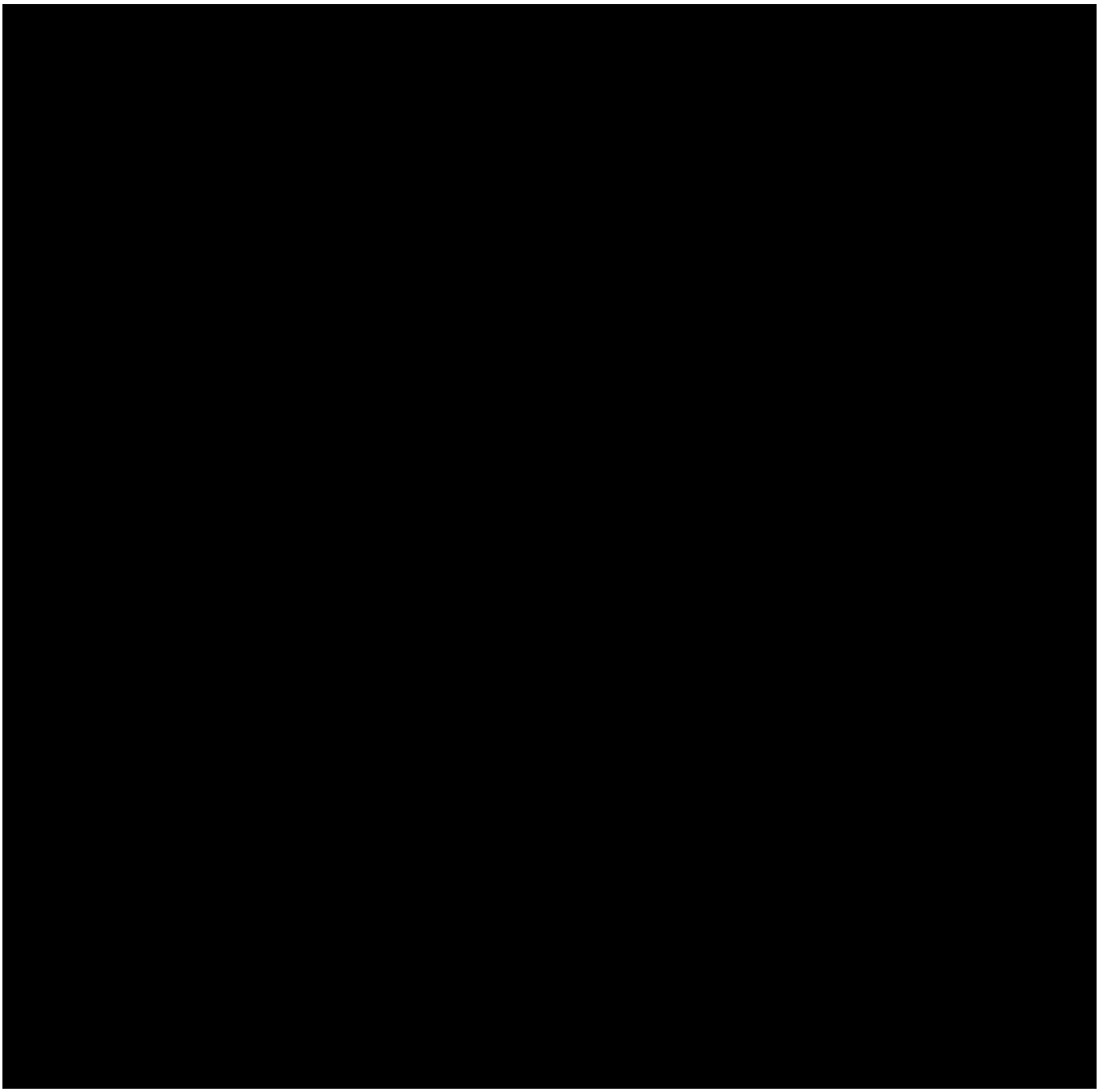

Figure 1-38 – Openhole log of offset well [redacted] depicting the upper confining zone. Effective porosity is displayed in green and permeability in red.

1.5.1.1 Upper Confining Zone Porosity

Within the shale facies in the upper confining zone, the average effective porosity is [redacted] Figure 1-39 presents the histogram displaying these distributions. With such an ample amount of net low-porosity facies within the upper confining zone, transmissibility through this confining unit is unlikely.

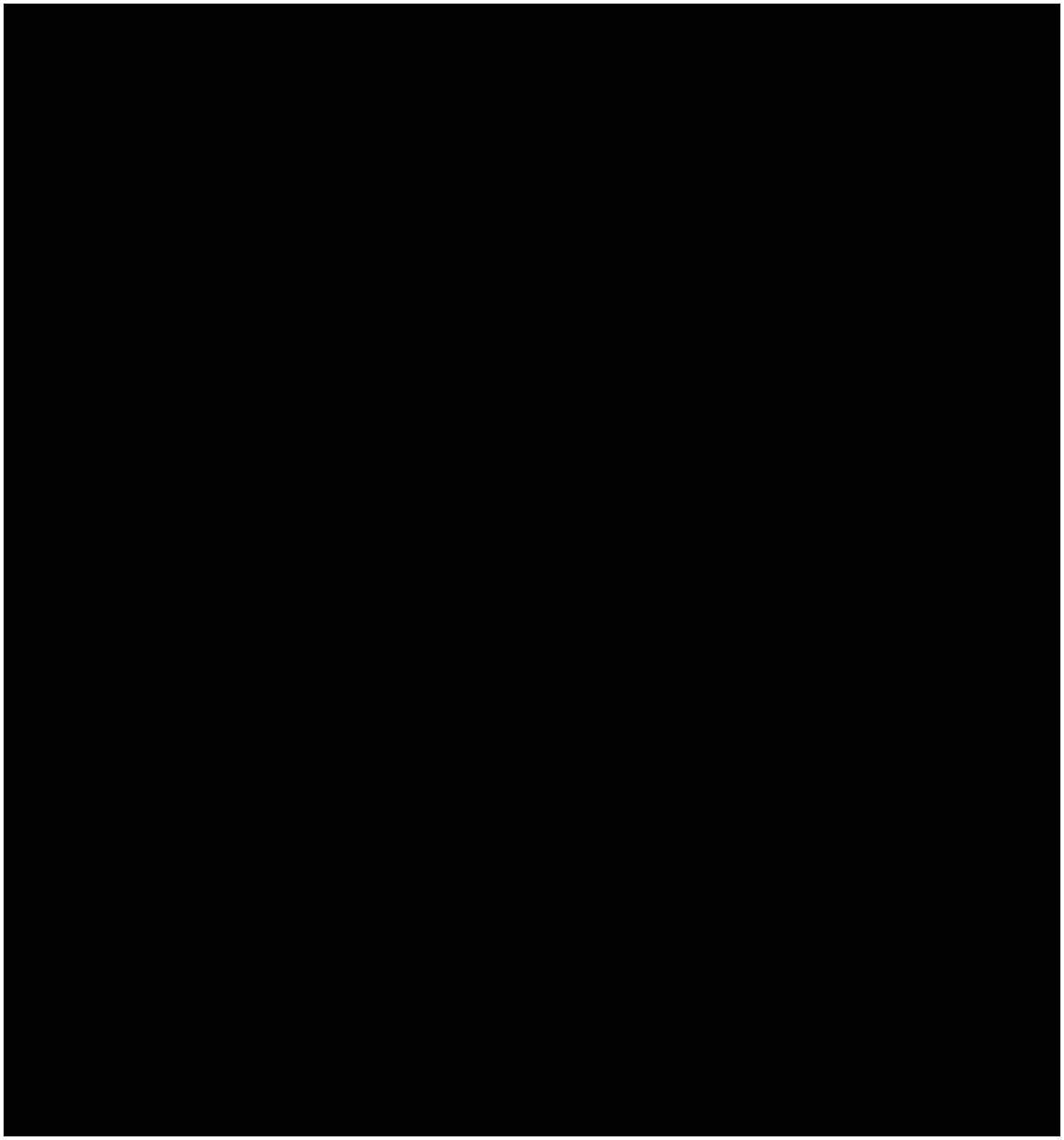

Figure 1-39 – Histogram of Porosity Distributions Within the Upper Confining Zone

1.5.1.2 Upper Confining Zone Permeability

Within the shale facies in the upper confining zone, the average horizontal permeability is [redacted] mD. Figure 1-40 presents the histogram displaying these distributions. Because of the very low horizontal and vertical permeabilities, transmissibility through this confining unit is unlikely.

Figure 1-40 – Histogram of Permeability Distributions Within the Upper Confining Zone

1.5.2 Injection Zone

The proposed Titan Project site will target the Lower Miocene formations as its injection zone. The distribution of permeability and porosity within this interval is notably influenced by the absence of calcite cementation and the prevalence of quartz, as evidenced in the core analysis detailed in *Section 1.3.1*. Figure 1-41 displays an openhole log of the [redacted] where PHIE represents effective porosity and K_Core represents permeability.

Within this injection zone, the target compartments for injection are the deltaic/shallow marine sands characterized by higher effective porosities and permeabilities. These sands are separated by interbedded shales that serve as compartmental seals. Figure 1-40 illustrates these injection compartments, with the sand intervals displaying noticeably higher porosity and permeability compared to the shale intervals. The subsequent sections provide descriptions of porosity and permeability distributions within the sand facies determined in the model.

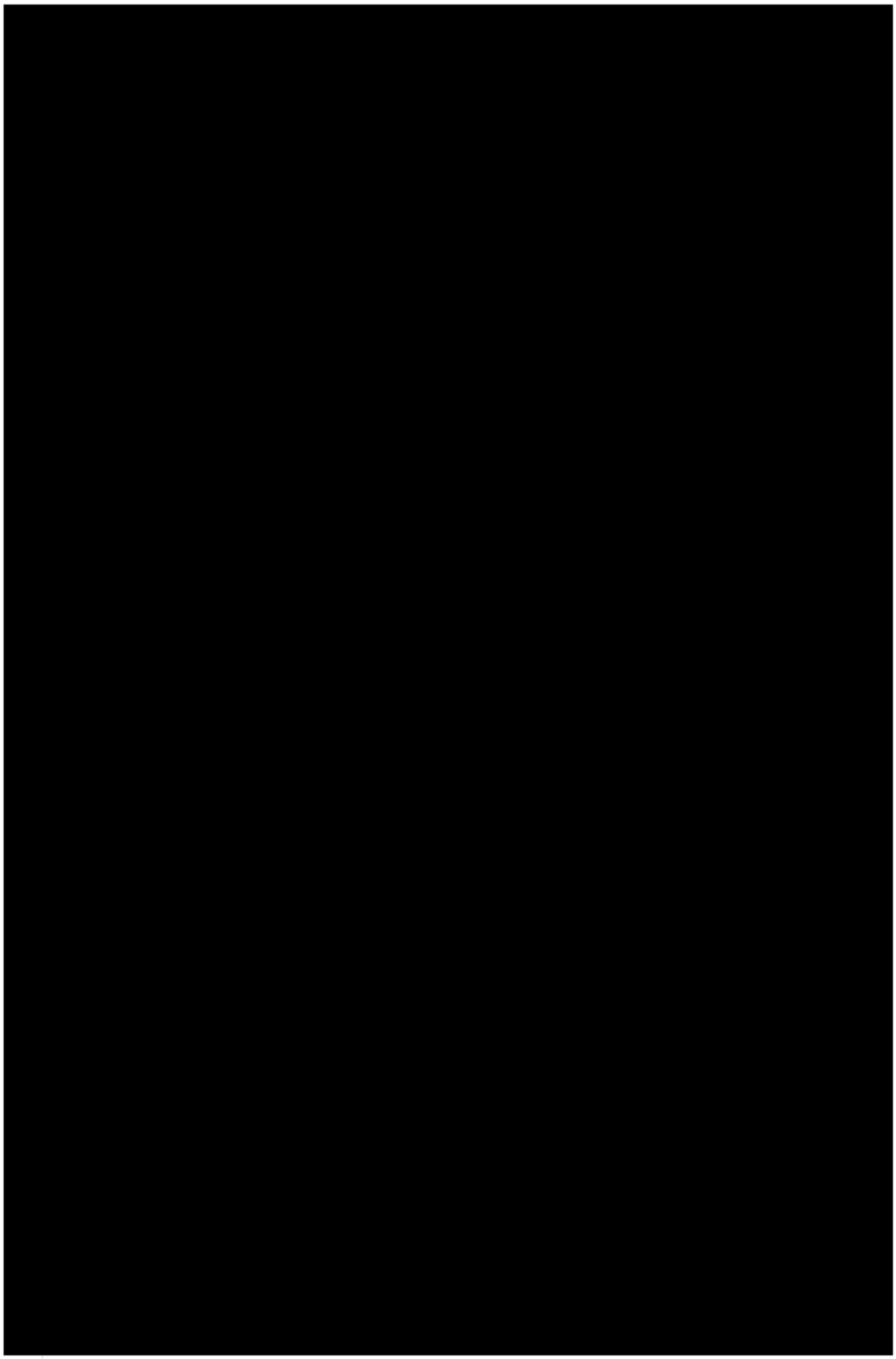

Figure 1-41 – Openhole log of [redacted] depicting the injection zone. Effective porosity is displayed in green and permeability in red.

1.5.2.1 Injection Zone Porosity

In the sand facies of the injection zone, the average effective porosity is [redacted] Figure 1-42 provides the histogram that illustrates these porosity distributions within the geocellular model. As mentioned in Section 1.5, porosity trends within the Miocene sands exhibit a decrease with depth, primarily due to compaction, which is evident in Figure 1-42. An isopach map, displaying porosity values [redacted] has been generated for the injection zone and is included in *Appendix B-12*. That map shows approximately [redacted] ft of net sand with porosities exceeding 12% at the proposed location.

Figure 1-42 – Histogram of Porosity Distributions Within the Injection Zone

1.5.2.2 Injection Zone Permeability

In the sand facies of the injection zone, the average permeability is [redacted] mD. Figure 1-43 provides histograms illustrating these permeability distributions within the geocellular model. Notably, because permeability is closely linked to porosity, the same trends observed in porosity distributions apply to permeability.

The vertical-to-horizontal (Kv/Kh) permeability ratios are expected to increase with higher porosity and permeability values due to the lack of cementation, which would drive unconsolidated sands within the injection zone.

Figure 1-43 – Histogram of Permeability Distributions Within the Injection Zone

1.5.3 Lower Confining Zone

The Siph Dav represents a widespread regional maximum flooding surface from the early Lower Miocene era. This flooding surface led to the deposition of a regional layer consisting of clay and mudstone. Offset core analysis from High Island revealed the prevalence of high calcite concentrations, which functioned as cements. This presence of calcite cementation is anticipated to significantly diminish the porosity and permeability of the samples, as highlighted by Meckel and Trevino (2014). (Additional information regarding the depositional environment was provided in *Section 1.3.3*.) Figure 1-44 is an openhole log image of [redacted] with PHIE representing effective porosity and K_Core representing permeability. As evident from the log, there is minimal-to-no sand formation within the Siph Dav, making it an excellent choice as a consistently thick and extensive lateral seal. The distributions of these predominantly shale facies within the Siph Dav in the geocellular model are presented in Figure 1-44.

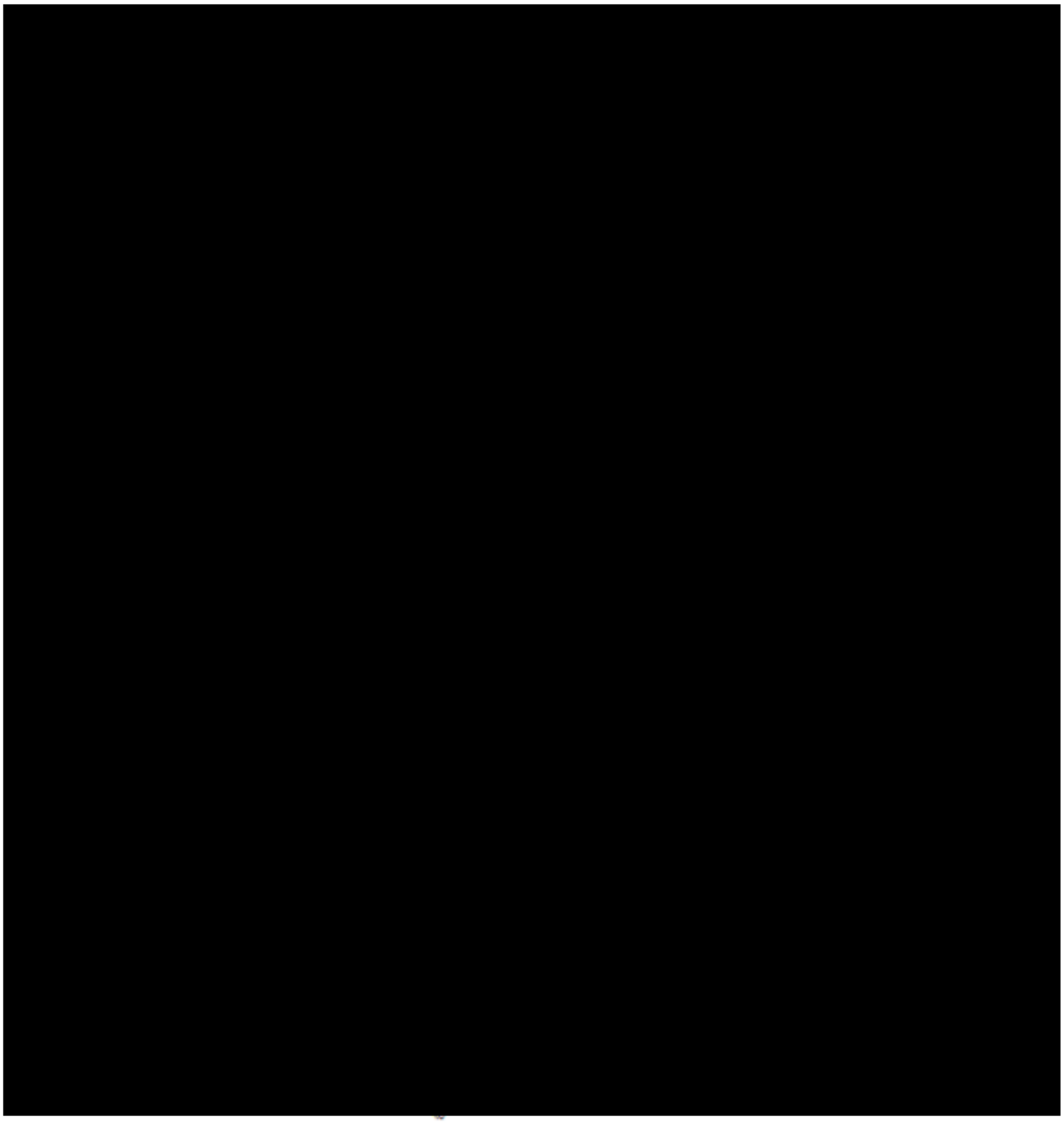

Figure 1-44 – Openhole log of [redacted] depicting the lower confining zone. Effective porosity is displayed in green and permeability in red.

1.5.3.1 Lower Confining Zone Porosity

Within the shale facies in the lower confining zone, the average effective porosity is [redacted]. Figure 1-45 presents the histogram displaying these distributions within the geocelluar model.

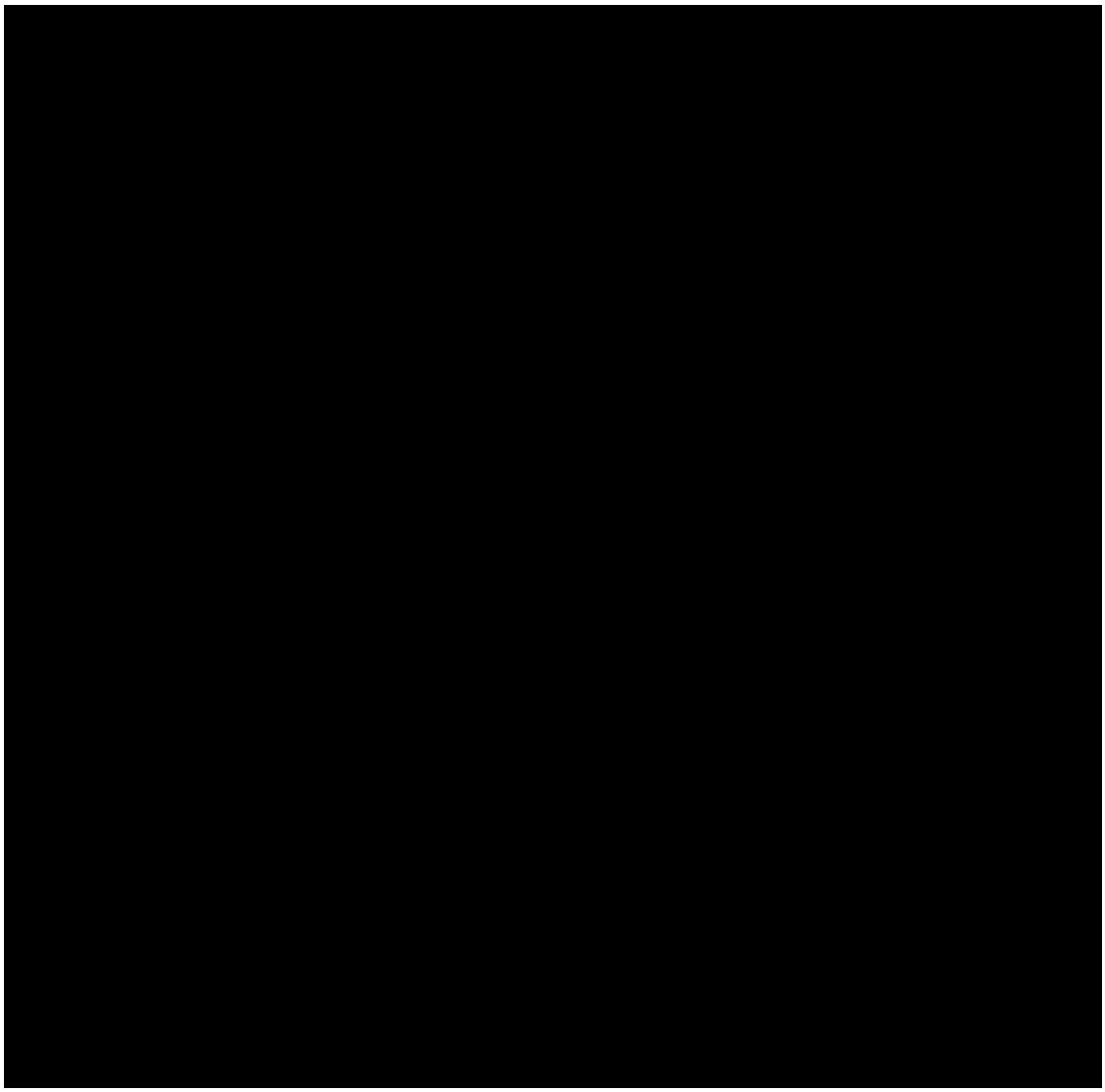

Figure 1-45 – Histogram of Porosity Distributions Within the Lower Confining Zone

1.5.3.2 Lower Confining Zone Permeability

Within the shale facies in the lower confining zone, the average permeability is [redacted] mD. Figure 1-46 presents the histograms displaying these distributions within the geocelluar model. These findings indicate an ideal lower confining zone that will effectively serve as a lower seal for the proposed injection site.

Figure 1-46 – Histogram of Permeability Distributions Within the Lower Confining Zone

1.6. Injection Zone Water Chemistry

1.6.1 Injection Zone Water Chemistry

To help determine the water chemistry within the injection zone, publicly available data from the USGS National Produced Waters Geochemical Database was accessed along with openhole log analysis. The database was filtered to fluid samples from Miocene sands, in a geographic window ranging from [redacted] This data was tabulated and plotted to examine the relationship between TDS and depth. Figure 1-47 depicts this relationship, with the red dashed lines representing the approximate depths of the injection zone. As seen in the graph, the majority of the Miocene samples occur[redacted] mark. A breakdown of the average chemical makeup of the sampled water samples is provided in Table 1-11.

Figure 1-47 – Depth vs. TDS graph of collected water samples from the USGS. The red dashed lines indicate the approximate injection zone.

Table 1-11 – Formation Brine Chemstry

Species	Concentration	Units
TDS		mg/L
Sp. Grav		g/cm^3
Ca		mg/L
Fe		mg/L
Mg		mg/L
Mn		mg/L
K		mg/L
Na		mg/L
SiO_2		mg/L
Cl		mg/L
HCO_3		mg/L
SO_4		mg/L

Furthermore, a thorough analysis of openhole logging was conducted for the [redacted]. This involved determining the apparent water resistivity (Rwa) by utilizing deep resistivity and porosity logs. Equation 5 provides an illustrative example of this calculation.

(Eq. 5) $$Rwa = Deep\ Resistivity * Porosity^2$$

Following the calculation of Rwa, the Schlumberger General 9 chart equation (as illustrated in Figure 1-48) was used to transform Rwa into TDS. Figure 1-49 presents the results of this calculation, demonstrating an average TDS value of roughly [redacted] milligrams per liter (mg/L) within clean sands (Vshale < 10%). Additionally, the log analysis showcases an example of an Rwa value at [redacted], which is depicted on the Schlumberger General 9 chart, indicating an estimated salinity of [redacted] TDS under those specific conditions. With that TDS value being a single data point within the log, the average of [redacted] mg/L was selected as the best fit to use in the plume modeling. There is a notable level of uncertainty when estimating the composition of the connate fluid. This will be verified with physical samples from the formations when drilled and cored.

[redacted] Water samples from the injection zone will be collected during the drilling operations of the proposed injection wells. Comprehensive water analyses will be conducted to establish the baseline reservoir fluid conditions. Once this data set is acquired, the models will be revised accordingly.

Additional data from water samples and analysis from the drilling process of the stratigraphic test well and injection wells will, once collected, be utilized in the model.

Figure 1-48 – Schlumberger General 9 chart with red lines representing [redacted]

Figure 1-49 – Example of log analysis performed on [redacted] to estimate TDS.

1.7. Geochemistry

The mineral-brine-CO_2 interactions that occur during CO_2 sequestration lead to the alteration of the host rock, and eventual equilibrium in the mineral-brine-CO_2 system. Chemical modeling and laboratory experiments show that these reactions and eventual equilibria are driven by the specific mineralogy of the target formation, composition of the brine, acidity of the CO_2-brine mixture, and pressure and temperature in the subsurface. This section covers the modeling of the mineral-brine-CO_2 system across the mineralogical facies associations present for the subject site.

1.7.1 Methods

Simplified, batch kinetic simulations (i.e., models) were created for each facies present at the subject location. The models are built to simulate the reactions that occur in the mineral-brine-CO_2 system contained inside a laboratory reactor vessel as a proxy for the subsurface system. The models use phase thermodynamic data in the PHREEQC Lawrence Livermore National Laboratory Database and reaction kinetics from Palandri and Kharaka (2004) to model the mineral-brine-CO_2 interactions. Each experiment is isothermal, with the temperature set to match the subject location and depth. The pressure for each simulation is also static and set to match the subject location and depth. The thermodynamic model is based on local equilibrium for the minerals and ions in an aqueous phase. The kinetic calculations assume that abundant CO_2 is supplied to the system during the simulation and that any consumed molecule of CO_2 is replaced. These simplifying assumptions align with the reality of the physical system, in that continuous injection allows for an abundant gas supply to the system.

1.7.2 Brine Geochemistry

The brine composition used for the simulations comes from the USGS National Produced Waters Geochemical Database. The database contained 37 samples of produced water from the Miocene-age sandstones in the [redacted] oil and gas fields located in Jefferson County, Texas. The average brine composition derived from the USGS database was then adjusted to match the log derived average salinity of [redacted] mg/L. The adjusted analytical value is then used in each mineral batch kinetics model (Table 1-12).

Table 1-12 – Brine composition used in the PHREEQC reaction-path modeling.

Species	Concentration	Units	
TDS	[redacted]	mg/L	
Sp. Grav		g/cm^3	
Ca		mg/L	
Fe		mg/L	

Species	Concentration	Units	
Mg	[redacted]	mg/L	
Mn		mg/L	
K		mg/L	
Na		mg/L	
SiO_2		mg/L	
Cl		mg/L	
HCO_3		mg/L	
SO_4		mg/L	

1.7.3 Mineral Geochemistry

Despite the well understood nature of the stratigraphy in the vicinity of the subject site, published XRD data from core are limited. The mineral compositions used in simulations were generated by averaging 18 sample values from the High Island 24L No. 9 (42-708-30316) into two average values, one for confining zones (shales) and the other for injection zones (sands) (Meckel and Trevino, 2008). The averaged values are in line with other published lithologic descriptions and generalized XRD data along the Gulf Coast published by Hovorka et al. (2003), Loucks et al. (1977), Meckel and Trevino (2014), and McGuire (2009), as well as XRD analyses of silicate rocks from similar depositional environments published in Weaver (1977).

Mineral compositions used in the models are shown in Table 1-13. [redacted]

Table 1-13 – Mineral Compositions Used in the Four-Facies Model

Facies Name	Upper Confining Zone	Top Injection Zone	Base Injection Zone	Lower Confining Zone
Modeled Depth (ft)	[redacted]			
Stratigraphic Interval				
Quartz				
Calcite				
Plag (albite)				
K-spar				
Illite				
Kaolinite				

1.7.4 Models

A total of four geochemical models were created: one each for the upper and lower confining zones and two for the injection zone. [redacted]

The reaction processes expected were modeled as a product of thermodynamic equilibrium and kinetic reactions using PHREEQC. The models were created as simplified, 1D batch models that occur at pressure and temperatures dictated by their stratigraphic position. The models assume a pressure gradient of [redacted] psi/ft and a thermal gradient of [redacted] with a mean annual surface temperature of 70°F. The injected volume of CO_2 was assumed to fill the pore spaces.

1.7.5 Results

Across each of the models, the results displayed in Figures 1-50 and 1-51 show that [redacted]

During the injection period, the modeled changes of the injection zone mineralogy are relatively minor. [redacted]

A number of necessary assumptions used in this modeling work leads to the models overrepresenting the speed and amount of alteration, compared to what will occur in the natural system. [redacted], geologic and hydrologic factors such as fluid flow paths may alter ion availability and system reactivity.

Figure 1-50 – Results of all constituents for the batch models for each facies. The x-axis is "log10" time in years. The reaction time spans from 0.001 seconds to 10,000 years.

Figure 1-51 – The results of minor constituents for the batch models for each facies. The x-axis is log10 time in years. The reaction time spans from 0.001 seconds to 10,000 years.

1.8. Fault Seal Analysis

The fault seal analysis is conducted to evaluate the sealing capacity of the faults. Within the CCS scope, two scenarios are considered: (1) when the plume reaches a surface-reaching fault; and (2) when only the pressure front reaches a fault. Therefore, only the second scenario—of the pressure front potentially reaching the faults—needs to be addressed.

Figure 1-52 – A 3D image of CO_2 plume (at stabilization) relative to nearby faults, viewed (a) from the northeast and (b) from the top.

To estimate fault sealing capacity, the shale gouge ratio (SGR), fault zone entry capillary pressure (FZP), and fault zone permeability were calculated. The SGR is an important parameter used to estimate the amount of clay within the fault gouge, as the very fine phyllosilicates result in very small pore throats, leading to high FZP and low permeabilities within the fault zone (Yielding, 2002). The accuracy of the SGR estimations certainly depends on the quality of input data, but overall the SGR "has proven to be a robust and quantitative predictor of fault seal in mixed clastic sequences" (Yielding, 2002). The SGR and SGR equation (Yielding et al., 1997) is a widely accepted method used to estimate the amount of clay within the fault gouge, as shown in Figure 1-53. These equations provide calculations for a sequence of reservoir zones where Δz is the thickness of each reservoir zone, and Vcl is the clay volume fraction in the zone (Yielding et al., 1997).

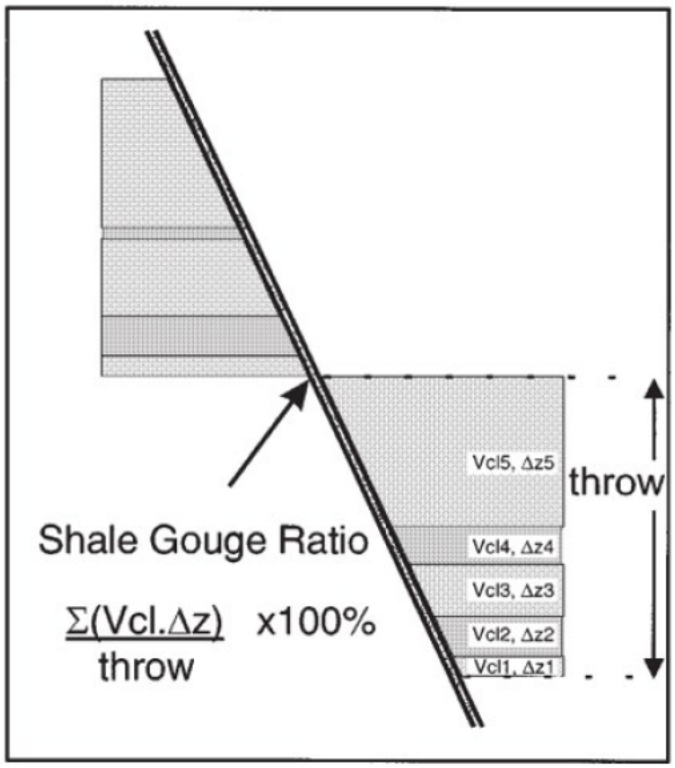

$$SGR = \frac{\Sigma\left[\left(\text{Zone thickness}\right)\times\left(\text{Zone clay fraction}\right)\right]}{\text{Fault throw}} \times 100\%$$

Figure 1-53 – Shale Gouge Ratio Conceptual Diagram and Equation (Yielding et al., 1997)

The SGR has been shown to be an effective qualitative predictor for sealing vs. non-sealing faults in hydrocarbon systems. The SGR data from the fault-bounded reservoirs of both sealing and non-sealing faults show that SGR values of approximately 15% to 20% are the typical cutoff for sealing vs. non-sealing faults (e.g., Bretan et al., 2003; Meckel and Trevino, 2014). Therefore,

anything with an SGR value greater than 20% is deemed to be sealant in nature. The SGR values were calculated from the Vshale, derived from available GR or SP logs. These values were conditioned to facies using the sequential Gaussian simulation algorithm while distributed through 3D volume. Figure 1-54 shows the 3D view of the fault planes with SGR values. Figure 1-55 shows histograms of SGR distribution for the confining and injection zones. Generally, it can be concluded that the [redacted]

Figure 1-54 – A 3D display of the shale gouge ratio on the fault planes (calculated for each cell within the faults for confining and injection zones).

Figure 1-55 – Histograms of the SGR distribution for the (a) upper confining, (b) injection, and (c) lower confining zones.

[redacted]

[redacted]

Figure 1-56 – The 3D model layer slices show facies distribution and fault SGR for the (a) upper confining and (b) injection zones. The maximum extent of the injection plumes is shown as a pink outline. The cross-section shown in Figure 1-57 is shown here as a black dashed line.

Figure 1-57 – A 3D model cross-section showing (a) SGR and Vsh distribution, and (b) SGR and facies distribution. The cross-section location was shown as a black dashed line on Figure 1-56.

To identify if the capillary entry pressure of the fault gouge was reached from the influence of the injected CO_2, FZP calculations were then performed. This effect is applicable only for the faults or their parts if the CO_2 plume reaches those faults. The classic SGR equation for hydrocarbon systems (Bretan et al., 2003) to calculate the FZP using SGR and fault rock strength is:

(Eq. 6) $$FZP\ or\ P_C\ (bar) = 10^{\left(\frac{SGR}{27} - C\right)}$$

Where C is fault rock strength, which varies with depth.

The C values are as follows: C = 0.5 for burials depths less than 9,850 ft; C = 0.25 for burial depths between 9,850 ft and 11,500 ft; C = 0 where burial depths exceed 11,500 ft (Bretan, 2003). However, since the wetting properties of various rock-forming minerals are different for CO_2 and hydrocarbons, this equation needs modification. The most recent work to address this difference was done by Karolyte et al. (2020). As noted by Bretan et al. (2022), proposed modifications lead to FZP reduction of about one-third of the classic FZP results. Therefore, the correction multiplier of 0.667 was applied to the resulting FZP value plus a unit conversion from bar to psi. Figure 1-58 shows calculated threshold FZP values vs. SGR. The FZP threshold increases with SGR increase. If FZP values remain below the threshold line (or a seal-failure envelope at the corresponding SGR), the fault behaves as a seal. If pressure exceeds this threshold at some parts of the fault during the injection, then the fault will lose its sealing properties at those portions.

Figure 1-59 shows the distribution of the FZP values on the fault plane.

Figure 1-58 – Fault Zone Entry Capillary Pressure (FZP) vs. Shale Gouge Ratio (SGR)

Figure 1-59 – Distribution of the FZP Values on the Fault Planes

Another useful estimation based on the SGR calculations is fault permeability (Figures 1-60 and 1-61). Different empirical equations have been proposed and used for permeability estimation. In most cases, as with this project, the input parameters are insufficient for the precise calculations, but the global equation of Jolley et al. (2007), which has been applied here, may provide some general insights on the fault permeability:

(Eq. 7) $$k_f = 4 \times 10^{-5} \times SGR^{-3.47}$$

Where:
k_f = fault permeability, mD
SGR = shale gouge ratio, %

Figure 1-60 – Fault Zones Permeability vs. SGR

Figure 1-61 – Distribution of the fault zone predicted permeability values on the fault planes.

Figure 1-62 shows histograms of permeability distribution for the confining and injection zones. These histograms show that the planes of the fault zones are mostly characterized by low permeabilities. For example, per corresponding histograms, abou

Figure 1-62 – Histograms of the fault permeability distribution for the (a) upper confining, (b) injection, and (c) lower confining zones.

The SGR-based analysis provides useful information about fault properties and estimates of their sealing capacities. Additionally, this analysis includes a permeable-impermeable rocks juxtaposition captured in the geostatic model and typically accounted for at the dynamic modeling stage. Three parameters provided by the fault seal analysis are SGR, FZP, and fault permeability at the present/static conditions. These calculated parameters indicate that, [redacted] These parameters define the fault behavior under present conditions and, along with FZP, set thresholds for the fault behavior under changing dynamic conditions.

[redacted]

[redacted]

1.9. Hydrology

Located in the southeastern area of Texas, Jefferson County encompasses an area of more than 1,100 sq mi. The cities of Beaumont and Port Arthur are the two primary population centers in the county, nearly a quarter of which is covered in water. This section discusses water resources and hydrology within the county. The USGS and other entities have written detailed reports, dissertations, and literature from peer-reviewed journals within this area of study.

1.9.1 Area of Study

Groundwater resources are nearly nonexistent in the area except for the Chicot aquifer. The Chicot is the shallowest aquifer of the major Gulf Coast aquifers and only provides fresh or treatable water at shallow depths along the Jefferson County coastline. The Titan Project area falls within this region of limited groundwater resources as shown in Figure 1-63.

Surface water resources include Sabine Lake, also known as the Sabine Estuary, and numerous smaller lakes. The Neches River and basin are also present and contain many tributaries and bayous that also provide inflow to the river.

Figure 1-63 – Image of Gulf Coast Aquifer in Texas with the red star representing the proposed injection site (Brunn, Jackson, Peter, & Walker, 2016).

1.9.2 Groundwater Resources

1.9.2.1 Major Aquifer – Gulf Coast Aquifer

The Gulf Coast aquifer is located along the entirety of the coastline from western Louisiana to northern Mexico and is comprised of multiple aquifers, to include the Jasper, Evangeline, and Chicot. A confining unit known as the Burkeville is found between the Evangeline and Jasper aquifers.

A regional cross section depicting those four different sedimentary units is displayed in Figure 1-64. More than 50 Texas counties are supplied with fresh water from this regional resource. The primary uses of the aquifer are for municipal, industrial, and irrigation districts. The Houston area is provided with a yield of approximately 1,600 gallons per minute (gpm). The quality of the water differs from region to region but tends to be better in the northeastern section, which includes Jefferson County. Total dissolved solids are nominally no higher than 500 mg/L, but saltwater intrusions have been noted in the area. The thickness of the aquifer can be as much as 1,300 ft, with the average freshwater thickness nearing 1,000 ft.

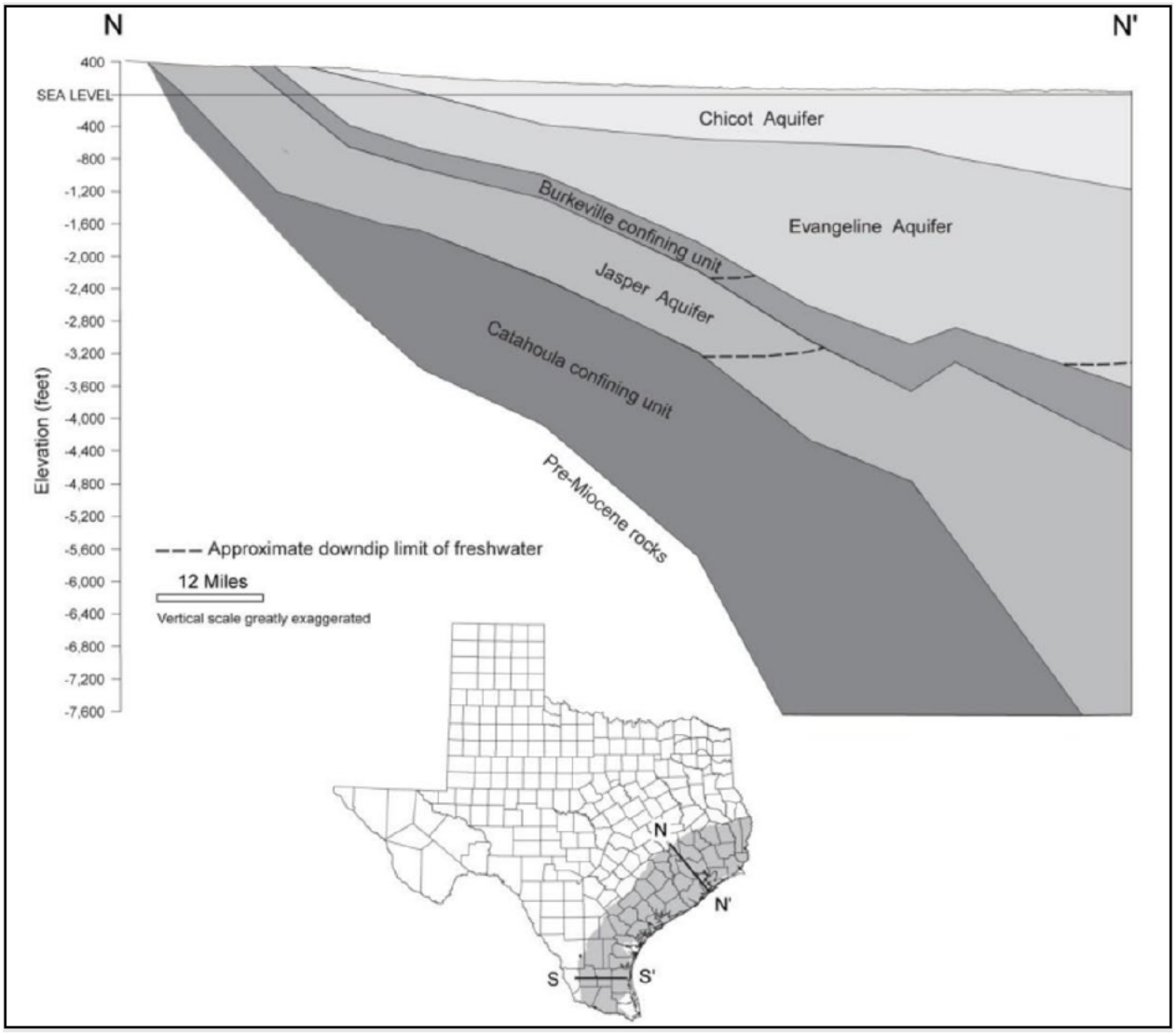

Figure 1-64 – Regional Cross Section of the Gulf Coast Aquifer in Texas (Brunn, Jackson, Peter, & Walker, 2016)

1.9.2.2 Chicot Aquifer

The Chicot aquifer is the shallowest underground water source of the major Gulf Coast aquifer system and is made of Quaternary-age sediments. The Chicot, which contains a larger abundance of sand than clay, has a thickness of nearly 1,200 ft at the coastline. Though the aquifer only bears consumable fresh water at very shallow depths, the Chicot is still present. It has been heavily pumped, providing water sources for irrigation, municipal supply, and industrial uses to the northern parts of the target area. The city of Houston has the most built-up development, with large-scale wells capable of yielding thousands of gallons per minute rates. Other cities near the Titan Project have also developed infrastructure to support their residential, commercial, and agricultural communities. Figure 1-65 is a map depicting the outcrop areas of the Jasper,

Evangeline, and Chicot aquifers, along with the Burkeville confining unit. A list of water wells discovered in the area is provided in *Appendix C-4*, with most reaching total depths no greater than 20 ft. One well (6317504) tested water from a depth of 119 ft but is listed as "plugged or destroyed" and is no longer producing water from these depths.

Figure 1-65 – Gulf Coast outcroppings of the Jasper, Evangeline, and Chicot aquifers in Jefferson County, with the red star representing the injection site (Kasmarek, 2004).

1.9.3 Surface Water Resources

1.9.3.1 Neches River

The Neches River flows from north to south through Jefferson County into the Sabine Lake, next to the city of Port Arthur, Texas. The last 40 mi of the river are considered industrialized. Kept at a deep draft so that deepwater vessels can navigate it, the river is approximately 40 ft deep and 400 ft wide—and planned to be deepened by another 8 feet. The Lower Neches Valley Authority provides most of the fresh water to Port Arthur and its surrounding areas. The valley authority also oversees the Neches River in multiple counties to include Jefferson County. "Freshwater inflow contributions to the Sabine-Neches estuary consist of (1) gauged inflow from the Sabine and Neches River Basins; (2) ungauged runoff; (3) return flows from municipal, industrial, and agricultural sources in ungauged areas; and (4) direct precipitation on the estuary" (Texas Department of Water Resources, 1981). Once near the coastline, the river becomes more saline until it empties into the primarily saltwater Sabine Lake or Sabine Estuary.

1.9.3.2 Sabine Lake

Sabine Lake covers approximately 90,000 acres and is considered a saltwater estuary and bay. The lake borders both Texas and Louisiana with Port Arthur situated next to it. The lake was created by the joining of two separate rivers—the Sabine and the Neches—which provide most of the fresh water, around 85%, in the lake. Near the area are several smaller lakes, such as Johnson Lake and Keith Lake to the north, and Salt Lake to the west of the target area.

1.9.4 Hydrology Conclusion

[redacted]n, as illustrated in Figure 1-66. [redacted] The water wells in this area are generally shallow, with most having depths of less than 50 ft—except for well [redacted] Consequently, an estimated depth for the USDWs, in alignment with the estimated USDW depths provided by the BEG, is approximately [redacted] ft, to safeguard all water sources located at or near the surface.

Figure 1-66 – Map of water-level changes within the Gulf Coast aquifer, depicting the injection site (indicated by the red star) falling within the "Unconfined (outcrop)" area (Brunn, Jackson, Peter, & Walker, 2016).

1.10. Evaluation of Mineral Resources

1.10.1 Active Mines Near the Proposed Injection Location

A public data search determined that no active surface mines are near the proposed site of the Titan Project; therefore, no surface mineral impacts will occur from project activities.

1.10.2 Oil and Gas Resources

Exploration activity in far southeast Texas began in the mid-1950s and 1960s. Much of the drilling activity focused around the salt domes found along the Gulf Coast. These domes, plus additional faulting in the area, created structural traps for hydrocarbons. However, the Titan Project is in an area where fewer hydrocarbons have successfully been recovered, as no structural trap exists across the area. [redacted] Within the AOR, no wells were drilled.

[redacted]

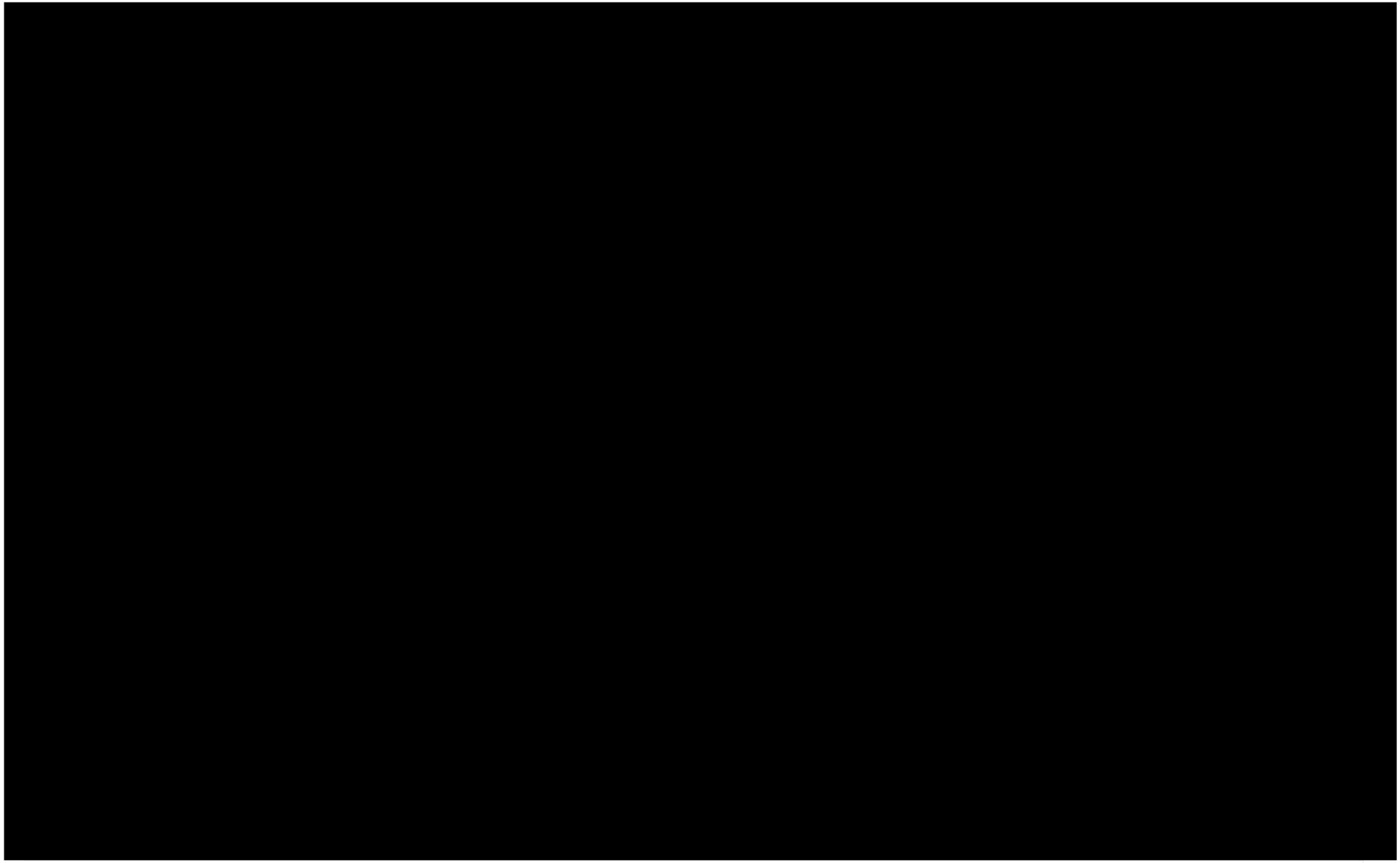

Figure 1-67 – Oil and Gas Wells [redacted] of the Titan Project

Table 1-14 – Productive Oil and Gas Wells Within 6 Miles of Titan Project Site

API No.	Well Name	Field	County/Parish	Well Status	Reservoir(s)	Spud Date	Plugged Date	First Prod Date	Last Prod Date
[redacted]									

API No.	Well Name	Field	County/Parish	Well Status	Reservoir(s)	Spud Date	Plugged Date	First Prod Date	Last Prod Date
[redacted]									

The closest well to the Titan Project, the [redacted] is located just under [redacted] of the project. [redacted]

With the lack of economically viable hydrocarbons in the area, the Titan Project is well suited for the injection and sequestration of CO_2.

1.11. Seismic History

Every new injection well project must consider, during the design and development phase, the potential for seismic activity caused by the injection operations. This part complies with 16 TAC **§5.203 (c)(2)(D)** [40 CFR **§146.82(a)(3)(v)]**, the Class VI rule, by carrying out the following four steps:

1. Identification of historical seismic events in proximity to the project
2. Faulting and determination of operational influences of nearby faults
3. Performance of a fault slip potential (FSP) simulation model
4. Review of seismic hazard

1.11.1 Identification of Historical Seismic Events

Texas experiences seismic activity in six key areas (Figure 1-68): the Delaware Basin and Midland-Odessa area in west Texas, the Panhandle, east Texas, the Eagle Ford area of south Texas, and the Cogdell Field near Snyder (Savvaidis, 2022). The area of interest (AOI) reviewed for this section was defined as a 9.08-km radius[1] around the project wells, based on seismographic recordings from a global network of seismological stations. According to a search of the Texas Seismological Network and Seismology Research (TexNet), [redacted] from the Titan Project site (Figure 1-69, page 103). Additional research into other seismic catalogs, including those from the USGS Earthquake Archive, Volcano Discovery, and Northern California Earthquake Data Center (NCEDC), supported the TexNet findings. Although Texas does have seismic active areas, the proposed project is located in an area where regional stress is low, as no earthquakes have occurred along southeast Texas and the Gulf Coast, demonstrated in Figure 1-70 (page 104). [redacted]

[1] Texas Railroad Commission FSP AOI Standard under the Seismicity Review.

[2] The magnitude of an earthquake is reported using the Richter scale, which measures the amount of energy (i.e., amplitude) generated at the source of an earthquake.

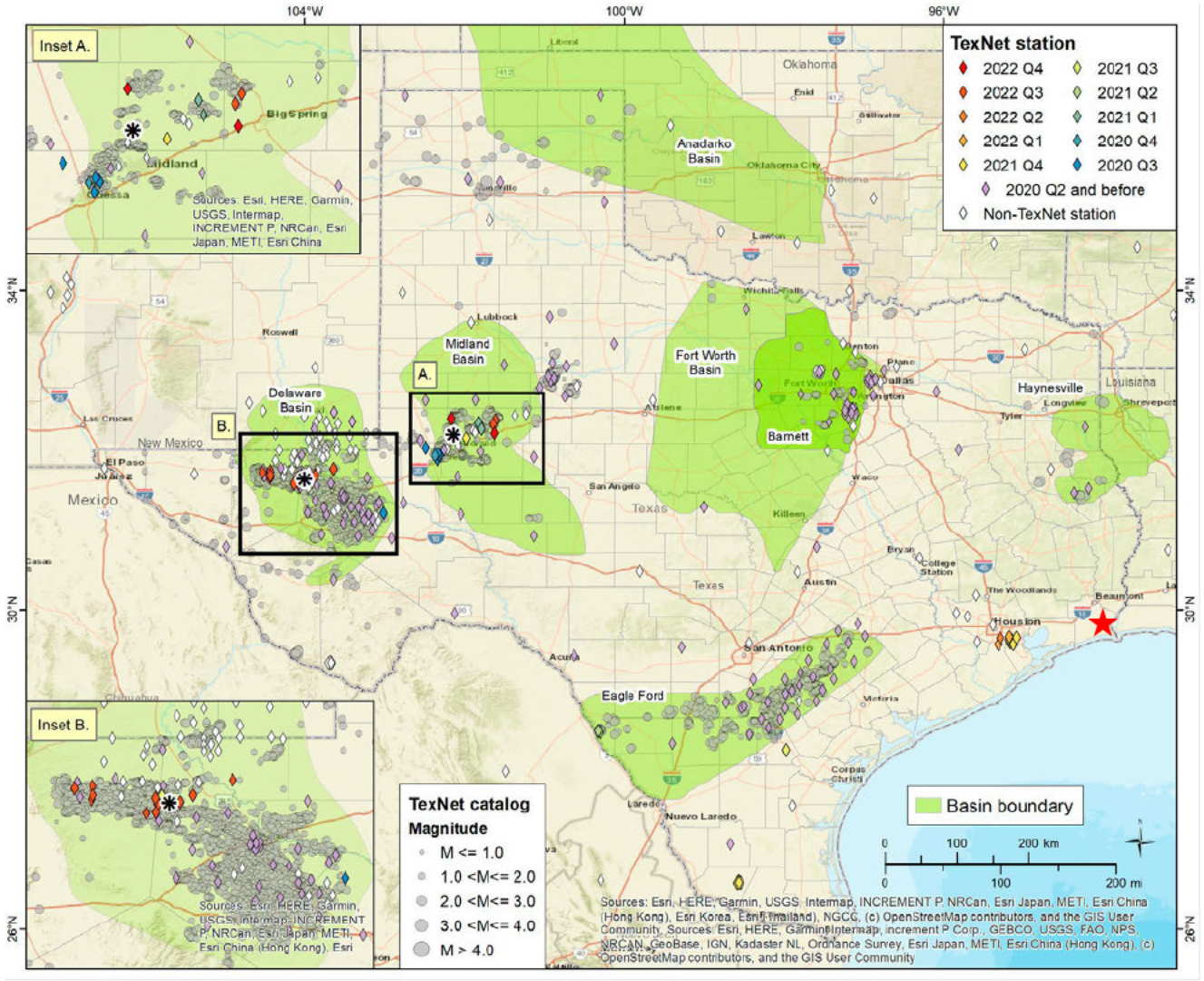

Figure 1-68 – Seismically active areas in Texas, with the red star indicating the proposed project location (Savvaidis, 2022).

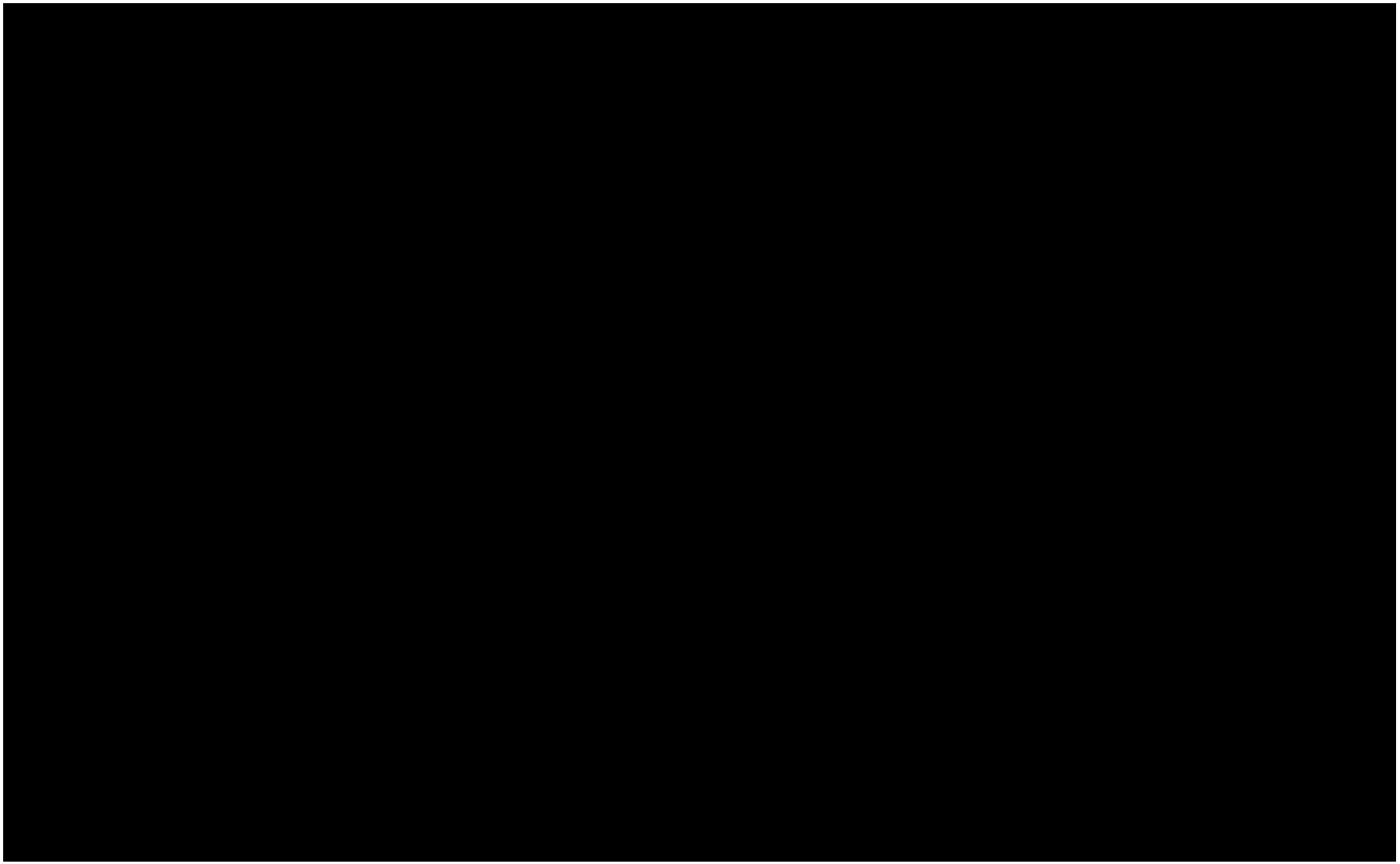

Figure 1-69 – Earthquake Search Parameters and Results from TexNet Website

Figure 1-70 – USGS-registered earthquakes inland east Texas, along the Gulf Coast and west Louisiana.
In red is the location of the proposed project, the green circle is the 9.08-km radius around the project, and the green dot is the closest earthquake.

1.11.2 Faults and Influence

The USGS has created a comprehensive database with respect to faults and associated folds, which includes five classes: A, B, C, D, and E. This database classifies faults in southeast Texas as "Class B," because most of them are in sediments and poorly lithified rocks that cannot withstand the forces necessary for the propagation of massive seismic ruptures that might cause dangerous ground motions. Additionally, Crone and Wheeler (2000) reference the possibility that the post-rift sequence and its band of normal faults along the Gulf of Mexico margin are mechanically separated from the underlying crust, reducing the risk of a significant earthquake[3]. These Cenozoic fault zones (Figure 1-71), from Oligocene- and Miocene-age displacement, showed a regional tendency to strike [redacted] g faults within the higher clay-concentrated layers, including the upper and lower confining zones.

[3] The USGS defines a *significant earthquake* to be greather than 600, a number derived by magnitude, number of "Did You Feel It" responses, and PAGER alert level.

Figure 1-71 – Major Cenozoic fault zones in southeast Texas and the location of the proposed project (indicated by the red star) (Meckel and Trevino, 2014).

1.11.3 Fault Slip Potential Model

The FSP model calculates the cumulative likelihood of a known fault exceeding the Mohr-Coulomb slip criteria due to fluid injection. Accounting for pressure variations at the prospective site is critical to prevent faults from reactivating or the seal from being hydraulically fractured (Meckel and Trevino, 2014). Based on the injection strategy, an FSP model was designed to assess the seismic risk, match the 3D flow simulation in Computer Modelling Group's GEM 2023.20 (GEM) software, and replicate the correct fault transmissivity discovered in the AOI. The results and data, including assumptions and uncertainties, are discussed in *Appendix B-13*.

[redacted] The FSP models reproduced the GEM models using sealing fault properties; however, the injection reservoir is [redacted]

1.11.4 Seismic Hazard

A seismic hazard analysis was carried out for the Titan Project using the EPA-recommended tools found in the USGS 2018 National Seismic Hazard Model (NSHM) Project and derived maps. The 2018 NSHM integrated and updated the 2014 NSHM, including fault models, seismic catalogs, population density, ground motion models, soil amplification factors, amplified shaking estimates of long-period ground motions, and seismic hazard calculation. The 2018 Modified Mercalli Intensity[4] (MMI) earthquake hazard map (Figure 1-72) reveals that, for a hard rock site, there is a 2% chance that peak ground accelerations will be surpassed in 50 years. Furthermore, in that time span according to Figure 1-72, a Class IV[5] or V[6] earthquake is most likely to impact southeast Texas (per the 2018 model). The AOI is in a Class IV hazard area. Figure 1-73 (page 109), which illustrates the likelihood of a minor damaging earthquake occurring over the conterminous United States in 100 years, shows southeast Texas having a 4%–19% chance of experiencing a Class VI[7] earthquake. In terms of 10,000 years, Figure 1-74 (page 110) depicts fewer than two damaging earthquakes[8] to occur in southeast Texas.

Based on the 2018 NSHM, therefore, the Titan Project location is within the lowest seismic hazard areas in United States.

[4] The MMI scale ranges from I to XII. The following summaries were taken from the USGS Earthquake Hazards Program, which were first condensed by Wood and Neumann in 1931.

[5] Class IV: "…light; felt indoors by many, outdoors by few during the day: At night, some are awakened. Dishes, windows, and doors are disturbed; walls make cracking sounds. Sensations are like a heavy truck striking a building. Standing vehicles are rocked noticeably."

[6] Class V: "…moderate; felt by nearly everyone; many awakened: Some dishes and windows are broken. Unstable objects are overturned. Pendulum clocks may stop."

[7] Class VI: "…strong; felt by all, and many are frightened. Some heavy furniture is moved; a few instances of fallen plaster occur. Damage is slight."

[8] *Damaging earthquake*: shaking; meaning a level VI or higher, causing structural failure.

Natural Hazards

In terms of natural hazards[9], Jefferson County, Texas, is considered "Relatively High" based on

Figure 1-72 – Total mean hazard map for 2% probability of exceedance in 50 years and the location of the proposed project (indicated by the red star) (Petersen, et al., 2019, p. 33).

[9] *Natural hazard* includes the following 18 hazards: Avalanche, Coastal Flooding, Cold Wave, Drought, Earthquake, Hail, Heat Wave, Hurricane, Ice Storm, Landslide, Lightning, Riverine Flooding, Strong Wind, Tornado, Tsunami, Volcanic Activity, Wildfire, and Winter Weather.

Figure 1-73 – Risk of a Class VI earthquake shaking in 100 years at the location of the proposed project (indicated by the red star), plus population density (Petersen, et al., 2019, p. 7).

Figure 1-74 – Predicted damaging earthquakes shaking around the United States and the location of the proposed project (indicated by the red star) ("Frequency of Damaging Earthquake Shaking Around the U.S", retrieved 2023).

Figure 1-75 – Jefferson County National Risk Index Map showing community resilience. The red star indicates the location of the proposed project (National Risk Index FEMA, 2023).

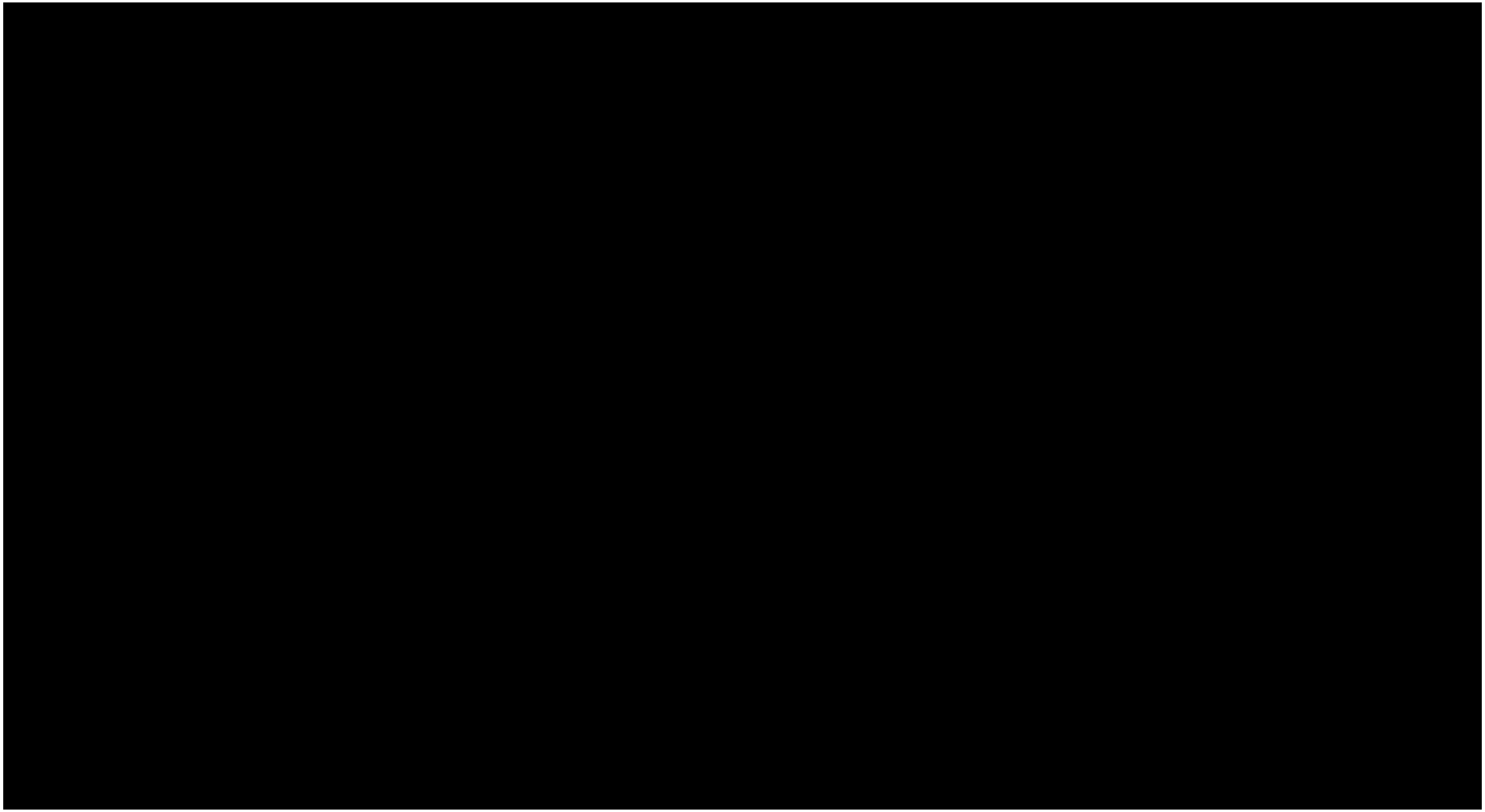

Figure 1-76 – Jefferson County National Risk Index Map showing hazard types. The red star indicates the location of the proposed project (National Risk Index FEMA, 2023).

Figure 1-77 – National Risk Index Scores for Jefferson County

1.12. Site Characterization Conclusion

The evaluation of the proposed injection wells, Cronos No. 1 and Rhea No. 1, demonstrates that the Lower Miocene sandstones possess ample porosity, permeability, lateral continuity, and depth to effectively accommodate the intended volume of CO_2. The Amph B exhibits sufficient thickness and is laterally distributed within the injection area, featuring desirable confining characteristics including high clay content with low effective porosity and permeability. Likewise, the Siph Dav shares similar characteristics with the Amph B, making it a suitable lower confining zone. The assessment of faulting in the area has been thorough, involving evaluation, modeling, and determination of low risk concerning containment within the proposed injection zone. Upon the drilling of the stratigraphic test well, additional data will be gathered and analyzed to ensure that the site maintains a low-risk status for CO_2 injection and storage.

The following attachments are in *Appendix B:*

- Appendix B-1 SW-NE Structural Cross Section
- Appendix B-2 NW-SE Structural Cross Section
- Appendix B-3 SW-NE Stratigraphic Cross Section
- Appendix B-4 NW-SE Stratigraphic Cross Section
- Appendix B-5 Cross Section Reference Map
- Appendix B-6 Top Upper Confining Structure
- Appendix B-7 Top Injection Zone Structure
- Appendix B-8 Top Lower Confining Structure
- Appendix B-9 Upper Confining Isochore
- Appendix B-10 Injection Zone Isochore
- Appendix B-11 Lower Confining Isochore
- Appendix B-12 Injection Zone Net Sand
- Appendix B-13 Fault Slip Potential Model
- Appendix B-14 XSEC_Logs

1.13. References

"Frequency of Damaging Earthquake Shaking Around the U.S." (retrieved 2023). *USGS sources include Earthquake Hazards Program*. https://www.usgs.gov/media/images/frequency-damaging-earthquake-shaking-around-us.

Aird, P. (2019). *Deepwater Geology & Geoscience*. ScienceDirect: https://www.sciencedirect.com/topics/engineering/overburden-stress.

Bretan, P. (2022). Assessing the predictive capability of the empirical Shale Gouge Ratio–buoyancy pressure calibration: implications for estimating CO2 column heights. The Geological Society of London.

Bretan, P. Y. (2003). Using calibrated shale gouge ratio to estimate hydrocarbon column heights. AAPG.

Brunn, B., Jackson, K., Peter, L., and Walker, J. (2016). Texas Aquifers Study. *Groundwater Quantity, Quality, Flow, and Contributions to Surface Water*.

Bump, A. P., Bakhshian, S., Ni, H. et al. (2023). Composite confining systems: Rethinking geolgic seals for permanent CO2 sequestration. *International Journal of Greenhouse Gas Contro* 126. https://doi.org/10.1016/j.ijggc.2023.103908.

Burke, L. A., Kinney, S. A., Dubiel, R., and Pitman, J. K. (2013). Regional Maps of Subsurface Geopressure Gradients of the Onshore and Offshore Gulf of Mexico Basin. USGS.

Crone , A., and Wheeler, R. (2000). *Data for Quaternary faults, liquefaction features, and possible tectonic features in the Central and Eastern United States, east of the Rocky Mountain front.* U.S. Geological Survey.

Eaton, B. A. (1969). Fracture Gradient Prediction and Its Application in Oilfield Operations. SPE-AIME.

Galloway, W. E. et al (2000). Cenozoic Depositional History of the Gulf of Mexico Basin. AAPG.

Galloway, W. E. (2008). *Sedimentary Basins of the World*, Chapter 15: Depositional Evolution of the Gulf of Mexico Sedimentary Basin, 505-549.

Galloway, W. E., Ganey-Curry, P. E., Li, X., and Buffler, R. T. (2000). Cenozoic depositional history of the Gulf of Mexico basin. AAPG.

Heidbach, O., Rajabi, M., Cui, X. (2016). World Stress Map database release 2016: Crustal stress pattern across scales. *Tectnophysics*, 484-498.

Hovorka, S. D., Holtz, M. H., Sakurai, S. et al. (2003). Frio Pilot in CO2 Sequestration in Brine-Bearing Sandstones. Gulf Coast Carbon Center.

Jolley, S., Stuart, G., and Freeman, S. (2007). Progressive evolution of a late-orogenic thrust system, from duplex development to extensional reactivation and disruption: Witwatersrand Basin, South Africa. In: Deformation of the Continental Curst. *Geologic Society*, 543-569.

Karolyte, R., Johnson, G., Yeilding, G., and Gilfillan, G. (2020). Fault Seal modelling – the influence of fluid properties on fault sealing capacity in hydrocarbon and CO2 systems. *Petroleum Goescience*, 481-497.

Kasmarek, M., and Robinson, J. (2004). Hydrogeology and simulation of groundwater flow and land-surface subsidence in the northern part of the Gulf Coast aquifer system, Texas: U.S. Geological Survey. *Scientific Investigations Report*.

Loucks, R. F., Bebout, D., and Galloway, W. E. (1977). Relationship of porosity formation and preservation to sandstone consolidation history- Gulf Coast Lower Tertiary Frio Formation. Gulf Coast Association of Geological Societies Transactions.

McGuire, K. A. (2009). CO2 injection and reservoir characterization: an integrated petrographic and geochemical study of the Frio formation, Texas. Ball State University.

Meckel, T. P., and Trevino, R. (2014). *Gulf Of Mexico Miocene Co2 Site Characterization Mega Transect, Final Scientific/technical Report (Revised).* U.S. Department of Energy National Energy Technology Laboratory.

Meckel, T., and Trevino, R. (2014). Gulf of Mexico Miocene CO2 Site Characterization Mega Transect. Bureau of Economic Geology.

Molina, O., Vilarrasa, V., and Zeidouni, M. (2016). Geologic carbon storage for shale gas recovery. *Elsevier*.

National Risk Index FEMA, Jefferson County, Texas. (2023, 04). https://hazards.fema.gov/nri/learn-more.

Olariu, M. I., DeAngelo, M., Dunlap, D., and Treviño, R. H. (2019). High frequency (4th order) sequence stratigraphy of Early Miocene deltaic shorelines, offshore Texas and Louisiana. *B*ureau of Economic Geology.

Palandri, J. L., and Kharaka, Y. K. (2004). A Compilation of Rate Parameters OF Water-mineralL Interaction Kinectics for Application to Geochemical Modeling. USGS.

Peel, F. J., Travis, C., and Hossack, J. (1995). Genetic structural provinces and salt tectonics of the Cenozoic offshore U.S. Gulf of Mexico: a preliminary analysis. AAPG, 153-175.

Petersen, M., Shumway, A., Powers, P. et al. (2019). The 2018 update of the US National Seismic Hazard Model: Overview of model and implications. *Earthquake Spectra* 36, 6-36. doi:10.1177/8755293019878199.

Roberts-Ashby, T. L., Brennan, S. T., Buursink, M. L. et al. (2012). Geologic framework for the national assessment of carbon dioxide storage resources: U.S. Gulf Coast. USGS.

Savvaidis, A. (2022). *2022 Biennial Report on Seismic Monitoring and Research in Texas.* Austin: Bureau of Economic Geology.

Snedden, J. W., and Galloway, W. E. (2019). The Gulf of Mexico Sedimentary Basin. Cambridge University Press.

Texas Department of Water Resources (1981). *Sabine-Neches Estuary: A Study of the Influence of Freshwater Inflows*.

Treviño, R. H., and Rhatigan, J.-L. T. (2017). Regional Geology of the Gulf of Mexico and the Miocene Section of the Texas Near-Offshore Waters. Bureau of Economic Geology.

U.S. Geological Survey and Texas Bureau of Economic Geology (2023, 10). Quaternary fault and fold database for the United States. https://www.usgs.gov/natural-hazards/earthquake-hazards/faults.

U.S. Quaternary Faults (2023, 04). USGS. https://usgs.maps.arcgis.com/apps/webappviewer/index.html?id=5a6038b3a1684561a9b0aadf88412fcf.

Weaver, C. E. (1977). Fine-Grained Sheet Silicate Rocks. USDOE.

Weber, K., and van Geuns, L. (1990). Framework for Constructing Clastic Reservoir Simulation Models. SPE.

Yassir, N., and Zerwer, A. (1997). Stress Regimes in the Gulf Coast, Offshore Louisiana: Data from Well-Bore Breakout Analysis. AAPG, 293-307.

Yeilding , G. (2002). Shale gouge ratio— Calibration by geohistory, in A. G. Koestler and R. Hunsdale, Hydrocarbon seal quantification. *Norwegian Petroleum Society Special Publication*, 1-15.

Yielding, G., Freeman, B., & Needham, D. T. (1997). Fault seal quantitative prediction: shale smear factor, shale gouge ratio, and smear gouge ratio. *AAPG*.